# Swept-Source Optical Coherence Tomography for Ageing Assessment of High Voltage Cellulose Insulation

by

Biniyam Kahsay Mezgebo

A thesis submitted to the Faculty of Graduate Studies of

The University of Manitoba
in partial fulfillment of the requirements of the degree of

Doctor of Philosophy

Department of Electrical and Computer Engineering
University of Manitoba
Winnipeg, MB, Canada

# Abstract

Oil- impregnated cellulose materials (such as Kraft paper) form an essential part of a transformer insulation system. The mechanical strength of the Kraft paper directly impacts the safe operation of the power transformer. Obtaining both spatially localized absorption profiles and subsurface structural images of the transformer paper would offer considerably more information about the samples than those obtained from optical methods such as microscopy. This could allow a continuous estimation of the operational age of the transformer insulation, beyond only classifying it as belonging to a broad age group.

In this thesis, optical coherence tomography (OCT), a novel and non-invasive diagnostic technique, is used for the first time to acquire subsurface images of the thermally aged Kraft paper samples. To achieve this goal, we implemented a swept-source quadrature OCT (SS-QOCT) system for both structural and spectroscopic OCT image acquisition. Then frame theory was used to develop a generalized OCT image reconstruction method using redundant and non-uniformly spaced frequency domain samples. We also introduced a new concept of applying compressed sensing techniques to acquire a sample's spectroscopic properties, (i.e., its spatially localized light absorption profile). As the typical number of samples acquired by OCT was not sufficient for this purpose, we developed a gradient-based multidimensional signal recovery from incomplete samples in arbitrary separable dictionaries to reduce the number of required measurements for successful spectroscopic signal recovery.

Then accelerated thermal ageing was used to generate samples of oil-impregnated Kraft paper with different levels of deterioration. From these aged paper samples, subsurface structural images at different depths were obtained using swept-source optical coherence tomography (SS-OCT). Statistical texture analysis was applied to these OCT images to convert each image into a spatial

grayscale level dependence matrix (SGLDM), from which Haralick texture features were calculated. Principal component analysis (PCA) is applied to the feature sets to reduce their dimension. The first component of our PCA retains about 98.2% of the total feature set information, and we used it to construct the age estimation model. Finally, leave-one-out-cross-validation (LOOCV) method was used to assess the estimation performance of the fitted model, where we achieved an estimation error of 1.12%. This work demonstrates that the development of OCT-equipped scanning probes to assess the condition of Kraft paper insulation is promising.

# Acknowledgments

Firstly, I would like to express my sincere gratitude and appreciation to my advisor, Dr. Sherif Sherif, for his generous support, immense knowledge, and encouragement throughout my studies. Besides my advisor, I would like to express my appreciation to my co-advisor, Dr. Behzad Kordi, for his outstanding support and supervision during this research. I sincerely appreciate all his valuable comments and guidance.

My sincere thanks also go to my thesis committee, Dr. Arkady Major and Dr. Chase Figley, for taking the time to read my thesis and their valuable comments. My gratitude extends to Manitoba Hydro and Mitacs for the funding opportunity to undertake my Ph.D. study. I also would like to thank Dr. Nathan Jacob at Manitoba Hydro for providing me with samples of the Kraft paper I used in my thesis. I also thank Marwan Elhelaly for the sleepless nights we spent working together to prepare the artificially aged Kraft paper samples. Next, I would like to thank my lab fellows and friends for their academic and personal help. In particular, I am grateful to Dr. Kibreab Assefa and his family for their encouragement and support throughout my studies.

Last but not least, many sincere thanks to my father, Kahsay Mezgebo, and my mother, Letslassie Aregawi, for their kindness, patience, and continued support while I was pursuing my studies. Infinite thanks for their encouragement and for always being there for me. I would also like to thank my sisters for their endless love and support, without whom this would not have been successful. Finally, I would like to dedicate my dissertation work to my parents and family.

# Table of Contents

# List of Figures

# List of Tables

# Chapter 1

# Introduction

## 1.1 Motivation

Power transformers, shown in Figure 1.1., are critical components of a high voltage transmission system with a potential life expectancy of a few decades when operated under normal loading conditions and system voltage [1, 2]. However, the actual in-service life of power transformers can be considerably shorter [3]. Power transformer failures can be very costly to utilities. Replacement of failed units is a long process and could be very costly. A typical transformer's insulation system is comprised of mineral oil and oil-impregnated paper. The most common type of paper used for power transformer insulation systems is called Kraft paper. Kraft paper is a wood-based material mainly composed of cellulose. The Kraft paper is wrapped on or around energized components of the transformer while the whole structure is immersed in a tank of mineral oil. The Kraft paper loses its electrical and mechanical strength when it is subjected to thermal stress. Once the insulation paper breaks down, it could lead to electrical faults.

Figure. 1.1. A power transformer [4].

Chemical and physical changes have been identified in ageing paper insulation. Conventional methods for evaluating the transformer paper insulation can be limited in scope. A widely used method involves analyzing oil samples taken from the transformer and inferring the level of paper deterioration based on chemical markers in the oil [5-8]. However, because this method is indirect, it is insensitive to acute defects in the paper. An established method to estimate paper degradation is the so-called degree of polymerization (DP) test [9]. The DP test has been shown to correlate well with the mechanical tensile strength of cellulose paper [10, 11]. However, the DP test is considered invasive as it requires removing a physical sample of the paper for analysis, which can be damaging to the insulation system. Moreover, the chemical-based assessment methods are usually time-consuming and expensive.

On the other hand, various optical-based diagnostic methods for evaluating power transformer cellulose insulation were proposed. Unlike the established methods, optical measurements have the potential benefits of being able to detect acute defects while being non-invasive to transformer

cellulose insulation [30, 31]. Current optical methods use scanning electronic microscopy (SEM), microscopy surface imaging, speckle imaging, or bulk spectroscopy techniques to assess the degradation of transformer paper. Neither microscopy imaging nor speckle imaging yields information about the internal structural changes in transformer paper that occur due to ageing. Bulk spectroscopy techniques typically result in only spatially averaged infrared absorption values of samples. Therefore, obtaining sub-surface structural images of transformer paper would offer considerably more information about the samples than obtained from current optical methods. This extra information should allow a more accurate estimation of the remaining life, instead of just coarse classification into only a few broad age groups.

The purpose of this research work is to develop non-invasive optical methods for the study of morphological changes in power transformer cellulose insulation caused by thermal stress factors and to evaluate the capabilities of optical methods in the detection and quantification of such changes. The intended long-term motivation is to develop reliable methods for *in-situ* assessment of power transformer cellulose insulation. The development of optical methods for this application provides potential benefits for detecting acute defects in the insulation system while being non-invasive. In addition, optical measurements may be performed off-line during transformer maintenance while the oil is removed for inspection and potentially online with fiber optics and optical sensors, which are electrically inert.

## 1.2  Research Objectives and Outline

The first objective of this research is to implement a hardware setup for swept-source quadrature optical coherence tomography (SS-QOCT) system and acquire both structural and spectroscopic OCT images of the thermally aged transformer cellulose insulation. The second objective of this research is to develop an image reconstruction algorithm for the OCT system. The final objective

3

in this research is to apply the statistical texture analysis methods to the thermally deteriorated paper samples to construct a continuum remaining age estimation model by examining how the texture features change as a function of ageing time. This research aims to develop a machine-learning algorithm to estimate the remaining lifetime of high voltage transformer insulation paper.

## 1.3 Outcomes and Contribution

In this research, a swept-source quadrature OCT (SS-QOCT) hardware setup was implemented. The SS-QOCT acquires both real and imaginary parts of interferometric OCT signal to produce a subsurface localized structural image. The spectroscopic analysis can be applied to the OCT data to acquire subsurface structural images and localized near-infrared absorption profiles. In this thesis, accelerated thermal ageing experiments were carried out for Kraft paper to create a set of paper samples belonging to deterioration levels with minimum and maximum ageing times of 0 hours and 396 hours, respectively. Furthermore, statistical texture analysis methods have been applied to the degraded oil-impregnated Kraft paper samples to analyze the OCT subsurface morphological changes in the paper caused by thermal stress.

The first significant contribution obtained in this research has been implementing a quadrature OCT system and developing a novel generalized OCT image reconstruction algorithm using the Frame Theory to reconstruct the subsurface image of an object from non-uniformly spaced samples.

The second key contribution of this research is developing a novel compressed sensing-based spectroscopic OCT algorithm. The spectroscopic OCT algorithm extracts spatially localized absorption and scattering profiles from the sample. To the author's best knowledge, none of the current spectroscopic algorithms apply to a swept-source OCT, which is the fastest OCT imaging method available. A gradient-based multidimensional signal recovery algorithm has been developed to reduce the number of measurements required to recover the spectroscopic information accurately.

The third key contribution of this research is constructing a continuum remaining age estimation model that exhibits the ageing condition of the Kraft paper sample. The result has shown that certain statistical texture features exhibit a logarithmic relationship with the ageing time. This implies that the paper's mechanical strength is directly related to the subsurface morphological changes that occur to paper fibers and their network structure in response to thermal stress. Principal component analysis (PCA), the feature dimension reduction technique, was applied to the feature set, and the PCA output is then used to construct the age estimation model. The estimation performance of the fitted model was assessed using leave-one-out-cross-validation (LOOCV), with an estimation error of 1.12%.

## 1.3.1  Publications

A list of publications directly resulting from this research are listed below in chronological order:

**Conference papers**

- B. K. Mezgebo, K. Nagib, N. Fernando, B. Kordi, and S. Sherif, "Scaled nonuniform Fourier transform for image reconstruction in swept-source optical coherence tomography," in *Optical Coherence Tomography and Coherence Domain Optical Methods in Biomedicine XXII*, J. A. Izatt, J. G. Fujimoto, and V. V. Tuchin, Eds.   SPIE, Feb 2018.

- B. Mezgebo, K. Nagib, N. Fernando, B. Kordi, and S. Sherif, "Swept-source optical coherence tomography of objects with arbitrary reflectivity profiles," in *2nd Canterbury Conference on OCT with Emphasis on Broadband Optical Sources,* O. Bang and A. Podoleanu, Eds.  SPIE, Mar 2018.

- K. Nagib, B. Mezgebo, B. Kordi, N. Fernando, R. Thakur, and S. S. Sherif, "Increasing

signal-to-noise ratio of swept-source optical coherence tomography by oversampling in k-space," in *2nd Canterbury Conference on OCT with Emphasis on Broadband Optical Sources,* O. Bang and A. Podoleanu, Eds. SPIE, Mar 2018.

- B. Mezgebo, B. Kordi, N. Fernando, and S. S. Sherif, "Estimation of power transformer insulation ageing using optical coherence tomography," *in 2020 IEEE Conference on Electrical Insulation and Dielectric Phenomena (CEIDP).* IEEE, Oct 2020.

**Journal papers**

- Nagib Karim, Biniyam Mezgebo, Namal Fernando, Behzad Kordi, and Sherif S. Sherif 2021. "Generalized Image Reconstruction in Optical Coherence Tomography Using Redundant and Non-Uniformly-Spaced Samples" *Sensors* 21, no. 21: 7057.

- B. Mezgebo, S. S. Sherif, N. Fernando and B. Kordi, "Paper Insulation Aging Estimation Using Swept-Source Optical Coherence Tomography," in *IEEE Transactions on Dielectrics and Electrical Insulation*, vol. 29, no. 1, pp. 30-37, Feb. 2022.

- Biniyam Mezgebo, Ishan Wickramasingha, Behzad Kordi, Sherif S. Sherif, "Gradient-Based Multidimensional Signal Recovery from Incomplete Samples in Arbitrary Separable Dictionaries" to be submitted to IEEE Transactions on Image Processing (2022).

# 1.4 Thesis outline

This thesis is organized into eight chapters with content as described below:

**Chapter 1**: Motivation, research objectives, primary contributions, and outcomes of the research are presented.

**Chapter 2:** Presents background technical information applicable to this research work. A general overview of the power transformer insulation system is discussed, along with deterioration mechanisms. A description of oil-impregnated cellulose material, the most common electrical insulation system, is provided along with its deterioration mechanisms and power transformer failure modes. Chemometric and optical-based existing methodologies used to assess insulation deterioration as a consequence of thermal stress are reviewed. An introduction to one of the advanced imaging modalities called optical coherence tomography (OCT), and statistical texture analysis is also presented in this chapter.

**Chapter 3:** Presents results from an implementation of swept-source quadrature OCT (SS-QOCT) system where both the real and imaginary components of the OCT interferogram signal are obtained.

**Chapter 4:** Presents a novel-generalized image reconstruction algorithm for OCT using redundant and non-uniformly spaced samples. Swept-source OCT (SS-OCT) and Frame Theory are reviewed. Then, our generalized method for signal reconstruction from redundant and non-uniformly spaced samples is discussed, along with its application to OCT A-scan reconstruction. An efficient way to compute our corrected reconstruction transform, i.e., a *scaled* non-uniform discrete Fourier transform (NDFT), using the Fast Fourier Transform is presented. The last section of this chapter demonstrates the different advantages of our generalized OCT image reconstruction method.

**Chapter 5:** The concept of compressed sensing and spectroscopy OCT are reviewed. Our mathematical formulation of the compressed sensing-based spectroscopy OCT is presented along

with a discussion on extracting spatially localized absorption and scattering profiles from a full complex interferometric signal acquired by swept-source quadrature OCT. The minimum number of measurements required for accurately recovering the spectroscopy signal using our compressed sensing-based method is also discussed.

**Chapter 6:** Presents an algorithm that recovers N-dimensional gradient sparse signal from incomplete measurements using Kronecker products of arbitrary transformation domains. Weighted tensor least angle regression (WT-LARS), an efficient multilinear compressed sensing method, is used to recover multidimensional gradients from incomplete measurements. *N*-dimensional Poisson problem is solved using a gradient-based iterative method to reconstruct the actual *N*-dimensional signal from the gradients. A numerical example that demonstrates the performance of the multidimensional gradient-based signal recovery method is presented.

**Chapter 7:** Presents the experimental setup for preparing thermally aged oil-impregnated paper samples and the OCT measurement arrangement. The subsurface morphological changes in the OCT images of thermally deteriorated paper samples are discussed. A statistical texture analysis-based method called the Spatial Grey Level Dependence Matrix (SGLDM) is presented. Texture features representing the ageing condition of the thermally deteriorated Kraft paper samples are extracted from the SGLDM. Principal component analysis (PCA), a feature dimension reduction technique, is applied to the feature set. The PCA output is then used to construct a remaining age estimation model, and the parameters of the model are obtained by solving a non-linear data fitting problem. A validation technique called the leave-one-out-cross-validation (LOOCV) method is used to assess the estimation performance of the fitted model.

**Chapter 8:** Conclusions of this thesis project and potential future research work that would improve and expand on this thesis work are discussed.

# Chapter 2

# Background and Literature Review-Power Transformer Insulation System, Ageing Assessment Methods, Optical Coherence Tomography and Image Texture Analysis

In this chapter, a brief overview of high voltage transformer paper insulation is presented, along with a description of the thermal deterioration of the Kraft paper and failure mechanisms. Morphological changes to the oil-impregnated paper occurring due to deterioration from thermal stress are described, along with a description of changes to the paper's mechanical properties. A

review of existing methods for evaluating the degradation of the transformer paper insulation, including optical-based methods, is covered, along with a discussion regarding their advantages and shortcomings. Finally, a new diagnostic method called optical coherence tomography is introduced, and the concept of statistical texture analysis will be discussed briefly.

## 2.1    High Voltage Transformer Insulation System

Power transformers are critical components of a high voltage transmission system with a potential life expectancy of around 40-years when operated under normal loading conditions and system voltage [1]. However, the actual in-service life of power transformers can be considerably shorter [3]. The lifetime of the power transformer insulation system determines the lifetime of the power transformer. Stress factors such as thermal, mechanical, and electrical deteriorate the insulating material, reducing the power transformer's typical life expectancy.

Oil-impregnated cellulose materials (such as Kraft paper) form an essential part of a transformer insulation system. Kraft paper is an unbleached paper, and its molecular composition constitutes a naturally occurring straight-chain polymer called cellulose [14].  Chemically, Kraft paper comprises approximately 95% cellulose, $4 - 5\%$ hemicellulose, and 1% lignin.

The average number of cellulose elements in new paper insulation would be approximately 1000-1200. The monomer element in the cellulose molecule is essentially a glucose molecule where each glucose molecule loses one hydrogen and one hydroxyl element to form cellulose. Chains of cellulose molecules are composed of amorphous and crystalline regions that include micro-fibrils, which make up larger macro-fibrils that comprise the cell walls of individual paper fibers.

Figure 2.1. A power transformer insulation Kraft paper [4]

The microfibrils' mechanical strength is directly related to the length of the cellulose molecules and crystallinity in their molecular arrangement, where intra- molecular bonds are formed between the cellulose molecule chains [5,6]. The cellulose loses its mechanical strength due to ageing, which is indicated by its chemical and physical changes. A decrease in mechanical strength is attributed to reducing the number of glucose units in the molecular chain [10,11]. The arrangement of cellulose molecules in the amorphous region is disordered and loose and is more easily deteriorated in the ageing process. Whereas in the crystalline region, fibers are arranged orderly and stable. The winding (or coils), copper, or aluminum windings make the main structure of nearly all power transformers wrapped with Kraft paper and immersed in mineral oil, as shown in Figure 2.1. Mineral oil is usually a highly refined mineral oil having good cooling and electrical insulating properties [6,7]. The mineral oil also enhances the dielectric properties of the insulating paper by filling the air voids in cellulose fibers of the Kraft paper.

11
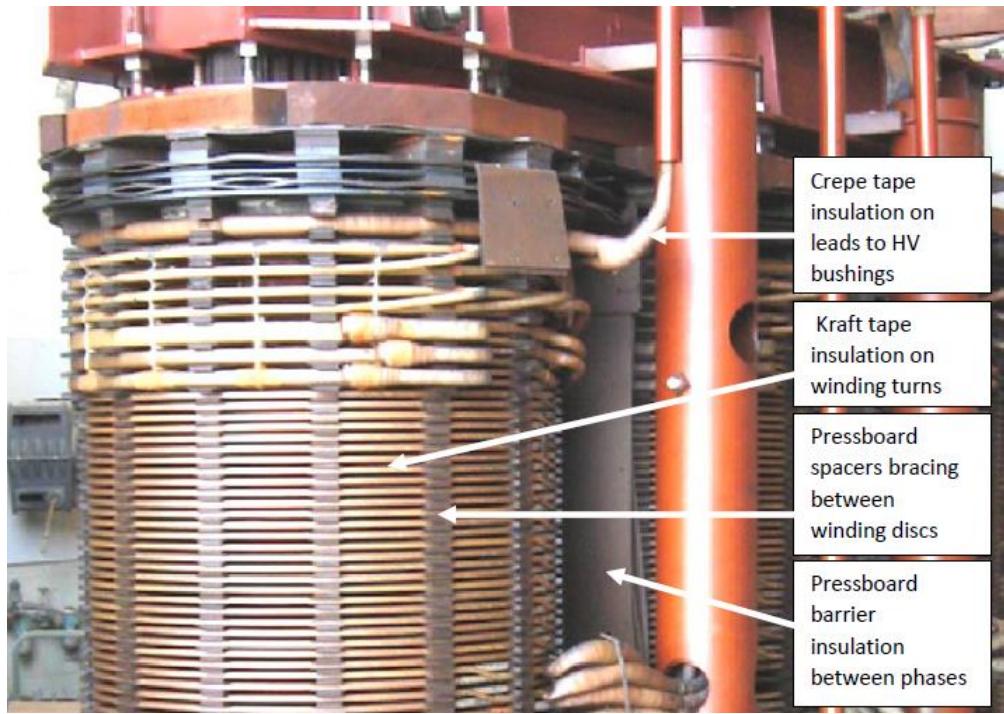
Figure 2.2. Transformer core and coils removed from tank. Kraft tape winding insulation, crepe tape HV bushing lead insulation, pressboard spacers between discs, and pressboard barriers between phases are identified [4].

On the other hand, as the solid insulation material, the Kraft paper supports mechanically and electrically separate live parts, such as the transformer winding turns and discs. Thus, the mechanical strength of the Kraft paper directly impacts the safe operation of the power transformer. The paper also resists the propagation of partial discharges. In the absence of paper, suspended particles in the oil can attach themselves to metallic conductors causing partial discharge issues. Different forms of Kraft paper are used for various electrical insulating purposes inside the power transformer. Examples of these other forms of Kraft cellulose papers are shown in Figure 2.2.

## 2.2 Paper Insulation Ageing Mechanisms and Failure Modes

The physical structure of the Kraft paper contains many micro-scale cracks in different regions of the fibers. When the transformer operates at full load, the insulation paper deteriorates continuously due to electrical, thermal, and mechanical stresses. This results in a reduced typical life expectancy of the power transformer. The most common deterioration mechanism of the paper insulation component in power transformers is caused by thermal stress [10, 11]. Over time, the heat produced by the transformer core and windings during regular operation thermally degrades cellulose materials. This led to stiffness and brittleness of the fibers of the cellulose materials as the micro-scale cracks in the fiber develop further with the ageing time. These cracks eventually reduce the mechanical strength of the paper, determined by the tensile strength index. Once the insulation Kraft paper breaks down, its dielectric and mechanical properties cannot be renewed.

Many transformer failures occur when the deteriorated paper insulation is subjected to a system disturbance, such as a through-fault or load rejection [3]. Such electrical system events cause abrupt electromechanical forces on the windings, disturbing the brittle winding insulation between turns. The likelihood of the paper tearing is increased when the tensile strength has been compromised due to thermal ageing. Tearing the insulation paper can lead to an electrical fault. Another deterioration mechanism that can degrade the paper component is caused by internal electrical stress leading to partial discharge.

Partial discharge (PD) in electrical insulation is a phenomenon where applying high voltage across an insulation system causes a localized breakdown or arcing across small voids inside that system or tracking across insulation surfaces. Over time, sustained PD activity will degrade the insulation level of the system and can cause eventual failure [15, 16]. Within a power transformer, PD can occur at various locations of the insulation system. Discharges can occur as Corona from high voltage windings and terminals into the oil volume discharge between energized components such as between the primary and secondary windings discharges between phases, or discharges between winding turns. A complex deterioration mechanism that can lead to power transformer

failures involves forming PD along pressboard barrier surfaces, sometimes referred to as creepage discharge [17]. Such discharge may originate due to undissolved gas or high moisture content in the pressboard resulting in PD. Discharge may also occur due to a phenomenon called static electrification, where surface friction between the pressboard and oil circulating in the power transformer causes a build-up of static charge on pressboard surfaces. This charge and the internal electric field stresses can result in the formation of PD [17]. Recurrent PD can lead to forming permanent carbon tracks on the pressboard surfaces, thus reducing the electrical insulation level. As a result, the risk of catastrophic failure during electrical transients such as a lightning strike or switching transients is elevated [9]. An example of a transformer failure attributed to creepage discharge on the pressboard is shown in Figure 2.3.



Figure 2.3. Converter transformer failure where evidence of partial discharge activity found on barrier surface between two windings [4].

Once the insulation paper breaks down, it could lead to electrical faults. This can result in

enormous economic loss as the operational life of the insulation directly determines the life expectancy of the power transformer [12,18]. It is believed that between $10 - 30\%$ of power transformers failures occur due to the reduced tensile strength of the oil-impregnated Kraft paper as it thermally ages [12]. Therefore, to ensure higher reliability and safety, it is crucial to assess the condition of insulation paper degradation.

## 2.3    Methods for Ageing Assessment of Transformer Paper Insulation

There are several established methods for evaluating the degradation of the transformer paper insulation. A widely used method involves analyzing oil samples taken from the transformer and inferring the level of paper deterioration based on chemical markers in the oil [19, 20]. However, because this method is indirect, it is insensitive to acute defects in the paper. The so-called degree of polymerization (DP) test is an established method for directly analyzing the paper component to detect degradation [21, 22, 23]. However, the DP test is considered invasive as it requires removing a physical sample of the paper for analysis, damaging the insulation system. Chemical markers in the oil and DP measurements from the degraded oil-impregnated paper samples have been used to model the remaining useful life of the transformer using different methods, e.g., statistical-based methods [24, 25, 26, 27].

### 2.3.1   Dissolved Gas Analysis

The dissolved gas analysis (DGA) involves high precision measurement of gasses uniformly dissolved in the transformer oil by an extraction process called gas chromatography. Gas chromatography is commonly used for the analysis of oil samples. Measurements of the relative concentrations of gases present in the oil can indicate specific insulation problems related to high temperature, partial discharge (PD), and internal arcing. This method for analyzing the transformer

oil to detect insulation problems is called dissolved gas analysis [10]. Degradation of the insulation paper from DGA is detected by comparing the relative concentrations of carbon monoxide to carbon dioxide present in the oil. Generally, if the ratio of carbon monoxide to carbon dioxide is less than 1.0, this may indicate insulation paper heating. Paper insulation degradation is also detectable by the presence of furanic compounds in the oil formed as the paper is deteriorated by thermal ageing [19, 20]. These compounds are dissolved in the oil and measured using high-performance liquid chromatography or gas chromatography-mass spectrometry [10].

The shortcomings of using samples of oil to detect problems in the paper are that they are indirect. The analysis is performed on a sample taken from a large volume of transformer oil which may make the method insensitive to detecting acute defects in the paper. Accumulation of gases in the oil may be caused by distributed defects producing heat and PD in the paper and slowly deteriorating the insulation, or they may be caused by a singular defect, which is quickly deteriorating towards failure.

## 2.3.2   Measurement of Degree of Polymerization

An established method for direct analysis of the paper component to detect degradation directly is called the degree of polymerization (DP) test [28]. The DP test has been shown to correlate well with the mechanical tensile strength of cellulose paper [3, 23, 28, 29], and it has also been shown to be directly proportional to the Furan content in oil. Figure 2.4 shows the experimental results obtained by Emsley *et al*. [12] and Lundgaard *et al*. [13]. The DP test is performed on a sample of paper taken from the transformer, dissolved in a cellulose solvent (Cupriethylenediamine, 1.0M) to form a slurry. The viscosity of the slurry is directly proportional to the average length of the cellulose molecules in the original sample of paper. As the paper is thermally aged, it forms breaks in the cellulose molecules to form shorter chains. This reduces the mechanical strength of the paper

and reduces the DP. In general, for new transformer paper insulation DP is expected between 1000-1200 units. If the paper becomes critically aged and its tensile strength reduced so that it is at high risk for failure, DP is expected to be less than 400 units [3]. However, the DP test is considered too invasive, which requires removing a physical sample of the paper for analysis, which can be damaging to the insulation system. In addition, since the cellulose sample is not easily accessible, the DP test is not always recommended.
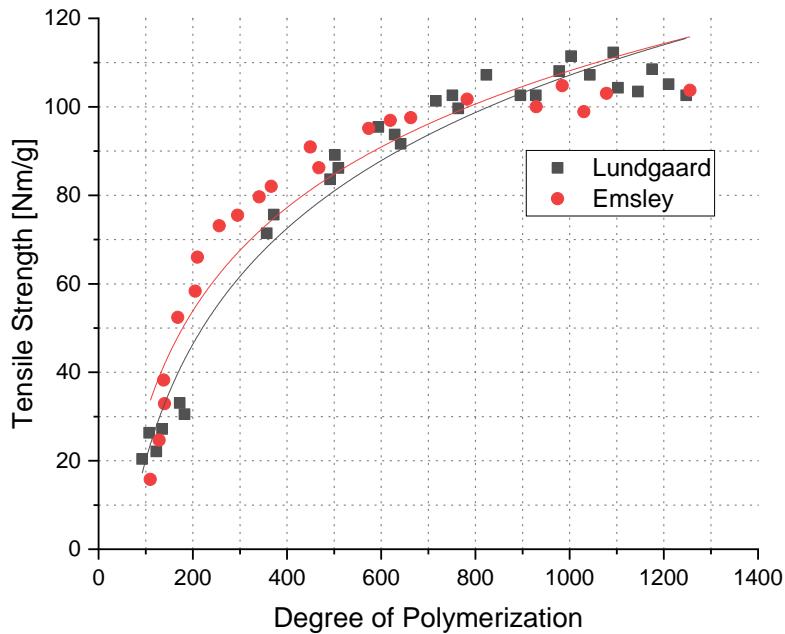
Figure 2.4. Relationship between tensile strength and degree of polymerization from experimental data given in [12] and [13].

## 2.4    Optical Methods to Assess Degradation of Transformer Paper

Unlike the established methods, optical techniques have good electrical isolation, and hence they are suitable for *in-situ* measurements under high voltage. Morphological changes to the paper

occurring due to deterioration from thermal and electrical stress can alter physical and chemical properties and therefore alter the interaction of cellulose insulation materials with light.

Different optical-based imaging modalities were proposed for direct assessment of the condition of power transformers insulation paper, such as microscopy imaging. The microscopy imaging method has been demonstrated as useful for characterizing the thermal degradation of transformer insulation paper [30, 31, 32, 33]. Changes in the surface have been correlated with the degree of polymerization measurements [30]. However, optical microscopy measurements on insulation paper may be hindered by the varying depth profile of the paper structure. Acquiring images where all regions of the sample are in focus can be difficult at high magnifications.

Similarly, the potential application of using the optical speckle phenomenon to discriminate between paper samples with different thermal ageing levels was investigated. However, the optical surface imaging methods do not yield information about internal structural changes in transformer paper that occur due to thermal ageing. That is why these two optical imaging-based methods were only able to classify the age of the transformer paper into four broad ageing levels.

Alternative optical imaging modalities such as scanning electron microscopy (SEM) and confocal laser scanning microscopy (CLSM) could be more suitable for this purpose because they can reconstitute images from information obtained at different depth profiles [34]. For electrical papers used in power transformer insulation, SEM has been used to qualitatively characterize the degradation of paper fibers and structure due to thermal ageing. Degradation has been associated with thinning of the paper fibers, the formation of cracks and holes in the fiber walls, and disruption of the interwoven network structure of the fibers [35, 36, 37]. Although SEM and CLSM can provide paper images with better resolution and contrast, their downfall is that they are invasive and require a physical sample for measurement.

As an alternatives to SEM and CLSM, atomic force microscopy (AFM) was also proposed to assess the condition of Kraft paper [37, 38]. AFM was used to determine the effects of chemical

reactions induced by thermal stressing, with results suggesting the reduction of certain molecular bonds was indicative of deterioration [38]. *In-situ* measurements were performed by Raman spectroscopy on three independent transformer windings in [39]. Raman spectroscopy measures the reflected light from a beam projected onto the specimen surface. However, these *in-situ* measurements yielded inconsistent spectral results due to excessive scattering of the incident light from irregular curvatures of transformer windings.

An alternative to the Raman reflectance spectroscopy method used in [39] is attenuated total reflectance Fourier transform infrared spectroscopy (ATR-FTIR). This technique utilizes a probe that makes direct contact with the specimen surface. A fiber optic cable carries an infrared beam with a specified wavelength of light to a crystal sensor directly in contact with the specimen. ATR-FTIR captures spectroscopic information about the material by an evanescent wave formed at the interface between the crystal sensor and the specimen. This wave will attenuate the signal when a chemical bond vibration is excited by a particular wavelength of light. Attenuated total reflectance has also been used to analyze polymer materials used in transmission line insulators in [40]. However, one of the main drawbacks of the bulk spectroscopy techniques is that they typically result in only spatially averaged infrared absorption values of samples. As a result of these limitations, a new diagnostic method for evaluating power transformer cellulose insulation is required.

## 2.5   Optical Coherence Tomography

Optical coherence tomography (OCT) is a non-invasive biomedical imaging technique capable of acquiring high-resolution three-dimensional subsurface structural images of different medical and industrial samples [41, 42, 43, 44, 45]. An OCT system, a Michelson interferometer-based imaging modality, uses a near-infrared light source to probe a sample and acquire images by measuring the

back-scattered beam from an object in a way similar to ultrasound imaging. However, using a light source allows OCT systems to acquire high-resolution cross-sectional images of samples at a higher speed. In addition, this imaging modality can image samples *in-situ* and with no contact needed between the imaging probe and sample.

OCT fills a valuable niche in imaging subsurface microstructures: providing high spatial resolution (10 microns) imaging in three dimensions and high sensitivities (100 dB) with no contact needed between the imaging probe and sample [41,42, 43, 44]. Some of the advantages of OCT over other alternative optical and non-optical imaging techniques are its high resolution, contact-free, and non-destructive operations.
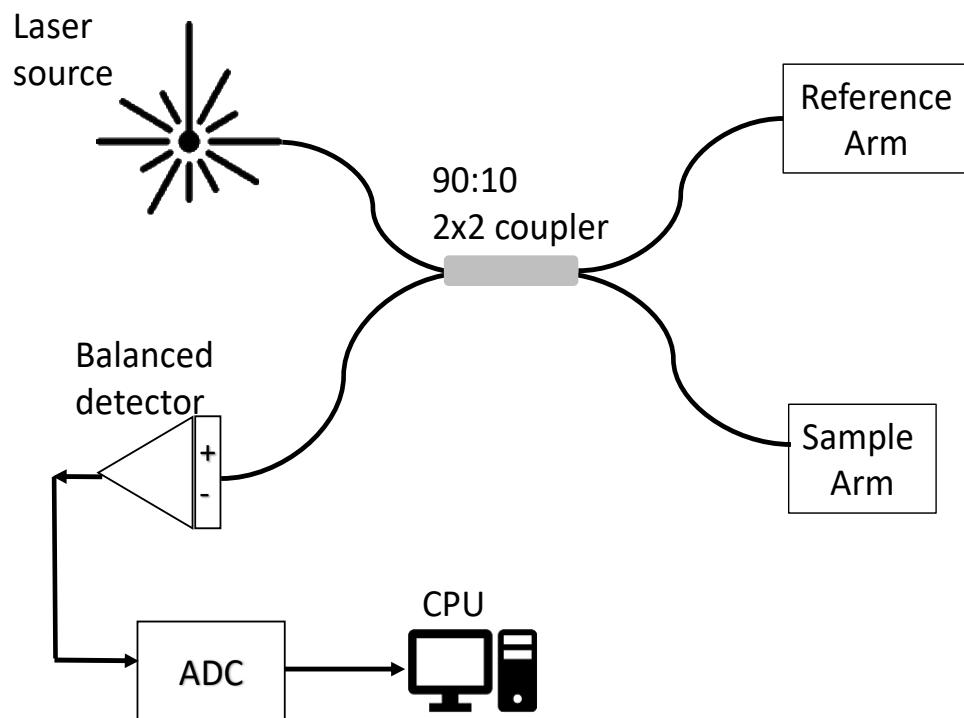
Figure 2.5. System diagram of OCT system

A schematic representation of a typical OCT system arrangement is shown in Figure 2.5. OCT is a Michelson interferometer-based imaging technique that measures the backscattered light from an object. In OCT, the interferometer is illuminated with the light emitted from a low-coherence light source. The power supplied by the swept source is divided by $2 \times 2$ fused-fiber couplers into two arms, known as the reference beam and the sample beam. A 90/10 fiber coupler is used (a regular 50: 50 can be used too), where 90 percent of the light power goes to the sample arm and 10 percent of it goes to the reference arm. The multiple layers of the sample reflect the light illuminating the sample. The light reflected from the reference and sample arms are then redirected into another $2 \times 2$ coupler, and a balanced photodetector detects the interference of the two wavefields. The detected analog interference OCT signal is then converted into a digital signal using a data acquisition board. The OCT fringe data are then sent to the host computer, where the signal processing is performed. The amplitude of the interference current signal is proportional to the local value of the backscattering coefficient at the corresponding probing depth. Moreover, the photodetector samples the recorded signal at equal intervals. Each wavelength scan produces depth information from the interference pattern by reflection at different depths in the form of an A-scan. An A-scan is simply a one-dimensional image of the sample at a specific depth. By acquiring multiple A-scans along a line in the transverse direction, a cross-sectional image of the sample called B-Scan can be obtained. Also, a three-dimensional volumetric image of the sample's microstructure can be obtained by superimposing multiple B-scans.

OCT techniques are generally divided into two main categories: time-domain (TD) OCT and frequency-domain (FD) OCT. Frequency domain OCT includes spectral domain (SD) and swept dource (SS) OCT. Note that the reference mirror in the TD-OCT is a moving part and is stationary in the case of FD-OCT. FD-OCT generally acquires images with fewer artifacts and provides higher imaging speed than the TD-OCT due to the more straightforward mechanical design of the fixed reference arm [42, 46]. Also, compared to the TD-OCT, FD-OCT provides higher detection

sensitivity [42].

## 2.6    Texture Analysis of Images

Texture analysis extracts metrics/features from an image that quantifies its smoothness or coarseness and is used in different applications such as remote sensing and biomedical imaging [47]. In this thesis, the texture is defined as the spatial variation of pixel intensities. Features describe texture properties and contain essential information about the stochastic properties of the spatial distribution of gray-level in an image that represents specific image properties such as coarseness, contrast, and homogeneity [48, 49, 50]. There are four approaches for analyzing texture that can be defined as statistical, structural, model-based, and transform-based methods [48]. The statistical texture analysis method primarily describes the texture of regions in an image by translating an image into a matrix that contains information about the variation of pixel intensities [23] i.e., textures are represented by stochastic properties of gray levels of pixels in an image. Second-order statistical methods, given based on the relation between pairs of pixels, have shown better discrimination ability. The most frequently used second-order statistical technique for texture analysis is extracting various textural features from a spatial gray level dependence matrix (SGLDM). In this work, SGLDM will be applied to OCT images of thermally deteriorated Kraft paper samples in chapter 7.

The structural texture analysis method associates texture features with well-defined structural elements such as regularly spaced parallel lines, and it allows a good symbolic description of the image. However, the structural-based technique appears limited in practicality since it is applied to images with very regular textures. Thus, these methods were not used for OCT images of thermally deteriorated paper, as the paper subsurface structural texture is very random. Hence, the structural texture method is not appropriate for this type of image.

Model-based methods for texture analysis are used to characterize texture which determines

an analytical model of the textured image being analyzed. Model-based texture analysis generates an empirical model for each pixel in an image by analyzing content in the surrounding pixels. In this method, a model, such as Autoregressive, Markov Random Fields (MRFs), and Hidden Markov, which can describe the image texture, is created. Its estimated parameters determine the properties of the texture that may be synthesized by applying the model. MRF has been widely studied as a model for texture.

Transform-based methods convert images into a new form using transformation techniques such as Fourier, wavelet, Curvelet, and Gabor while extracting textural information from the transformed images [51, 52]. However, the Fourier transform has practical limitations due to the lack of spatial localization. In contrast, the wavelet transform can represent texture suitably due to variable spatial resolution and freedom in choosing wavelet function from a wide range for a specific application. In instances texture analysis is used for discerning between materials having different surface textures, features extracted from the texture analysis method are commonly processed using machine learning algorithms to enable automated classification of a material category, quality, or condition [23].

## 2.7    Chapter Summary

Oil-impregnated cellulose materials (such as Kraft paper) form an essential part of a transformer insulation system. Kraft paper, composed of 95% cellulose, is constituted mainly by cellulose fibers and wrapped around an energized conductor. Therefore, the mechanical strength of the Kraft paper directly impacts the safe operation of a power transformer.

When the transformer operates at full load, the oil-impregnated insulation paper continuously deteriorates due to the heat produced by the transformer core and windings. As this thermal degradation becomes significant, the insulation paper's mechanical tensile strength reduces and becomes more brittle. Once the insulation paper breaks down, it could lead to electrical faults.

Many power transformer failures occur due to the reduced tensile strength of the insulation paper, which is attributed to a chemical change occurring in the paper as it thermally ages. When the Kraft paper ages, the average length of the cellulose molecules within the paper decreases. This leads to a loss of the tensile strength of the insulation paper. Chemical reactions in the paper are activated by heat, causing a breakdown in the cellulose molecules. Optical imaging methods such as optical coherence tomography (OCT) can detect the changes that occur to the subsurface morphology of the paper as a consequence of thermal deterioration. As the paper deteriorates, its cellulose fibers become distorted as cracks and holes form on the paper wall.

Several established chemometric parameters have shown beneficial in assessing deterioration of oil-impregnated Kraft paper insulation in power transformers. However, current methods for assessment of the paper insulation in power transformers have several limitations. First, approaches which involve indirect techniques associated with measurements on the oil component of the insulation system are ineffective at detecting deterioration of acute or regional insulation defects. Lastly, methods such as the DP or tensile strength tests are considered direct test methods performed on a sample paper taken from the transformer insulation. However, the main limitation of the existing direct methods is that they require too large a paper sample taken from the transformer, making the assessment too invasive and impractical. Therefore, a brief overview of the OCT system has been presented, along with a description of statistical texture analysis.

# Chapter 3

# Implementation of Swept Source Quadrature Optical Coherence Tomography

In this chapter, an overview of quadrature swept-source OCT is described. First, a complete schematic of the quadrature swept-source OCT system set up and its working principle is discussed.

## 3.1 Swept Source Quadrature OCT System

Swept-source OCT measures the real part of the complex interferometric signal between a reflected reference wave and a backscattered wave from the tissue sample. A cross-sectional image of the sample is reconstructed by subjecting the real-valued interferogram signal to Fourier transform. In the $2 \times 2$ swept-source OCT, only the real component of the interferometric signal is recorded, and the imaginary part (quadrature) is ignored. Consequently, the Fourier inversion on the real interferometric component only produces a complex conjugate artifact.
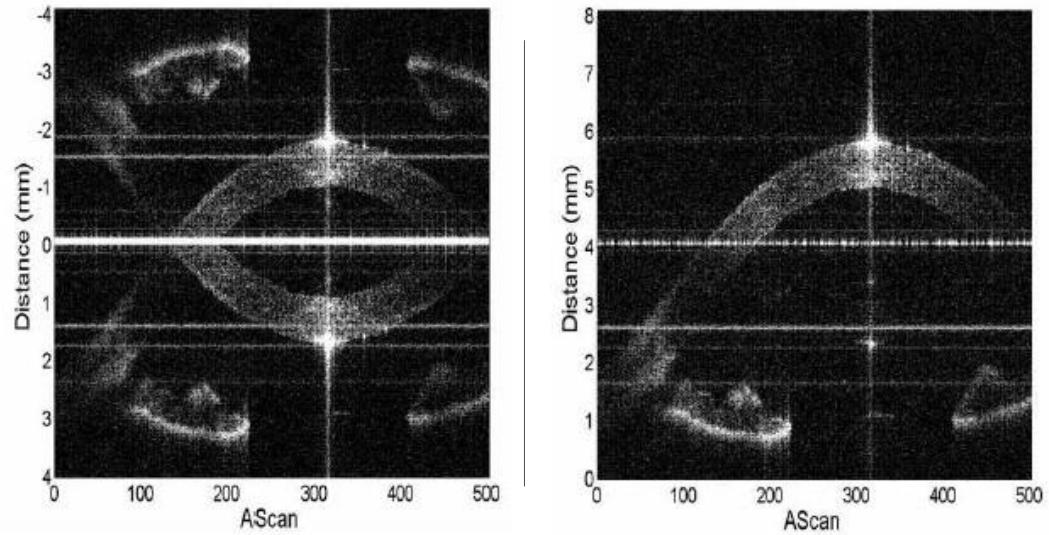
Figure 3.1. Cross-sectional image of an interior segment of the human eye acquired using a 3×3 spectral domain-OCT (SD-OCT) system. (a) The real component of the complex interferogram was used to generate the image (b) The full quadrature signal was used to image the sample, resulting in an image free of the mirror image and clear visualization of the sample [53].

This image artifact is produced by the potential overlapping between the actual image and its mirror image. The artifact prevents the distinction between positive and negative object depths, thereby reducing the effective imaging range. As imaging range is essential in various applications, removing this complex conjugate artifact achieving full range in SS-OCT is of significant interest. The complex part of the signal must also be acquired to resolve this artifact. Figure 3.1 shows B-scans of the anterior segment of a human eye in vivo acquired using quadrature SD-OCT. The image of the sample reconstructed using only the real component, acquired using only a single detector, of the complex interferogram is shown in Figure 3.1 (a). It is seen that the image suffers from complex conjugate artifacts due to the overlapping of the actual image and the mirror image. The OCT image in Figure 3.1 (b) used the interferometric signal from the two detectors, and it was shown that suppression of the mirror image doubles the effective imaging depth.
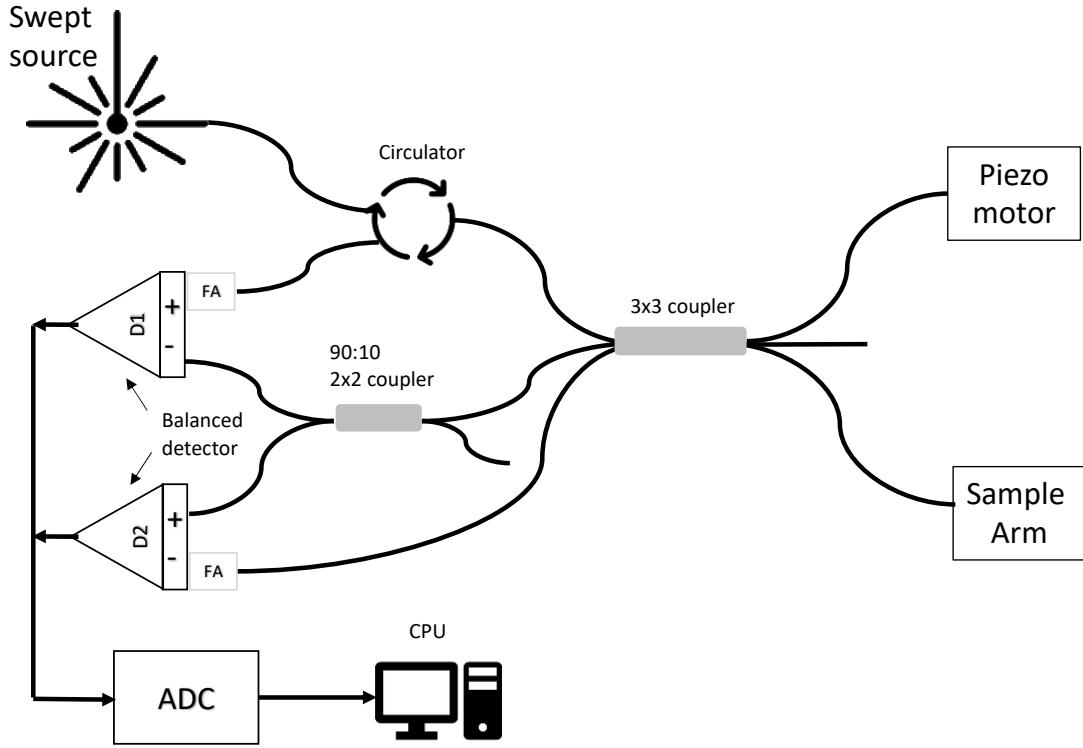
Figure 3.2. Schematic diagram of 3 × 3 quadrature OCT using a swept-wavelength laser. An optical circulator recovers the signal light in the source arm. D1 and D2 are photodiode detectors. FA is fiber attenuator.

Different full-range SS-OCT imaging methods that measure the complex component of the interferometric signal by shifting the phase of the reference and sample reflections have been reported [54, 55, 56]. However, these methods suffer from significant image corruption resulting from slight variations in used materials' phase shift or birefringence. Recently, the acquisition of both real and imaginary interferometric components was demonstrated using Michelson quadrature interferometers using $3 \times 3$ fused fiber couplers and nondifferential optical detection [53, 57].

In [53], a 3×3 Michelson quadrature interferometer with balanced differential detection was used for acquiring the complex interferometric signal. A Michelson interferometer-based swept-source quadrature OCT system using a $3 \times 3$ coupler and two optical detectors is illustrated in Figure

3.2. The incoming light source travels to the $3 \times 3$ fiber coupler with coupling ratios of $0.33\colon 0.33\colon 0.33$. At the output of the coupler, 1/3 of the source power travels to the sample arm and reference arm (piezo motor). The back-reflected signals are collected by the $3 \times 3$ and redirected to the $2 \times 2$ coupler, where each of the two outputs go into the two balance detectors D1 and D2, as shown in Figure 3.2. The fiber circulator was used in the source arm to redirect the back-reflected light to the balanced detector D1. Finally, the output signals on detectors D1 and D2 are recorded simultaneously using a data acquisition (DAQ) card. In [58], it was demonstrated that a $90^{\circ}$phase difference between the detector outputs D1 and D2 could be obtained if the input power ratio was 2.6. The fiber attenuators (FA) are used to control the amount of power input to the detectors.

## 3.1.1 Analysis of Scalar Scattering of Light from Inhomogeneous Media

The scattering in this analysis is associated with the interaction of waves or particles with material media. We will restrict ourselves to circumstances where the response of the medium to the incident wave is linear and can be described by parameters such as dielectric constant or, equivalently, by the refractive index or the dielectric susceptibility. The scalar scattering equation is given by [59]

$$\nabla^2 U(\boldsymbol{r}, k) + k^2 n^2 (\boldsymbol{r}, k) U(\boldsymbol{r}, k) = 0 \tag{3.1}$$

where $n(\boldsymbol{r}, k) = n_s(\boldsymbol{r}, k) + j n_a(\boldsymbol{r}, k)$ denotes the refractive index of the medium. The real part of the refractive index, $n_s(\boldsymbol{r}, k),$ corresponds to the scattering property whereas the imaginary part, $n_a(\boldsymbol{r}, k),$ corresponds to the absorption profile. The total field $U(\boldsymbol{r}, k)$ can be expressed as the sum of the incident field, $U^{(i)}(\boldsymbol{r}, k)$ and of the scattered field $U^{(s)}(\boldsymbol{r}, k)$ as $U(\boldsymbol{r}, k) = U^{(i)}(\boldsymbol{r}, k) + U^{(s)}(\boldsymbol{r}, k)$. The refractive index $n(\boldsymbol{r}, k)$ is related to the scattering potential of the medium by

$$P(\mathbf{r}, k) = -k^2[n^2(\mathbf{r}, k) - 1] \tag{3.2}$$

Substituting (3.2) into (3.1), the following equation can be obtained

$$\nabla^2 U(\mathbf{r}, k) + k^2 U(\mathbf{r}, k) = P(\mathbf{r}, k)U(\mathbf{r}, k), \tag{3.3}$$

The incident field $U^{(i)}(\mathbf{r}, k)$ is usually a plane wave and satisfies the Helmholtz equation

$$(\nabla^2 + k^2)U^{(i)}(\mathbf{r}, k) = 0 \tag{3.4}$$

on substituting the expression for $U(\mathbf{r}, k)$ into (3.3) and using (3.4), the scattered field satisfies the equation

$$(\nabla^2 + k^2)U^{(s)}(\mathbf{r}, k) = P(\mathbf{r}, k)U(\mathbf{r}, k), \tag{3.5}$$

The one-dimensional depth profile of the sample could be obtained from the backscattered sample wave, as described by the scalar scattering theory of light given by Wolf in 1969 [60]. The study indicated that a structure of a weakly scattering object could be determined from its scattering potential through the diffraction theorem. In 1994, Fercher *et al.* approximated the formulation of Wolf for a one-dimension problem, which can be achieved by assuming that the scattering potential of an object to be proportional to the z-axis only [61]. Figure 3.3 shows a drawing of a sample being illuminated by a plane monochromatic laser beam that has a wavevector of $\mathbf{k}^i$ along the negative z-axis.

Incident wavefield $U^{(i)}(-Z, k)$

X

$K^s$

Z

PD

$K^i$

Back scattered field $U^{(s)}(Z, k)$
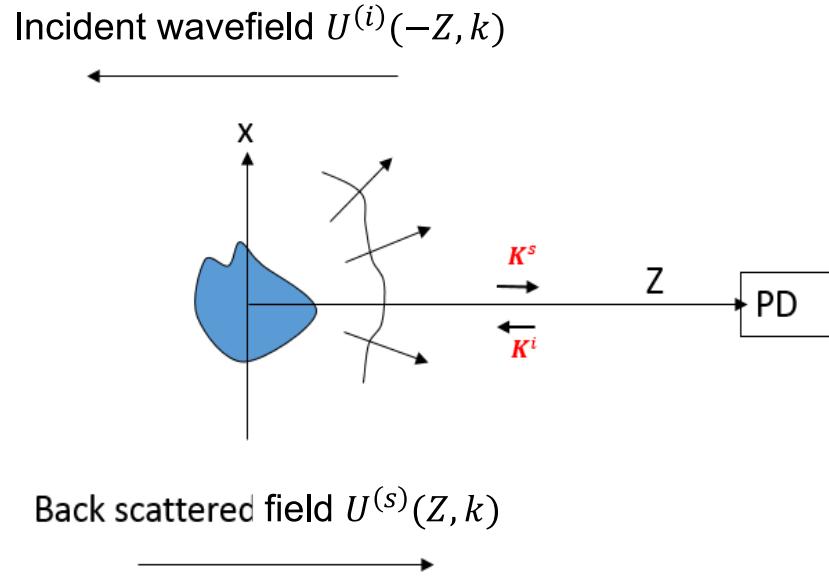
Figure 3.3. A diagram of a sample illuminated by a light wave.

Suppose that the filed incident on the scatterer is a monochromatic plane wave. The time-independent part of the incident field is then given by the expression

$$U^{(i)}(-Z, k) = A^i e^{jk^i Z} \tag{3.6}$$

where $A^i$ is a constant that represents the amplitude of the incident light, $|\boldsymbol{k}^i|$ is the wavenumber of the illuminating wave and $|\boldsymbol{k}^i| = k = 2\pi/\lambda$ is the wavenumber. The scattered filed $U^{(s)}(Z, k)$ can be written in terms of Greens function $G(Z - z', \boldsymbol{k}^s) = \frac{e^{-jk^s|Z-z'|}}{|Z-z'|}$ as follows [56]

$$U^{(s)}(Z, k) = W \int_{z'} P(z', k)\, U(z', k) G(Z - z', k) dz', \tag{3.7}$$
$$= W \int_{z'} P(z', k)\, U(z', k) \frac{e^{-jk^s|Z-z'|}}{|Z - z'|} dz',$$

30

where $W$ is a constant factor that represents the scattering potential in the $x$ and $y$ direction, $Z'$ is the distance from a specific point in the object to the scatterer inside the volume, and $Z$ is the position distance between the detector and the scatterer point inside the object. Using the first-order Born approximation and the far-field approximation, an expression for a one-dimension sample wave is obtained

$$U^{(s)}(Z,k) = \frac{A^i W}{2Z} e^{-jkZ} \int_{-2z_{min}}^{2z_{max}} P(z',k)e^{jkz'} dz' \qquad (3.8)$$
$$= \frac{A^i W}{2Z} e^{-jkZ} \mathcal{F}_{z'}\{P(z',k)\}$$

where $\mathcal{F}_{z'}\{P(z',k)\}$ is the Fourier transform of the scattering potential of the object.

## 3.1.2    Obtaining the Complex Interferogram Signal Using a Swept-Source Quadrature OCT

In conventional OCT, the recorded data is the real part of the complex interference signal between reference and sample arm wavefields. Assuming that the incident wavefield is a plane wave, the wavefield back-reflected from the reference arm can be described as

$$U_r(z_{ref},k) = A^i e^{-jkz_{ref}} \qquad (3.9)$$

where $z_{ref}$ is the length between the detector and the reference mirror. As the wavelength of the swept-source is varied, the optical sensor records the interference signal one after the other. The intensity of the interference signal can be calculated as follows

$$I_{OCT}(Z,k) = |U_r(z_{ref},k) + U_s(Z,k)|^2 \qquad (3.10)$$

Substituting (3.8) and (3.9) into (3.10),

$$I_{OCT}(Z,k) = \left|A^i\right|^2 + \left|\frac{A^iW}{2Z}\mathcal{F}_{z'}\{P(z',k)\}\right|^2 \tag{3.11}$$
$$+ 2Re\left\{A^ie^{jkz_{ref}}\frac{A^iW}{2Z}e^{-jkZ}\mathcal{F}_{z'}\{P(z',k)\}\right\}$$

and the interferometric portion of the OCT intensity signal measured for the SS-OCT system can be written as

$$I_{OCT}(Z,k) \propto \left(2\left|A^i\right|^2\frac{W}{2Z}\right)Re\left\{e^{-jk(\Delta z)}\mathcal{F}_{z'}\{P(z',k)\}\right\} \tag{3.12}$$

where $\Delta z = Z - z_{ref}$ is the optical path length mismatch between the reference and sample arms. (3.12) has information only on the real part of the scattering potential.

In the case of swept-source quadrature OCT system, the real ($I_{real}$) and imaginary ($I_{imag}$) parts of the complex interferometric OCT signals ($I_{Quad}$) are formed from the interferogram signals acquired at the two differential detectors $D_1$ and $D_2$. The real and imaginary components of the complex interferometric signal are given by [53]

$$I_{real}(\phi) = D_1(\phi), \quad I_{imag}(\phi) = \frac{D_1(\phi)\cos(\Delta\phi) - D_2(\phi)}{\sin(\Delta\phi)} \tag{3.13}$$

where $\Delta\phi$ is the phase difference between the interferometric signals $D_1$ and $D_2$. The complex interferometric signal is obtained by putting the real and imaginary signals together as $I_{real}(\phi) + jI_{imag}(\phi)$. The OCT signal measured from the SS-QOCT system can be described as

$$I_{Quad}(Z,k) = 2\left|A^i\right|^2\frac{W}{2Z}e^{-jk(\Delta z)}\mathcal{F}_{z'}\{P(z',k)\} \tag{3.14}$$

The difference between (3.12) and (3.14) is that the swept-source quadrature OCT system can measure complex interferogram OCT signal, whereas the standard SS-OCT measures only the

real part.

### 3.1.3  Experimental Setup and Results

Figure 3.4 shows experimental set-up of our swept-source quadrature OCT system. Here, the laser used is the high-speed scanning laser (Santec HSL-20-100-B) with the center wavelength of 1,310 nm and a full scan wavelength of 88.8 nm. The average output power of the laser is 22.2 mW. The coherence length of the swept-source is 20.4 mm, and the scanning rate is 100 kHz. A start trigger is provided to synchronize with the start of each linear wavelength sweep.
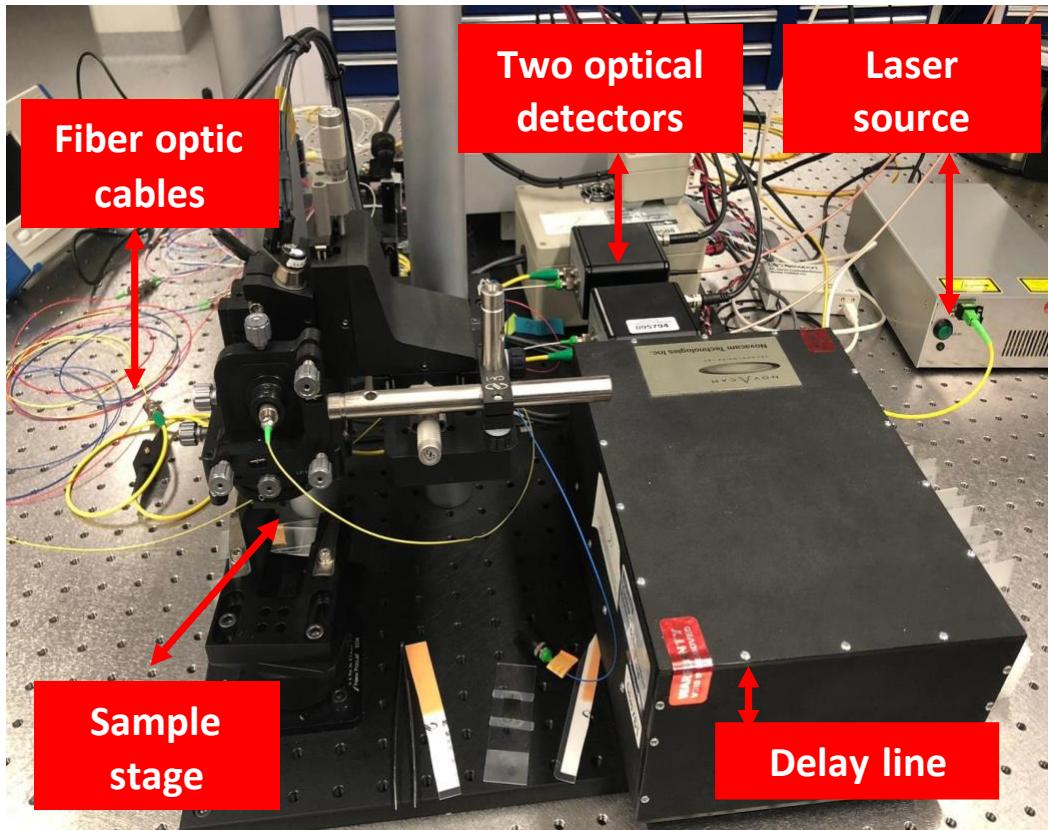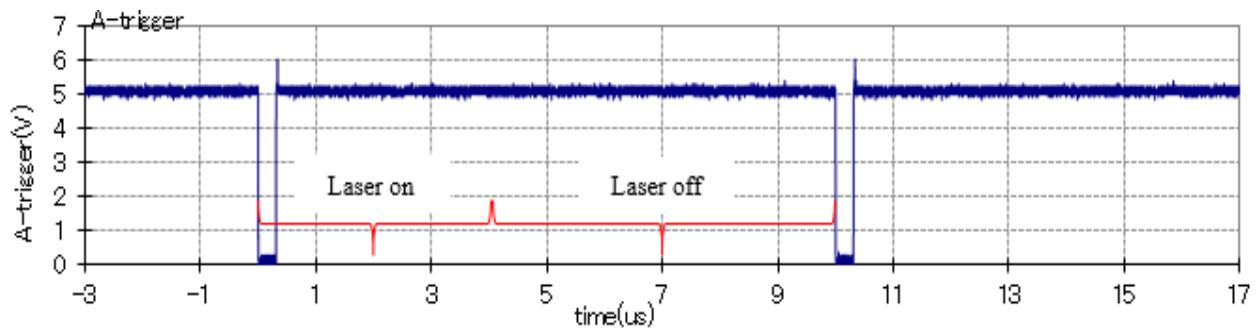


Figure 3.4. Experimental setup.
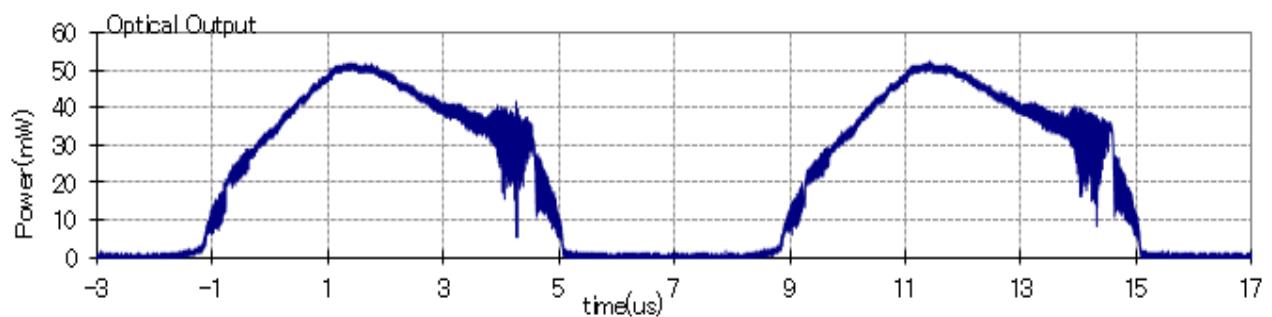
During the 88.8 nm sweep, ranging from 1,270 nm to 1,360 nm, the laser output scan trigger

signal, with a period of 10µs, is used for triggering the acquisition process with the beginning of the wavelength sweep. The sweeping process is characterized by having two stages, "laser on" and "laser off," as represented in Figure 3.5. During the "laser on" stage, the laser is on, and the wavelength sweep takes place (38.9% duty cycle, yielding a 3.89µs). During the "laser off" stage, the laser is off, and the k-space clock signal is used to fill the gap that lasts until the end of the sweeping process.
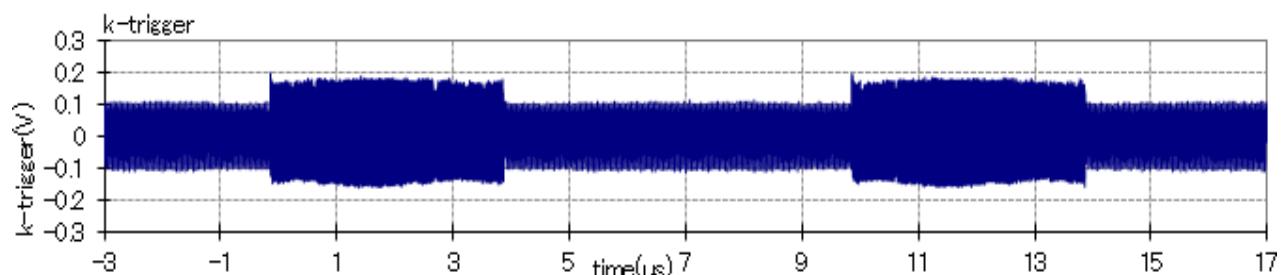
The HSL-20 laser source also provides a clock signal called k-TRG, shown in Figure 3.5 (c), to acquire data with uniform frequency intervals during wavelength sweep. The k-space clock provides data points equally spaced in frequency and are the points at the falling edge (which relies on zero crossings), shown in Figure 3.6 (a). The intensities of the two interference signals are measured by two balanced detectors (New Focus 1817) of 80 MHz bandwidth, after which outputs are digitized through NI 5761 DAQ. Interference fringes acquired from a sample of a mirror are shown in Figure 3.7, where there is $90^{\circ}$ phase shift between the real and quadrature components of the whole complex interferometric signal acquired using optical detectors D1 and D2. Figure 3.7 (b) shows the absolute values of the A-scan in the space domain after our *scaled* NDFT algorithm is applied.
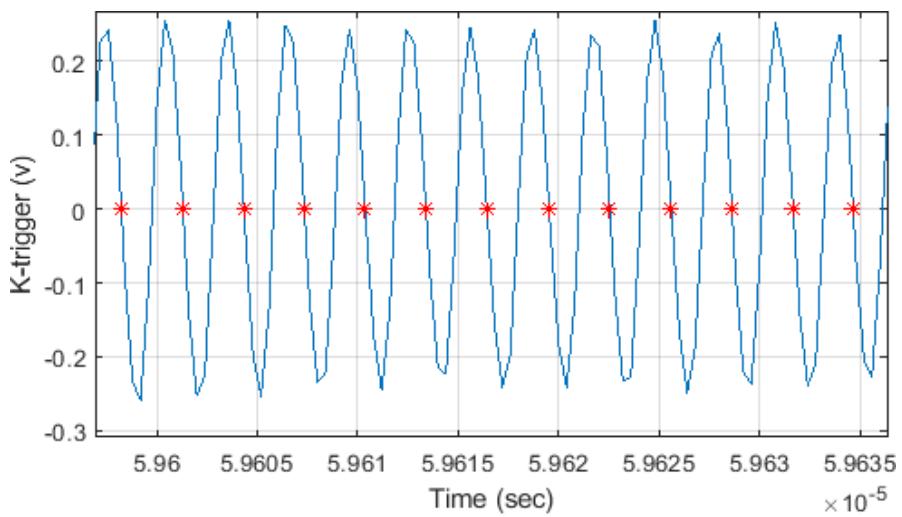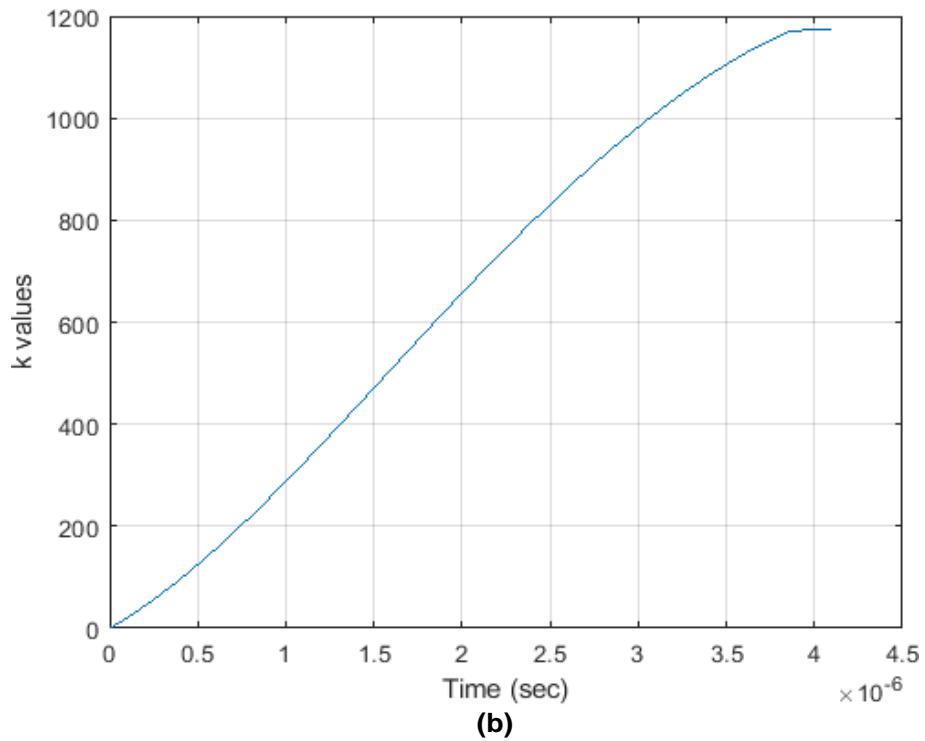
Figure 3.5. (a) A-scan trigger signal, (b) spectral power of the laser (c) K-trigger clock.
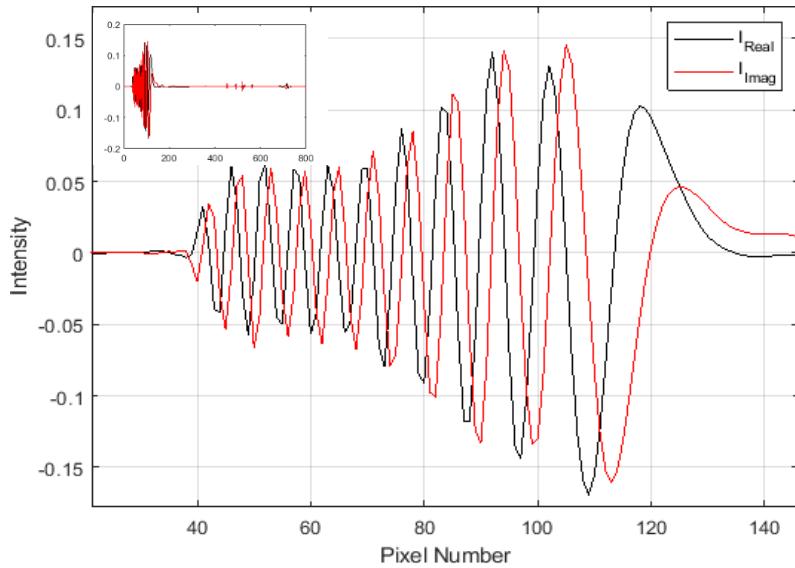
**(a)**
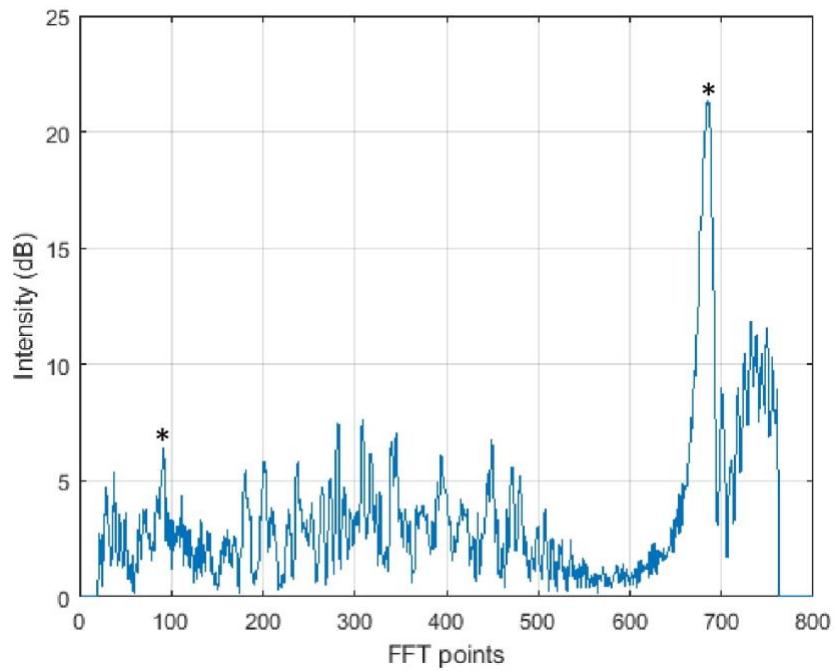


**(b)**

Figure 3.6. (a) the falling edge is used as the zero point. (b) A plot of the time variation in the clock frequency due to the non-linear k-space output.

(a)



(b)

Figure 3.7. A-scan signal (a) the real and imaginary components of the interferometric signal and maintaining $90^{\circ}$ phase difference. (b) A-scan obtained by *scaled* NDFT of the complex signal suppresses the complex conjugate peak.

# Example of an image acquired by our quadrature OCT system

The performance of our quadrature OCT system can be assessed by comparing mirror image resolved B-scans with unresolved B-scans. For this comparison, the OCT image of Kraft paper was acquired using the $3 \times 3$ SS-OCT system shown in Figure 3.8. The images are reconstructed using our *scaled* NDFT.

Figure 3.8 (a) shows the quadrature OCT image of Kraft paper with the mirror image suppressed. Figure 3.8 (a) is reconstructed using the interferometric signal from the two detectors and (3.13) to obtain the full complex signal. It was shown that the complex conjugate artifact had been suppressed in the image.



(a)                                                              (b)
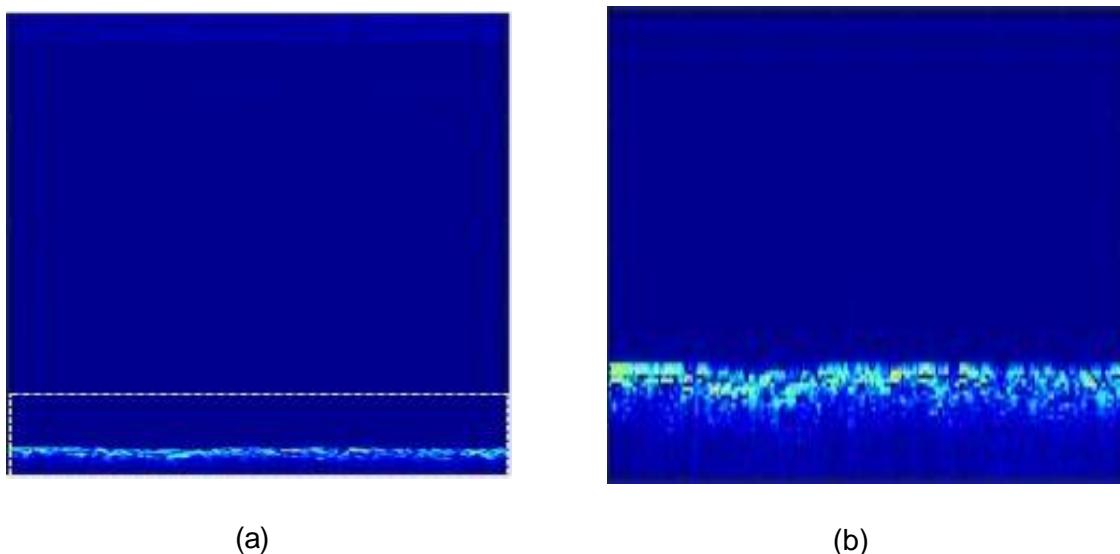
Figure 3.8.  Quadrature OCT images of (a) full-range image of Kraft paper (b) Region ofinterest indicated by the dashed box in (a).

## 3.2    Chapter Summary

A conventional $2 \times 2$ OCT measures the real component of the complex interferogram signal and ignores the quadrature component. Consequently, the Fourier inversion on the real interferometric component produces a complex conjugate artifact. This chapter has experimentally demonstrated the instantaneous acquisition of the complex interferometric signal using a $3 \times 3$ fiber coupler. Using a $3 \times 3$ Michelson interferometer set up, $90^{\circ}$ phase shift was introduced between the interferograms at the output of the detectors. Fourier inversion on the full complex interferometric signal results in a complex conjugate resolved A-scans by suppressing the mirror image. In this experiment, we achieved a mirror image suppression of 27 dB. The real and quadrature components of the full interferometric signal can be used as input in the spectroscopic OCT analysis.

# Chapter 4

# Novel Generalized Image Reconstruction Algorithm for Optical Coherence Tomography

This chapter will briefly explain an overview of swept-source OCT and a review of Frame Theory. First, a description of our generalized method for OCT signal reconstruction from redundant and non-uniformly spaced samples is presented, along with an efficient method to compute our corrected reconstruction transform, i.e., a *scaled* NDFT, using the Fast Fourier Transform.

Then, different advantages of our generalized OCT image reconstruction method are demonstrated by achieving 1) theoretically corrected OCT image reconstruction directly from non-uniformly-spaced frequency domain samples, where we obtained significantly higher image quality compared to one obtained using the standard NDFT; 2) OCT image reconstruction with increased field-of-view using redundant and non-uniformly spaced frequency domain samples.

## 4.1 Swept-Source Optical Coherence Tomography

Swept-source optical coherence tomography (SS-OCT), a Fourier-domain approach, uses a narrow-band laser source whose instantaneous line-width is rapidly swept in wavelength [43, 62]. The system diagram of SS-OCT used in this chapter is shown in Figure 4.1. Compared to TD-OCT, the SS-OCT provides higher imaging speed due to the simpler mechanical design of the fixed reference arm. In TD-OCT and SD-OCT cases, a detector array and spectrometer are used to detect the interference signals. In SS-OCT, neither a detector array nor a spectrometer is used; instead, it uses a single photodetector to record the spectral interference signal, as presented in Figure 4.1.

Also, unlike the SD-OCT, where the spectral components of the interference fridge are spatially separated, in the SS-OCT, the spectral components are encoded in time. This overcomes certain limitations of SD-OCT, such as fringe washout and low resolution, by allowing longer wavelengths. Moreover, at higher imaging depths, SS-OCT provides better sensitivity than SD-OCT. As shown in Figure 4.1, the interferometer is illuminated with light emitted by the wavelength-swept laser source. The first $2 \times 2$ coupler directs 90% of the incoming light into the sample arm and 10% into the reference arm.

The light reflected from the reference and sample arms are then redirected into another $2 \times 2$ coupler, and a balanced photodetector detects the interference of the two wavefields. The detected analog interference OCT signal is then converted into a digital signal using a data acquisition board. The OCT fringe data are then sent to the host computer, where all signal processing is performed. Moreover, the photodetector samples the recorded signal at equal spectral intervals. Each wavelength scan produces depth information from the interference pattern by reflection at different depths in the form of an A-scan. An A-scan is simply a one-dimensional image of the sample at a specific depth. A cross-sectional image of the microstructure of the sample can be obtained by integrating multiple A-scans.
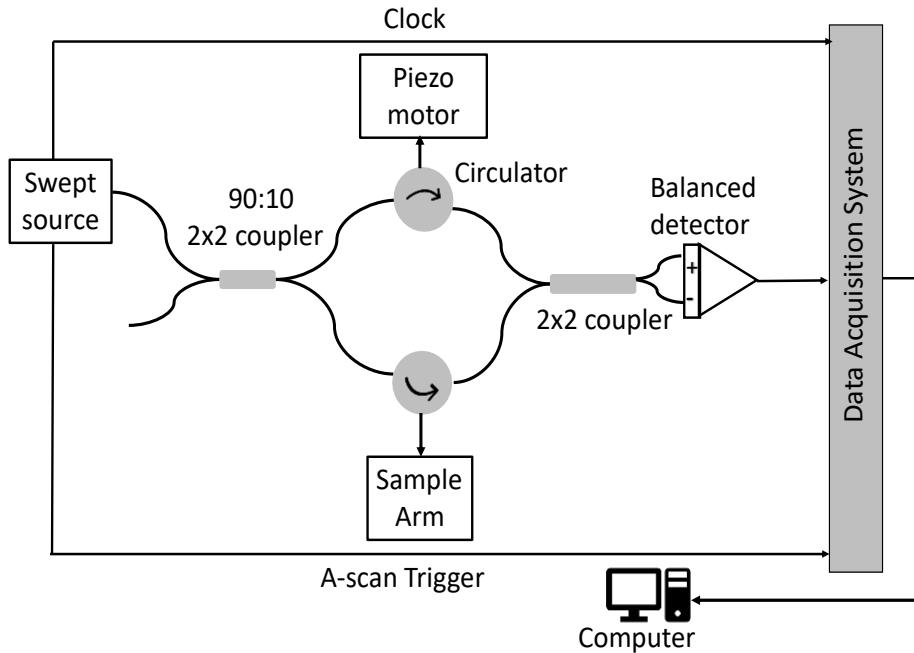
Figure 4.1. System diagram of SS-OCT. The piezo motor is used to change the optical path in the reference arm. The circulator differentiates the light fields moving opposite directions inside the respective optical fibers. The swept laser source, besides the light, also provides two signals called A-scan trigger and clock which are useful for signaling the beginning of a new A-scan and re-sampling of OCT data sets respectively.

Image reconstruction in Fourier domain OCT typically involves an inverse Fourier transform step applied to its A-scan data. The A-scan data provides the reflectivity profile at the beam focusing spot along the light propagation direction. Typical acquisition of this A-scan data, particularly in SS-OCT, leads to non-uniformly spaced samples in the frequency domain. This is due to the nature of the laser source, where its output frequency is a nonlinear function of time. Therefore, it is common to acquire oversampled, i.e., redundant, A-scan data, from which critically sampled, i.e., non-redundant, and uniformly spaced frequency domain samples could be obtained. To avoid the inefficiency of acquiring redundant A-scan data only to overcome this nonuniform sampling issue, OCT image reconstruction using the Nonuniform Discrete Fourier Transform

(NDFT) has been reported [63].

In this thesis, we use Frame Theory to develop a generalized OCT image reconstruction method using redundant and non-uniformly spaced frequency domain samples. Our method includes, as special cases, OCT image reconstruction using non-redundant samples, uniformly spaced samples, or both. This method also demonstrates and corrects a theoretical error in previously published results related to OCT image reconstruction using the NDFT. To demonstrate the advantage of using our corrected OCT image reconstruction method, i.e., a *scaled* NDFT, compared to using the NDFT, we compare OCT images reconstructed from the same non-redundant and non-uniformly spaced frequency domain samples, using both methods.

## 4.2  Brief Review of Frame Theory

A frame is a generalization of a basis in a vector space. Frame Theory, originally developed by Duffin and Schaeffer, is a powerful mathematical tool for studying redundant linear signal representations. i.e., to represent it using a larger number of coefficients than its dimension [64]. In a Hilbert space, **H**, a frame is a generalization of the familiar notion of a Riesz basis. A set of linearly independent vectors $\{\phi_n^{basis}\}_{n=1,2,\dots,N}$ in any **H** with dimension, *N*, could be considered a basis for **H**. Let $f$ be an *N*-dimensional vector $f \in$ **H**, $\langle\cdot,\cdot\rangle$ be an inner product, and $\|\cdot\|$ its induced norm. Let $\Phi^{basis}$ be the basis analysis operator defined as $\Phi^{basis} f = \langle f, \phi_n^{basis}\rangle$. Therefore, $f$ could be represented as

$$f = \sum_{n=1}^{N} \langle f, \phi_n^{basis}\rangle \, \tilde{\phi}_n^{basis} \tag{4.1}$$

where $\{\tilde{\phi}_n^{basis}\}_{n=1,2,\dots,N}$ are the dual basis vectors of $\{\phi_n^{basis}\}_{n=1,2,\dots,N}$ that are given by

$$\langle \phi_n^{basis}, \tilde{\phi}_m^{basis} \rangle = \begin{cases} 1 & n = m \\ 0 & n \neq m \end{cases} \tag{4.2}$$

Therefore, as a special case, the dual basis vectors for any complex-valued orthonormal basis are simply the complex conjugates of its vectors. An element set $\{\phi_n\}_{n \in \Gamma}$, where the index set $\Gamma$ could be finite or infinite, is called a frame in the Hilbert space **H** with bounds $0 < A \leq B$ if and only if [64]

$$A\|f\|^2 \leq \sum_{n \in \Gamma} |\langle f, \phi_n \rangle|^2 \leq B\|f\|^2 \tag{4.3}$$

where $f \epsilon$ **H** is any vector representing a bandlimited signal, $\|\cdot\|$ is its induced norm, and when $A = B$, the frame is said to be tight. We note that the frame condition (4.3) could be satisfied by $\{\phi_n\}_{n \in \Gamma}$ that are either 1) $N$ linearly independent vectors (a basis); or 2) larger than $N$ linearly dependent vectors (a frame). Therefore, a frame in a linear finite dimension inner product space is a generalization of a basis that allows for a potentially redundant linear representation of any vector in this space. In this case, $f$ could be represented as

$$f = \sum_{n \in \Gamma} \langle f, \phi_n \rangle \, \tilde{\phi}_n \tag{4.4}$$

where $\left\{ \tilde{\phi}_n \right\}_{n \in \Gamma}$ are the dual-frame vectors of $\{\phi_n\}_{n \in \Gamma}$ that are given by $\tilde{\phi}_n = (\mathbf{\Phi}^*\mathbf{\Phi})^{-1}\phi_n$, where $\mathbf{\Phi}$ is a matrix whose rows are $\{\phi_n\}_{n \in \Gamma}$, and $*$ denotes Hermitian transpose. If the frame condition (4.3) is satisfied, then $\mathbf{\Phi}$ is called a frame analysis operator such that $\mathbf{\Phi}f[n] = \langle f, \phi_n \rangle$ are the analysis coefficients. The reconstruction of $f$ from its frame coefficients, $\langle f, \phi_n \rangle$, could be computed with a pseudoinverse projection operator, $\mathbf{\Phi}^+ = (\mathbf{\Phi}^*\mathbf{\Phi})^{-1}\mathbf{\Phi}^*$, where $*$ demotes Hermitian transpose. This projection operator, $\mathbf{\Phi}^+$, is bounded and implements a dual-frame reconstruction of $f$. The dual-frame vectors implementing this projection-based reconstruction

are defined by $\{\tilde{\phi}_n\}_{n\in\Gamma}$,

$$\frac{1}{B}\|u\|^2 \leq \sum_{n\in\Gamma}|\langle u,\tilde{\phi}_n\rangle|^2 \leq \frac{1}{A}\|u\|^2 \tag{4.5}$$

where $\tilde{\phi}_n = (\boldsymbol{\Phi}^*\boldsymbol{\Phi})^{-1}\phi_n$ and the actual single $f$ can be reconstructed by

$$f = \sum_{n\in\Gamma}\langle f,\phi_n\rangle\tilde{\phi}_n = \sum_{n\in\Gamma}\langle f,\tilde{\phi}_n\rangle\phi_n \tag{4.6}$$

For shift-invariant frames, i.e., when $\phi_n$ are shifted versions of a single vector, instead of using $\tilde{\phi}_n = (\boldsymbol{\Phi}^*\boldsymbol{\Phi})^{-1}\phi_n$ in the time domain, the dual-frame vectors could be obtained easily in the frequency domain. In this case, the Fourier transforms of the dual-frame vectors, $\widehat{\tilde{\phi}}_n(k)$, where $k$ denotes the frequency variable, are given by [64]

$$\widehat{\tilde{\phi}}_n(k) = \frac{\widehat{\phi}_n(k)}{\sum_{n\in\Gamma}\left|\widehat{\phi}_n(k)\right|^2} \tag{4.7}$$

## 4.3 Signal Reconstruction from Redundant and Non-Uniformly Spaced Samples

### 4.3.1 Redundant and Non-Uniformly Spaced Samples of Bandlimited Functions as Frame Coefficients

According to the Nyquist-Shannon sampling theorem, non-redundant and uniformly spaced

samples, obtained at, $t_n = nT$, of bandlimited signals with bandwidths, $[-\pi/T, \pi/T]$, could be viewed as the coefficients representing these signals in an orthonormal basis, $\{\phi_n^{basis}(t)\}_{n\in\mathbb{Z}}$ [65]. The basis vectors are given by

$$\phi_n^{basis}(t) = T^{-1/2}\frac{\sin(\pi(t-nT)/T)}{\pi(t-nT)/T} \tag{4.8}$$

where $T$ is the Nyquist sampling interval in the given space of bandlimited functions. Similarly, redundant and non-uniformly spaced samples, obtained at $t_n$ of bandlimited signals whose bandwidths are included in $[-\pi/T, \pi/T]$, could be viewed as the coefficients resulting from representing these signals in a frame, $\{\phi_n(t-t_n)\}_{n\in\mathbb{Z}}$. The frame elements are given by

$$\phi_n(t) = \Lambda_n T^{-1/2}\frac{\sin(\pi(t-t_n)/T)}{\pi(t-t_n)/T} \tag{4.9}$$

where $t_n$ is the arbitrary location of the nth sample, $\Lambda_n = [(t_{n+1}-t_{n-1})/2T]^{1/2}$, and $T$ is once again the *Nyquist* sampling interval in the given space of bandlimited functions. If the maximum sampling distance $\delta$ satisfies

$$\delta = \max_{n\in\mathbb{Z}}|t_{n+1}-t_n| < T \tag{4.10}$$

then the frame is bounded by $A \geq (1-\delta/T)^2$ and $B \leq (1+\delta/T)^2$. We note that $T/\delta$ represents the oversampling ratio, relative to the Nyquist sampling rate, and the scale factor, $\Lambda_n$, in (4.9) accounts for this oversampling and location irregularities of the sampled points.

## 4.3.2 Frame-Based Reconstruction of an OCT A-scan

The reconstruction of an OCT A-scan, $u(z)$, where z is the axial spatial domain variable, from its redundant and non-uniformly spaced frequency domain samples, is equivalent to reconstructing

its Fourier transform, $\hat{u}(k)$, from its frame coefficients, $\hat{u}(k_n) = \langle \hat{u}, \phi_n(k - k_n) \rangle$, followed by an inverse Fourier transform. Therefore, using (4.6)

$$\hat{u}(k) = \sum_{n \in \mathbb{Z}} \hat{u}(k_n) \tilde{\phi}_n(k - k_n) \tag{4.11}$$

For ease of implementation, instead of applying the inverse Fourier transform, we obtain a flipped version of the A-scan by applying the forward transform to (4.11). By using (4.7) we obtain

$$u(-z) = \sum_{n \in \mathbb{Z}} \hat{u}(k_n) \frac{\widehat{\phi_n}(z)}{\sum_{n \in \Gamma} |\hat{\phi}_n(z)|^2} \tag{4.12}$$

where $z$ is the axial spatial domain variable. The Fourier transforms of the frame vectors corresponding to (4.9), but in the frequency domain, are given by

$$\widehat{\phi_n}(z) \quad = \mathcal{F}\{\phi_n(k - k_n)\} = \Lambda_n \hat{\phi}_0(z) e^{-jk_n z} \tag{4.13}$$

where, $\hat{\phi}_0(z)$, is the Fourier transform of the unshifted frame vector $\phi_0(k) = K^{-1/2} \sin(\pi k/K)/(\pi k/K)$, where $K$ is the Nyquist sampling interval in the frequency domain. Substituting (4.13) into (4.12), we have

$$u(-z) = \frac{\hat{\phi}_0(z)}{\sum_{n \in \Gamma} |\hat{\phi}_n(z)|^2} \sum_{n \in \mathbb{Z}} \Lambda_n [\hat{u}(k_n) e^{-jk_n z}] \tag{4.14}$$

Since the Fourier transform of $\sin(\cdot)/(\cdot)$ is a rectangular window, and assuming a finite number of frame expansion coefficients, $N_f$, and then replacing the continuous spatial variable, z, in (4.14) by its corresponding uniformly sampled spatial variable, $z_s = 0, 1, ..., N_T - 1$, we could approximate $u(-z_s)$ as

$$u(-z_s) \cong \frac{1}{N_T} \sum_{n=0}^{N_f-1} [\Lambda_n \hat{u}(k_n)] e^{-jk_n z_s} \tag{4.15}$$

where $N_T$ is the number of Nyquist samples $N_T = \delta N_f / T$. (4.15) is a scaled version of the nonuniform discrete Fourier transform (NDFT) at arbitrary points $k_n$, rather than the standard NDFT used for OCT reconstruction in [63, 66]. We note that, compared to the standard NDFT, the extra scale factor $\Lambda_n$ in (4.15) accounts for both oversampling and location irregularities of the sampled points. We will refer to (4.15) as our theoretically corrected OCT image reconstruction.

### 4.3.3 Frame-Based Reconstruction of an OCT A-scan Using the FFT

The reconstruction of an OCT A-scan using the above scaled nonuniform Fourier Transform, (4.15), has a computational complexity of $N_f f (\log_2 N_f)^2$ [63]. However, we could use O ($N_f$) operations to enable computing (4.15) using the FFT. We could write (4.15) as

$$u(-z_s) \cong \frac{1}{N_T} \sum_{n=0}^{N_f-1} \left[ \Lambda_n \, \hat{u}(k_n) e^{-j[k_n - round(k_n)] z_s} \right] e^{-j \, round(k_n) z_s} \tag{4.16}$$

where $round (k_n) = 0, 1, \dots, N_T - 1$, is the nearest integer to $k_n$ after linearly mapping the measured range of $k_n$ to $[0, \; N_f - 1]$. We note that (4.16) is the Discrete Fourier transform (DFT) of the measured A-scan in the Fourier domain, $\hat{u}(k_n)$, multiplied by a complex-valued frequency-dependent scale, $\Lambda_n e^{-j[k_n - round(k_n)] z_s}$. This resulting DFT could be efficiently computed using the Fast Fourier Transform (FFT) with computational complexity $N_T (\log_2 N_T)$.

### 4.3.4 Theoretically Corrected OCT Image Reconstruction from Non-Uniformly Spaced Frequency Domain Samples

The Fourier inversion step required in SS-OCT is typically implemented using the fast Fourier transform (FFT), a computationally efficient implementation of the discrete Fourier transform

(DFT). One major problem of using a DFT-based inversion method is that equally spaced samples in the frequency domain ($k$-space) are necessary, or else the image quality would be compromised [67]. Equally spaced samples in $k$-space cannot be obtained directly because of the nonlinear relationship between the output frequencies of typical swept laser sources and time [70].

Many hardware and software-based methods for acquiring uniform samples in k-space were described in the literature [63, 65, 68, 69, 70]. One way used an auxiliary Mach-Zehnder interferometer (MZI), with a fixed delay between its arms and a balanced detector. As the wavelength of the laser source is swept, this MZI optical output would be a periodic calibration signal with equidistant maxima and minima in $k$-space [69, 70]. Figure 4.2 shows the MZI signal with equidistant sample points in the frequency domain.



(a)  (b)
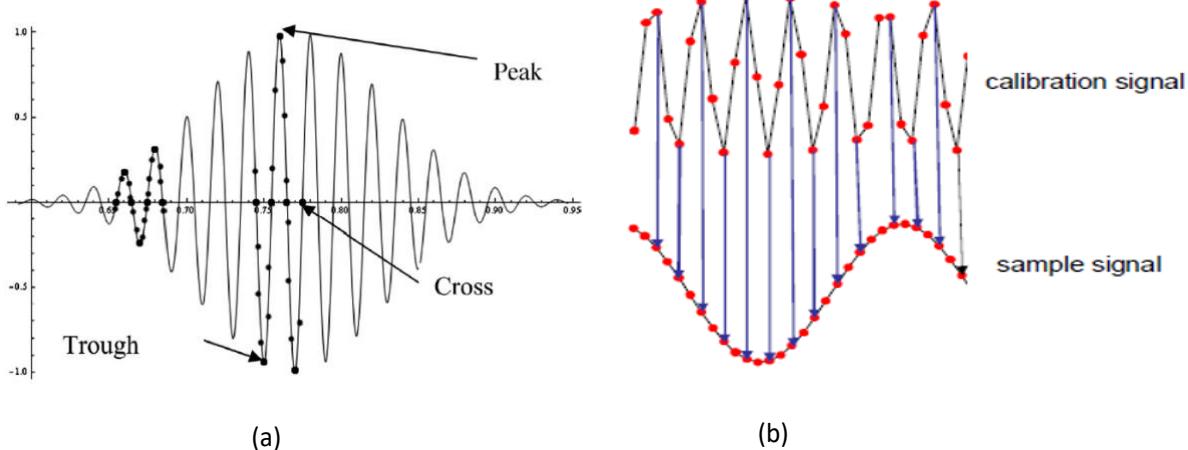
Figure 4.2. (a) illustrative frequency clock signal from the Mach-Zehnder interferometer. The peak, zero cross and trough of the interference fringe signal are equally spaced in frequency domain (b) Signal calibration based on the "nearest neighbor check" algorithm [69].

A time-domain interpolation scheme was implemented by applying a Fourier transform, followed by a low pass filter to equidistant samples of the MZI calibration signal. This calibration signal was reconstructed again by applying an inverse Fourier transform on its single-sided

spectrum. The resulting complex calibration yielded time-dependent wavenumber, $k(t)$, that would be fitted by a $3^{rd}$ order or a higher-order polynomial [71]. Another method that was proposed in [72] used a direct $k$-domain interpolation method based on the spectral phase of the MZI calibration signal. However, MZI based calibration methods add hardware complexity to the system because of the need for an auxiliary interferometer, in addition to the non-efficient use of the optical source since a portion of its power goes to this auxiliary interferometer.

In [63], a Fourier inversion method for SS-OCT based on NDFT was proposed, which is a simpler approach. However, this approach lacked the consideration of the scale factor that compensates for the irregularity of frequency distribution. We corrected this misconception and applied it to the reconstruction of the signal, as presented in the previous section, thus compensating for the irregularity of the frequency distribution in $k$-space that was produced due to the nonlinearity of the output frequencies from the swept-source with time.

The implementation of our *scaled* NDFT, (4.15), requires the knowledge of the time-frequency relationship for the output of the swept-source tunable laser. The relationship between frequency output from the wavelength-swept laser source and time, $f(t)$, can be obtained through the investigation of, $\lambda_s(t)$, the relation between the wavelength and time. Assume the relationship between the wavelength of the output of the used laser and time is a third-degree polynomial, i.e.,

$$\lambda_s(t) = \lambda_0 + at + bt^2 + ct^3 \tag{4.17}$$

A data fitting problem can be solved to obtain the coefficients $a, b, c$ from wavelength measurements. The interference fringes output of the MZI balanced detector can be expressed as follows:

$$I_{MZI} \propto cos(\Delta\phi(t)) = \cos\left(\frac{2\pi d}{\lambda_s(t)} - \frac{2\pi d}{\lambda_0}\right) \tag{4.18}$$

where $\Delta\phi(t)$ is the phase shift difference between the sample and reference arms of the MZI. The

least-squares method fits this MZI model to the measured MZI signal $y_{MZI}(t)$ in such a way that the weighted errors between the model and the measured signal are minimized as follows

$$E = \underbrace{min}_{a,b,c,\lambda_s} \|I_{MZI} - y_{MZI}(t)\|^2 \tag{4.19}$$

hence, from $\lambda_s(t)$ we can obtain $f(t)$ of our swept laser source through a nonlinear relationship. Gauss-Newton method was used to solve (4.19), and the polynomial coefficients $a, b, c$ were obtained. The wavelength-time relation can be written as

$$\lambda_s(t) = \lambda_0 + 0.00225t + 1.9812 \times 10^{-6}t^2 + 1.999 \times 10^{-9}t^3 \tag{4.20}$$

where $\lambda_s$ and $t$ are in nanometres and nanoseconds, respectively. Using $\lambda_0 = 1250$ nm, (4.20) could be approximated as a linear function

$$\lambda_s(t) = 1250 + 0.00225t \tag{4.21}$$

which we used to obtain the needed sampled $k$-space frequencies, $K_s(t)$. After the determination of $\lambda_s(t)$, the required non-linear relationship between the laser output frequency and time, $f(t)$, could be obtained as,

$$f_2(t) = f_1 - 4c \frac{\left(\frac{\Delta\lambda}{\Delta T}t\right)}{\left(2\lambda_1 + \frac{\Delta\lambda}{\Delta T}t\right)^2} \tag{4.22}$$

where $\Delta T$ and $\Delta\lambda$ are the sweeping wavelength duration and tunable wavelength range, respectively, and c is the speed of light in the medium. Once we obtain the $k$-space frequencies, then using (4.15), the depth information of the SS-OCT can be reconstructed. Thus, obtaining the depth information from the spectral data turned out to be NDFT with scale factor. The expression in (4.15) is a generalized form for obtaining the depth information and can be used for either irregular frequency distribution or even in the regular distribution case. In the latter case, the scale

factor $\Lambda_n$ is unity, and the denominator of the scale outside the summation is equal to the number of points, thus becoming the DFT.

The result of our *scaled* NDFT image reconstruction technique can be demonstrated by applying it to SS-OCT interferograms. The result shown in this section is based on an SS-OCT system with wavelength swept-source (Thor Labs, SL1325-P16) spanning the range 1,250 - 1,375 nm with center wavelength 1,325 nm and average output power of 15 mW. The light from the wavelength-swept source is divided by a 90/10 beam splitter into two wavefields. Ninety percent of the power illuminates the sample, whereas the 10 percent travel to the mirror. Then, the beams back-reflected from both arms mixed together in a 50:50 coupler before being detected by a balanced detector of 80 MHz bandwidth, after which the output is digitized through NI 5761 DAQ.

## Generalized reconstruction results using synthetic samples

To quantitively compare the performance of our *scaled* NDFT based image reconstruction method with the performance of standard NDFT based reconstruction, we applied both methods to non-uniformly-spaced, possibly redundant, frequency domain samples that we generated from an OCT image ($512 \times 1000$ pixels) of a human retina obtained from a public dataset [73]. We generated these synthetic samples by Fourier transforming the A-scans of this OCT image and oversampling them by 20 times. Then, non-uniformly spaced, possibly redundant, samples were obtained by non-uniformly selecting samples from these 20 times oversampled Fourier-domain A-scans. The original OCT image of the human retina was then reconstructed from these synthetic samples using both the standard NDFT and our *scaled* NDFT methods.

Figure 4.3 (a) and Figure 4.4 (a) show the original OCT images of a human retina. Reconstructed images obtained by applying the standard NDFT are shown in Figure 4.3 (b) and Figure 4.4 (b), while reconstructed images obtained by applying our *scaled* NDFT to the same non-redundant and non-uniformly-spaced synthetic OCT samples are shown in Figure 4.3 (c) and Figure 4.4 (c). Figure 4.3 (d) and Figure 4.4 (d) show correlation coefficients between

corresponding A-scans of the original image and different reconstructed images.
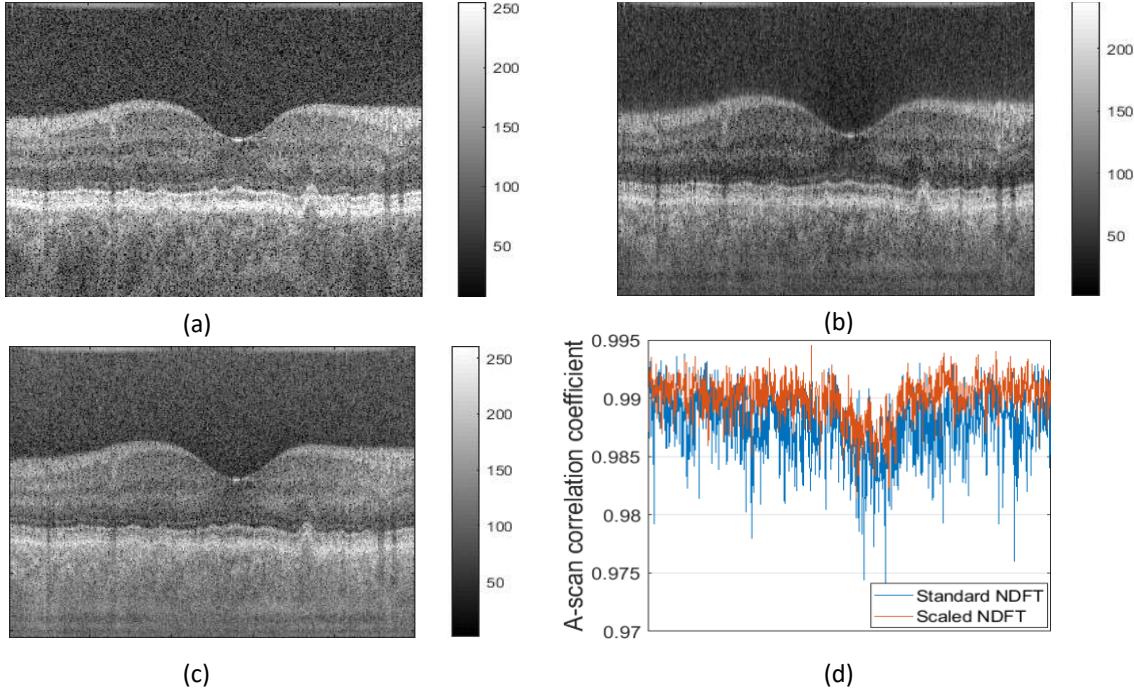


Figure 4.3. (a) Original OCT image of a human retina (b) reconstructed image using the standard NDFT (without scaling) (c) reconstructed image using our *scaled* NDFT (d) correlation coefficients between the A-scans of the original image and their corresponding A-scans in each reconstructed image.

From Figure 4.3 and Figure 4.4, we note that, compared to the images reconstructed using the standard NDFT, the images reconstructed using our *scaled* NDFT are clearer overall and have better-defined edges. This is quantitatively confirmed by the average value of the correlation coefficients between corresponding A-scans in the original images, and the images reconstructed using the standard NDFT (Figure 4.3 average value = 0.9889 and Figure 4.4 average value = 0.9733) and using our *scaled* NDFT (Figure 4.3 average value = 0.9905 average and Figure 4.4 average value 0.9867). This is a quantitative demonstration of the benefit of using our *scaled* NDFT for OCT image reconstruction.
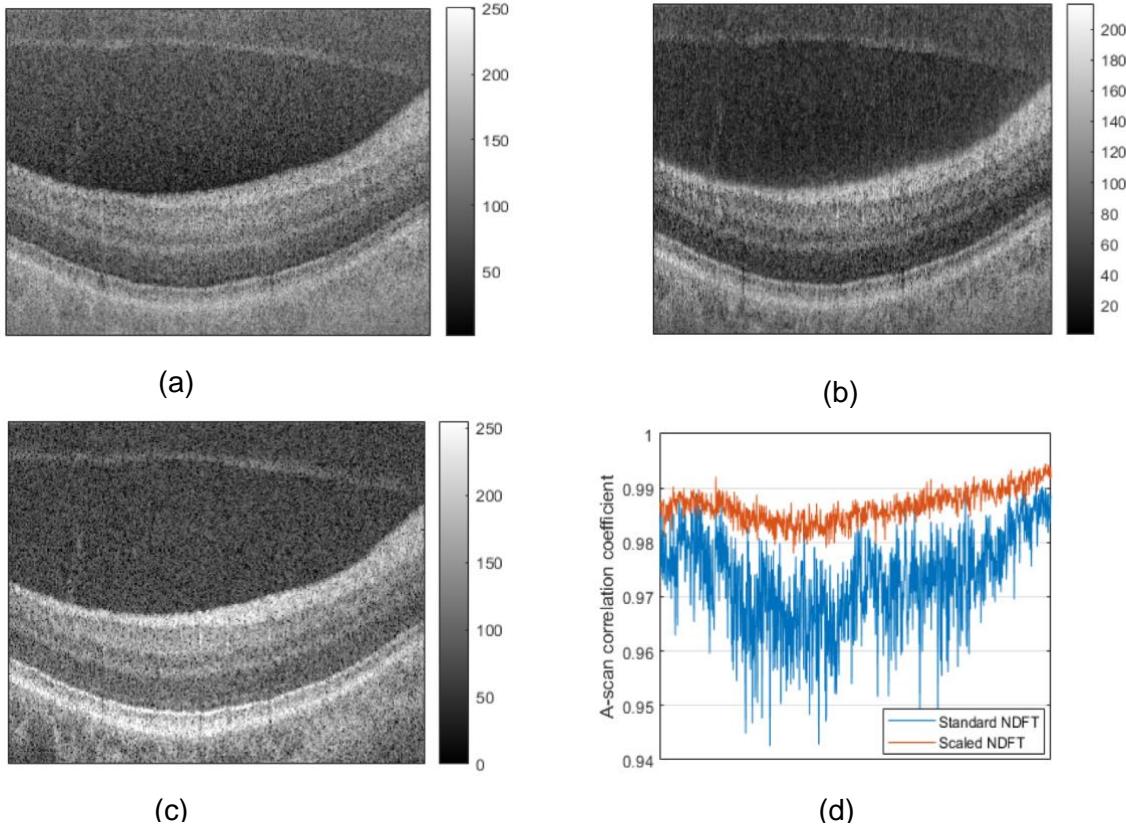
Figure 4.4. (a) Original OCT image of a human retina; (b) reconstructed image using standard NDFT (without scaling); (c) reconstructed image using our *scaled* NDFT; (d) correlation coefficients between corresponding A-scans of the original image and each reconstructed image.

Figure 4.5 shows the Bland-Altman plot comparing A-scans in the original image, and the images reconstructed using both the standard NDFT and our scaled NDFT methods. The red line represents the mean of the difference between the two A-scans, and the blue lines represent the limits of agreement (mean $\pm$ 2standard deviation of difference). Figure 4.5 (a) and Figure 4.5 (b) show a mean difference (bias) of -3.49 and 26.63 were introduced between corresponding A-scan of the original image and image reconstructed using scaled NDFT and standard NDFT respectively. Figure 4.5 (a) shows that 95% of the differences of the two A-scan points lie within $\pm$ 2 standard deviation (standard

deviation= 22.641) of the mean difference.  Figure 4.5 (c) shows the bias between all the A-scans of

the original image and their corresponding A-scans in each reconstructed image. The average bias for

images reconstructed using scaled NDFT and standard NDFT are -7.3499 and 20.5829 respectively.
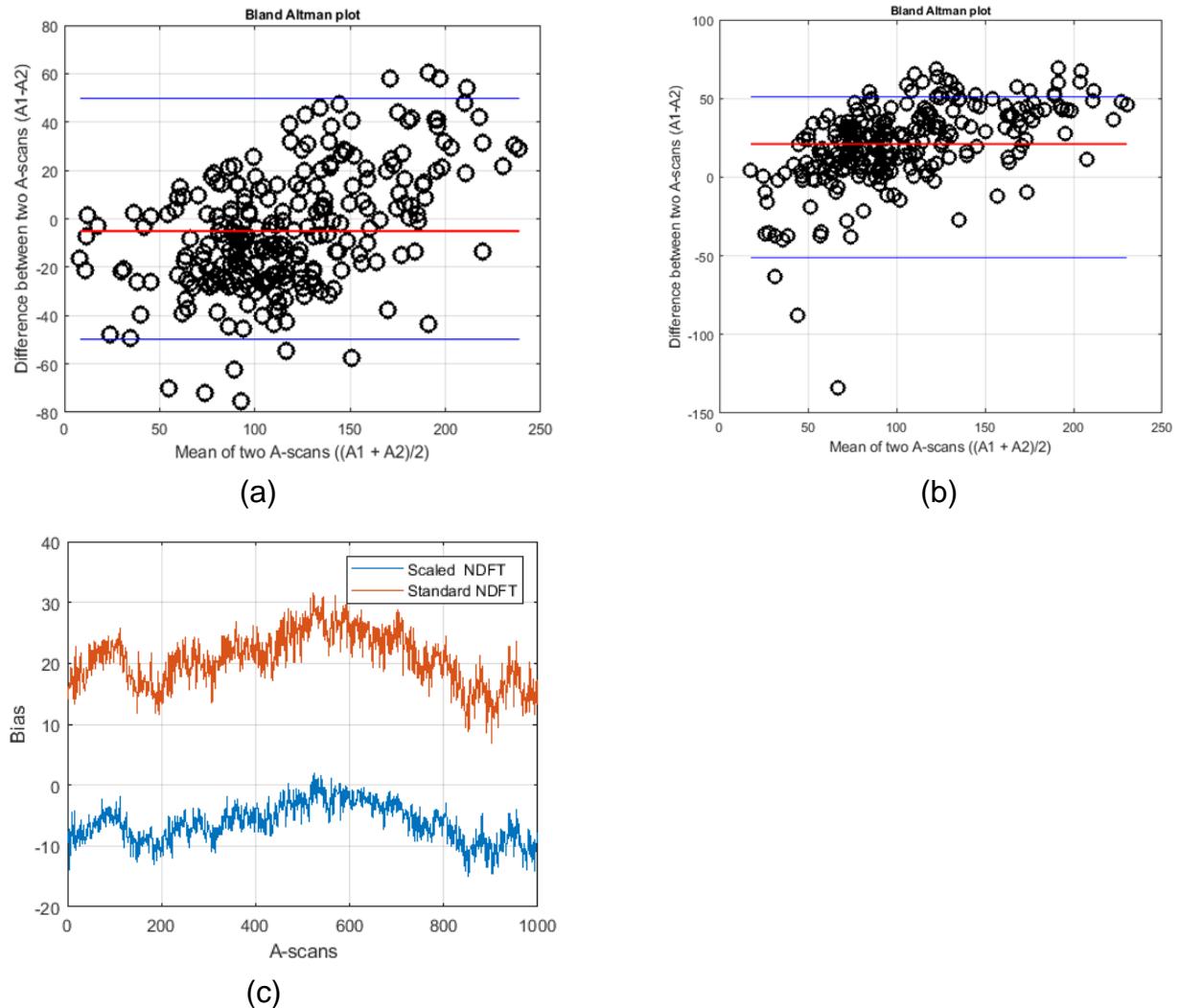


Figure 4.5. A Bland-Altman plot comparing A-scans in the original image, and the image reconstructed using a) our *scaled* NDFT method; (b) standard NDFT method; (c) bias between all the A-scans of the original image and their corresponding A-scans in each reconstructed image.

## Generalized reconstruction results using measured samples

Figure 4.6 (a) shows an SS-OCT image of an Axolotl salamander egg that is reconstructed using the standard NDFT (without scaling), while Figure 4.6 (b) shows the same sample reconstructed using our *scaled* NDFT algorithm. For the standard NDFT algorithm, the scale factor $\Lambda_n$ is unity. On the other hand, for the *scaled* NDFT, the scale compensates for the irregularity in the frequency distribution.
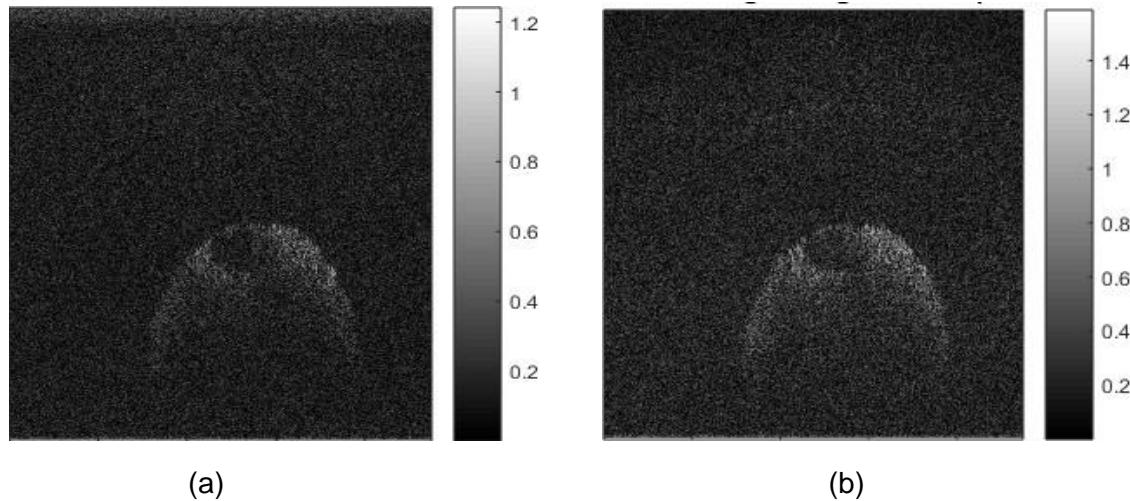


Figure 4.6. Reconstructed OCT image of a salamander egg using: (a) standard NDFT (without scaling); (b) our scaled NDFT.

Using our *scaled* NDFT, the image reconstructed is clearer and has better-defined edges than its corresponding, with the same sampling rate, for the one reconstructed using the standard NDFT. This declares that our algorithm is not only simpler because it does not need extra hardware for calibration but also better since the calibration process does not guarantee perfectly uniform frequencies while our algorithm compensates for the irregularity in the frequency distribution.

## 4.4 OCT Image Reconstruction with Increased Filed-of-View Using Redundant and Non-Uniformly Spaced Frequency Domain Samples

The SS-OCT measures the real part of the complex interferometric OCT signal and ignores the phase (quadrature) component. Fourier inversion on the real part only typically produces a potentially overlapping conjugate image, which consequently leads to inaccurate image interpretation and low image quality. Moreover, the overlapping could be avoided by restricting the object to have its highest reflectivity at its surface. However, this restriction might not be fulfilled when imaging a very thin object placed on highly reflective surfaces or when imaging an object containing a contrast agent with high reflectivity. Several studies have demonstrated the great value of avoiding the overlap in different OCT applications, such as in vivo retinal OCT imaging of human eyes [74], human brain [75], and skin imaging [76]. Moreover, to enhance the image quality and to have a better visualization of the sample, an effective method should be developed to resolve the overlapping images. In this paper, we demonstrated that oversampling the SS-OCT could solve this problem. By recording data points at a higher rate than the minimum required Nyquist sampling rate and using our novel image reconstruction algorithm, the potential overlap of the obtained image and its conjugate mirror image would be avoided without the currently required restriction on the reflectivity profile of the object.

SS-OCT uses a continuous and repetitively tunable narrowband laser source, which is wavelength-swept in time with a single photodetector. Each wavelength scan produces a depth profile from interference pattern by reflection at different depths, where a depth profile of an object is obtained from its backscattered light, as described by the scalar scattering theory of light given by Wolf in 1969 [60]. In 1994, Fercher *et al*. approximated Wolf's formulation by assuming that the scattering potential of the object varies along the axial Z-axis only [61]. As the wavelength of

the swept source is varied, the optical detector records the interference signal one after the other. The intensity spectral interferogram, $I(k)$, measured at the detector is given by [61]

$$I(k) \propto \left(2|A^{(i)}|^2 \frac{W}{4\pi z_s}\right) Re\{exp(-jk\Delta l)\widehat{F_R}(K)\}$$

(4.23)

where $A^{(i)}$ is a constant that represents the amplitude of the incident light, $W$ is a constant factor that represents the scattering potential in the x and y direction, $\widehat{F_R}(K)$ is the Fourier transform of the scattering potential of a sample, $\Delta l$ is the path length difference between the reference and sample arms and $z_s$ is the optical path length of the sample arms. To obtain the depth profile, a Fourier inversion of the recorded interferogram, $I(k)$, due to the interference between backscattered light from the object and a reference beam is required. Because most SS-OCT systems are not quadrature OCT systems [68, 69], where both intensity and phase of this interferogram are measured, the inverse Fourier transform of the intensity of the interferogram, $I(k)$, yields the autocorrelation function (ACF) of the scattering potential rather than the scattering potential FR of the object itself [61]. This ACF could be written in terms of FR as

$$FT^{-1}\{I(k)\} \cong RF_R^*(z_I - Z) + RF_R(z_I + Z) + R^2\delta(Z),$$

(4.24)

where R is the value of the highest reflectivity in the object that is assumed to be located at $z_I$, and $\delta(Z)$ is the Dirac delta function. The second term of the RHS of (4.24) represents the required depth profile shifted by $z_I$, while the first term represents the conjugate mirror depth profile that is also shifted by $z_I$ [61]. Assuming the scattering potential $F_R(Z)$ has length L with support $[Z_{min}, Z_{min} + L]$ as shown in Figure 4.7.
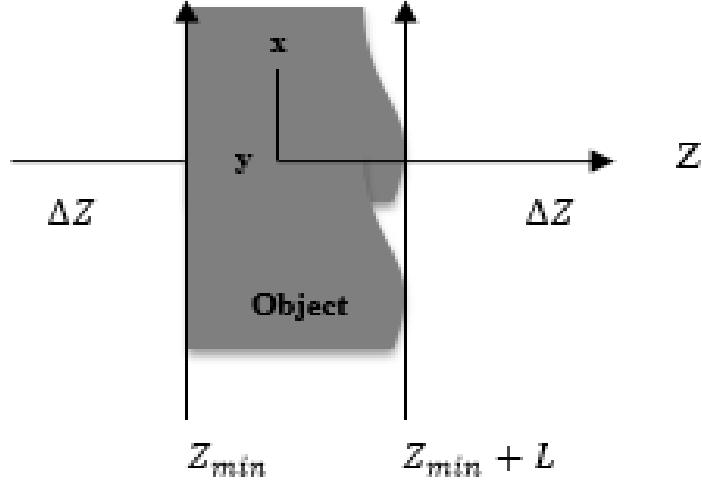
Figure 4.7. A diagram of a sample.

By oversampling the measured interferogram beyond the Nyquist rate, and applying our *scaled* NDFT, a buffer zone, ΔZ, populated by zeros, will be created on both sides of $F_0$ and $F_0^*$. That is, due to oversampling, the support of $F_0(Z)$ will increase to $[Z_{min} - \Delta Z, Z_{min} + L + \Delta Z]$. This buffer zone, $\Delta Z$, would serve as a safeguard to prevent the overlap of the scattering potential $F_0(Z)$ with its conjugate mirror image $F_0^*$, even when both are shifted by different values of $z_I$, which represents the location of highest reflecting point in the depth profile of the object. Hence oversampling the measured interferogram beyond the Nyquist rate could relax the restriction of requiring the highest reflecting point in the object to be at its surface. The flexibility of the location of $z_I$, introduced by oversampling may be useful in some cases when the object contains a contrast agent with high reflectivity between the structures of the object.

(a)                                            (b)
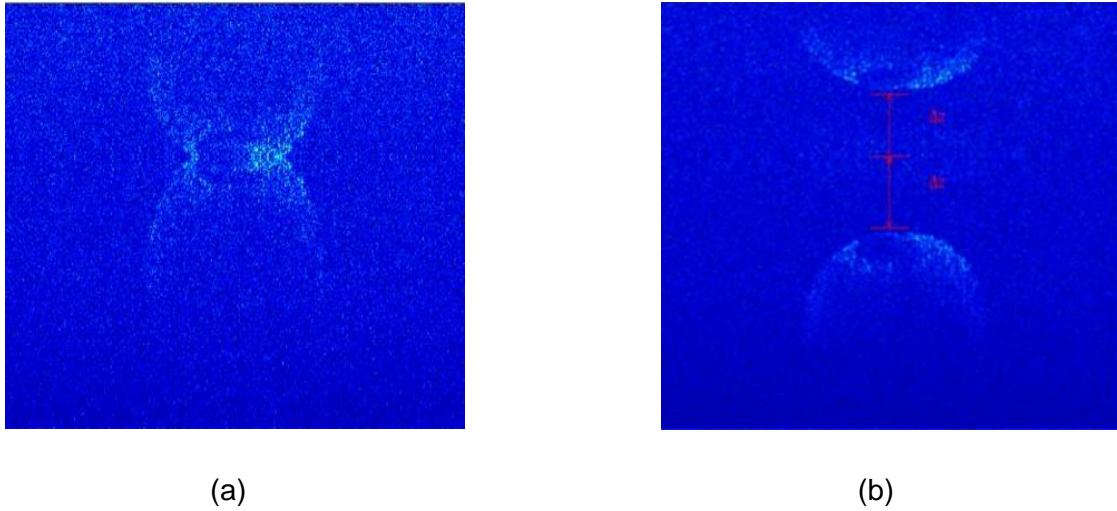
Figure 4.8. Reconstructed image including the conjugate image (a) overlapped and (b) separated by safeguard due to oversampling.

Figure 4.8 shows a comparison between the two cases. Figure 4.8 (a) depicts the overlap between the true reconstruction of the image and its conjugate mirror image. On the other hand, due to the oversampling, (b) shows that the true image is reconstructed and separated by safeguard from its conjugate mirror image, as discussed in the previous section. Therefore, the details of an embryo could be interpreted correctly. It is important to mention that the safeguard increases with the increase of the oversampling rate.

## 4.5    Chapter Summary

Swept-source OCT (SS-OCT) measures backscattered light from different depths within the object due to incident light from a laser source whose frequency is rapidly swept in time. A one-dimensional depth profile of an object (A-scan) is obtained by considering the measured fields due to different incident light frequencies. When the measurements of all frequencies are obtained, the data is inverted into the space domain signal by applying an inverse Fourier transform. Fourier inversion of the measured SS-OCT interferograms typically requires its samples to be equidistant

in *k*-space. However, because of the non-linear relationship between the frequency of a typical wavelength-swept laser and time, the SS-OCT samples obtained are irregularly located in *k*-space. To overcome this problem without any need for interferogram oversampling, an earlier method was demonstrated using the standard nonuniform discrete Fourier transform (NDFT) for image reconstruction in SS-OCT. In this thesis, we used frame theory to develop a more accurate method that applied a scaled nonuniform Fourier transform to the acquired SS-OCT interferograms. Compared to an image obtained using the standard NDFT without scaling, the image obtained by our *scaled* NDFT appeared clearer, and its edges were better defined.

Moreover, Fourier inversion of the obtained SS-OCT interferogram typically produces a potentially overlapping conjugate mirror image, whose overlap could be avoided by restricting the object to have its strongest reflective surface at its own surface. However, this restriction may not be fulfilled when imaging a very thin object that is placed on a highly reflective surface or imaging an object containing a contrast agent with high reflectivity. In this thesis, we showed that oversampling of the SS-OCT signal in *k*-space would overcome the need for such restriction on the object. Our result was demonstrated using SS-OCT images of an Axolotl salamander egg.

# Chapter 5

# Novel Spectroscopy Optical Coherence Tomography Using Compressed Sensing

This chapter applied the theory of compressed sensing to spectroscopy optical coherence tomography (OCT). First, an overview of spectroscopy OCT and the idea of compressed sensing is described. Next, a mathematical formulation of our novel spectroscopic OCT based on compressed sensing is presented. Then, a description of the data required for our spectroscopy OCT algorithm is given.

## 5.1   Spectroscopy Optical Coherence Tomography

Optical coherence tomography (OCT) is a non-invasive imaging modality based on interferometry used to acquire high-resolution 3-dimensional images of biological samples. The applications of OCT are not limited to biomedical imaging but also extend to industrial applications. Regular OCT systems analyze the interferometric signal to produce 3-D images. These images provide information on the microstructures of the sample by looking at the amount of light backscattered by the different points in the sample. However, a great deal of information is encoded in the spectrum of the backscattered light that is not available with intensity-based OCT imaging. Thus, in addition to capturing the cross-section views of samples, OCT can also be used for extracting depth-resolved spectra information, mainly chemical-dependent absorption, and structure-dependent scattering. For example, different tissue types will have different scattering and absorption spectra depending on the cell sizes, blood content, water content, and where the area is oxygenated or deoxygenated.

The conventional OCT can be extended to extract the spectroscopic information from a sample [77, 78]. This is known as spectroscopic OCT. The complex refractive index can be obtained from the interferometric OCT signal using posterior signal processing without changing the system's hardware configurations. The refractive index is essentially a complex number and provides information about the sample's wavelength-dependent absorption and scattering properties. In a low absorption media, the real part of the refractive index refers to the scattering profile of the sample, whereas the imaginary part corresponds to its absorption. The real and imaginary parts of the refractive index are related to each other via the Kramers-Kronig relations. The wavelength-dependent absorption profiles are sensitive to endogenous chemicals such as hemoglobin [79], melanin [80], and exogenous contrast-enhancing dyes [81, 82, 83, 84], which can provide additional functional information. On the other hand, the scattering spectral profiles sense the size, shape, and refractive index of cellular organelles [85, 86] to determine the scattering spectral profiles.

As the light travels inside biological or material samples, some parts of the light spectrum are absorbed by molecules (or chromophores). Hence spectra of the backscattered light will be varied along

with the depth. Therefore, the amplitude and frequency of the backscattered OCT signals vary along with the depth, and this leads to a nonstationary OCT signal. These signals cannot be analyzed directly with Fourier transform. Hence, different hardware and software-based techniques were proposed to extract depth-resolved spectroscopic information from the interferometric OCT signal. The hardware-based spectroscopic OCT constitutes two or more light sources with varying wavelength bands and collects the light separately [87, 88]. However, any hardware-based spectroscopic OCT is expensive and adds complexity to the typical OCT system, as it requires hardware modification of the OCT system.

Another method is software-based spectroscopic OCT that is based on signal processing and does not require hardware modification. These techniques constitute many time-frequency techniques and the least-squares method [89]. Morgner applied Morlet wavelets on conventional time-domain OCT images of a Xenopus laevis (African frog) to demonstrate the depth-resolved spectroscopic information [77]. Xu *et al.* compared three different classes of time-frequency analysis methods on synthesized signals and experimentally acquired time-domain OCT data: Linear Time-Frequency Domain (TFDs), Cohen's class TFDs, and model-based TFDs [90]. In [89], Xu *et al.* obtained the absorption and scattering spectrums from phantoms with a NIR absorbing dye using a least square method. The main drawback of the algorithm was that the absorption or scattering profile of the sample has to be known a prior. In another study [78], Leitgeb *et al.* obtained absorption properties of a sample of spectral-domain OCT using a windowed Fourier transform (WFT). In another study by Yi *et al.* [91], the absorption and scattering spectra of micro-scale structures of spectral OCT samples were analyzed.

Similarly, in 2005 and 2008, Faber *et al.* performed short-time Fourier transform (STFT) analysis on OCT signals to determine localized tissue oxygenation in measurements of the absorption spectra [92]. STFT is relatively simpler to apply and is artifact-free. However, one of the main drawbacks of STFT is the trade-off between the spectral resolution and the axial resolution because of windowing. To overcome this limitation of STFT, Francisco Robles *et al.* proposed a dual window (DW) method by determining the spatial and spectral resolutions independently [93]. The DW

combines two STFTs generated using two different orthogonal Gaussian windows: narrow spectral window and wide spectral window. Recently, Jaedicke *et al.* used the dual-window method proposed by Robles *et al.* to extract the scattering profile of highly scattering media [94].

The existing techniques involve time-frequency analysis, and separation of absorption and scattering profiles from a time-domain or spectral-domain OCT images were demonstrated. However, these current methods disregard the dispersion effect and cannot be applied on swept-source OCT. Swept-source OCT operates at a much faster speed than time-domain OCT or spectral-domain OCT. Furthermore, swept-source OCT overcomes the limitation of spectral-domain OCT, such as fringe washout, low axial resolution, and limited imaging depth range. In addition, the use of time-frequency analysis results in reduced spatial resolution due to windowing effects.

In this section of the thesis project, the sparsity-based spectroscopic OCT data analysis method is described in detail. SS-QOCT is used to acquire a one-dimensional depth profile of an object, i.e., an A-scan. The objective here is to obtain the wavelength-dependent and spatially varying refractive index $n(z, k) = n_s(z, k) + jn_a(z, k)$ from the A-scan. Where $n_s(z, k)$ and $n_a(z, k)$ are the scattering and absorption profiles of the imaged object, respectively. Assuming that the refractive index has sparse (one with only a few nonzero entries) representations in some domain, the two-dimensional refractive index $n(z, k)$ can be obtained using a compressed sensing algorithm. The sparse signal representing the refractive index in the dictionary is obtained by solving a basis pursuit problem, a well-known technique used for sparse source recovery.

## 5.2   The Theory of Compressed Sensing

Compressed sensing (CS) provides an efficient method for analyzing and reconstructing sparse signals from a small number of measurements. CS has established itself as a powerful signal recovery approach in various fields, such as medical and radar applications [95]. Compressed sensing refers to representing an input signal using a few numbers of measurements that possess extra information. It

is known that many real-world images or audio signals are inherently sparse in an appropriate basis called a dictionary. Therefore, signal sparsity can be used as prior information to estimate the signal accurately and efficiently, even if the number of available measurements is smaller than the dimension of the unknown signal. This is the basic idea of compressed sensing [96]. Furthermore, sparse signal representations can also result in simpler signal processing algorithms, for example, signal denoising via simple thresholding operations in a domain where the signal is assumed to be sparse [97]. Also, the computational costs of processing a sparsely represented signal are typically less than the costs of processing its dense counterpart.

Compressed sensing is vital for signal compression. In the conventional signal compression scheme, a signal is reconstructed by first acquiring a significant data size signal, and the remaining insubstantial information is thrown away. Donoho [98] investigated to directly measure the part that will not end up being thrown away. The key objective in compressed sensing is to reconstruct a signal accurately and efficiently from a set of few non-adaptive linear measurements, i.e., the compressed sensing is equivalent to solving the underdetermined linear system problem, which is characterized by having fewer equations than the unknowns. Let us consider a one-dimensional signal $\mathbf{x} \in \mathbb{R}^N$ that has a $K$-sparse representation with respect to the sparsifying basis or frame $\mathbf{\Psi}$ .i.e, $\mathbf{x} = \mathbf{\Psi}\mathbf{\theta}$ and obeys $\|\mathbf{\theta}\|_0 = K$ , with $K \ll N$. Here, $\|\mathbf{\theta}\|_0$ denotes the number of nonzero entries in the vector $\mathbf{\theta}$. The compressed sensing framework consists of measuring the product of the signal against a measurement matrix $\mathbf{\Phi} \in \mathbb{R}^{M \times N}$; the compressive samples of $\mathbf{x}$ can be written as $\mathbf{y} = \mathbf{\Phi}\mathbf{x} + \mathbf{n} = \mathbf{\Phi}\mathbf{\Psi}\mathbf{\theta} + \mathbf{n}$, with $\mathbf{y} \in \mathbb{R}^M$ ($M \ll N$) containing the CS observations. Where $\mathbf{n}$ denotes the noise introduced in the measurement process. The unknown $\mathbf{\theta}$ is obtained by solving the following optimization problems,

$$\widehat{\boldsymbol{\theta}} = \operatorname{argmin} \| \boldsymbol{\theta} \|_1 \text{ subject to } \| \mathbf{y} - \mathbf{\Phi}\mathbf{\Psi}\boldsymbol{\theta} \|_2 \leq \epsilon \tag{5.1}$$

where $\epsilon$ is an upper bound on the $\ell_1$ norm of the noise vector $\mathbf{n}$, and $\|\cdot\|_1$ denotes $\ell_1$ norm, which is equal to the sum of the absolute values of the vector entries. The reconstruction of $\mathbf{x}$ from $\boldsymbol{y}$ is an

underdetermined problem because the number of measurements $M$ is much smaller than the signal dimension $N$. However, if the measurement matrix $\mathbf{\Phi}$ is not correlated with the sparsifying basis $\mathbf{\Psi}$, then we can recover $\mathbf{x}$ from $\mathbf{y}$ accurately. In the field of compressed sensing, there exists a metric known as the mutual coherence that evaluates the performance of CS that gives us a guarantee of the exact reconstruction of sparse signals from a reduced set of measurements. The mutual coherence is the maximum absolute value of the inner product between any two columns of the measurement matrix $\mathbf{\Phi} \in \mathbb{R}^{M \times N}$ and the sparsifying bases $\mathbf{\Psi} \in \mathbb{R}^{N \times N}$ and is given by [105]

$$\mu(\mathbf{\Phi}, \mathbf{\Psi}) = \max_{1 \leq i,j \leq N} \left| \langle \boldsymbol{\phi}_i, \boldsymbol{\psi}_j \rangle \right| \tag{5.2}$$

where $\boldsymbol{\phi}_i$, and $\boldsymbol{\psi}_i$ denoting the $i^{th}$ column of $\mathbf{\Phi}$ and $\mathbf{\Psi}$, respectively. The completely coherent bases have the maximum coherence value, i.e., 1., and the lower bound, known as the Welch bound, is for the completely incoherent bases and is given by

$$\mu(\mathbf{\Phi}, \mathbf{\Psi}) \geq \sqrt{\frac{N - M}{M(N - 1)}} \tag{5.3}$$

The mutual coherence is strictly positive: $\mu(\mathbf{\Phi}, \mathbf{\Psi}) > 0$ and $\mu(\mathbf{\Phi}, \mathbf{\Psi}) \in [N^{-1/2}, 1]$. When $\mu(\mathbf{\Phi}, \mathbf{\Psi}) = N^{-1/2}$, the measurement matrix $\mathbf{\Phi}$ is said to be perfectly incoherent with the sparsifying basis $\mathbf{\Psi}$. A Grassmannian (real) matrix $\boldsymbol{A}$ of size $M \times N$ always achieves the smallest possible mutual coherence, $\mu(\boldsymbol{A}) = N^{-1/2}$. The coherence determines the minimal number of measurements $M$ required for accurate recovery of a signal of length $N$ and is given by [105]

$$M \geq CKN\mu^2(\mathbf{\Phi}, \mathbf{\Psi}) \log(N) \tag{5.4}$$

where $C$ denotes a small positive constant, $N$ is the dimension of the signal to be reconstructed, and $K$ is the signal's sparsity. The smaller is the coherence between $\boldsymbol{\Phi}$ and $\boldsymbol{\Psi}$, the fewer number of measurements is required to reconstruct the signal. Thus, a proper selection of the $\boldsymbol{\Phi}$ and $\boldsymbol{\Psi}$ is needed to minimize the number of measurements required for the accurate recovery of the signal. One of the main practical advantages of coherence-based theory is that it is easy to compute $\mu$ for a given compressed sensing problem. There are many different sparse-based recovery approaches in finding the solution to the compressed sensing system given by (5.1). The techniques can be broadly classified into two primary methods. The first, $\ell_1$-optimization technique such as the basis pursuit (BP) uses linear programming to reconstruct the signal. In contrast, the second method uses greedy algorithms such as the Matching Pursuit (MP) [99, 100]. The second methods are usually much faster than the first ones, but an algorithm that implements the greedy technique will not be guaranteed to find an accurate solution. The $\ell_1$-norm minimization (also known as the Basis Pursuit problem) is a convex optimization technique and always finds the exact solution.

## 5.3  Mathematical Formulation of Our Spectroscopy OCT

The conventional $2 \times 2$ OCT measures the real part of the complex interferometric signal generated between waves reflected from a reference mirror and backscattered from the tissue sample. To keep the linearity of the problem, we need to acquire the real and imaginary components of the interferometric OCT signal. Thus, the complex interferometric OCT signal can be obtained using a swept-source quadrature OCT system. The system's description and implementation are given in chapter 3.  The one-dimensional sample wave is provided by

$$U_s(Z,k) = \frac{A^i W}{2Z} e^{-jkZ} \int_{-2z_{min}}^{2z_{max}} P(z',k) e^{jkz'} dz' = \frac{A^i W}{2Z} e^{-jkZ} \mathcal{F}_{z'}\{P(z',k)\} \tag{5.5}$$

where $A^i$ is a constant that represents the amplitude of the incident light, $W$ is a constant factor that depends on the scattering potential in the $x$ and $y$-direction, $\mathcal{F}_{z'}\{P(z',k)\}$ is the Fourier transform of the scattering potential of a sample, $z'$ is the distance from any point in the object to the scatterer inside the volume, and $Z$ is the length between the position of the detector and the scatterer point inside the object. The scattering potential of the medium $P(z,k)$ is given by

$$P(z,k) = -k^2[n^2(z,k) - 1] \tag{5.6}$$

where $n(z,k) = n_s(z,k) + jn_a(z,k)$ denotes the wavelength-dependent and spatially varying refractive index of the medium. The real part of the refractive index ($n_s(z,k)$) corresponds to the scattering property, whereas the imaginary part ($n_a(z,k)$) corresponds to the absorption profile. The refractive index is directly related to the electric susceptibility, $\chi(z,k) = \chi_{real}(z,k) + j\chi_{imag}(z,k)$, i.e. $n^2(z,k) - 1 = \chi(z,k)$. Hence, the scattering potential can be written in terms of the electric susceptibility, $\chi$, as

$$P(z,k) = -k^2\chi(z,k) \tag{5.7}$$

thus, the scattered light given by (5.5) can be written in terms of the electric susceptibility, $\chi$, as follows

$$U_s(Z,k) = -\frac{A^iW}{2Z}k^2e^{-jkZ}\mathcal{F}_{z'}\{\chi(z',k)\} \tag{5.8}$$

The wavefield back-reflected from the reference arm can be described as

$$U_r(z_{ref},k) = A^ie^{-jkz_{ref}} \tag{5.9}$$

69

where $z_{ref}$ is the distance between the detector and the reference mirror. As the wavelength of the swept-source is varied, the optical detector records the complex interference signal one after the other. The OCT signal $I_{Quad}$ measured from the SS-QOCT system can be described as

$$I_{Quad}(Z, k) = -2|A^i|^2 \frac{W}{2Z} k^2 e^{-jk(\Delta z)} \mathcal{F}_{z'}\{\chi(z', k)\} \tag{5.10}$$

where $\Delta z = 2(Z - z_{ref})$ is the optical path length mismatch between the reference and sample arms. Here, for simplification, we can rewrite the above (5.10) as follows

$$y(Z, k) = ce^{-jk(\Delta z)} \mathcal{F}_{z'}\{\chi(z', k)\} \tag{5.11}$$

where $c = -2|A^i|^2 \frac{W}{2Z}$ and $y(Z, k) = \frac{I_{Quad}(Z,k)}{k^2}$. Furthermore, the intensity of the complex interferometric OCT signal given by (5.11) can be written in discrete matrix format:

$$\boldsymbol{b} = \boldsymbol{F}^T \boldsymbol{\chi} \tag{5.12}$$

where $\boldsymbol{b}$ is $N \times 1$ complex-valued measurement vector, $\boldsymbol{F}^T$ is an $N \times N$ scaled non-uniform discrete Fourier transform (*scaled* NDFT) matrix, and $\boldsymbol{\chi}$ is an $N \times 1$ unknown complex-valued signal.

## 5.3.1 Obtaining Absorption and Scattering Profiles Using Compressed Sensing

To solve the scattering equation given in (5.12) using the compressed sensing framework, we could formulate it as a basis pursuit problem.

$$\min_{\chi} \|\boldsymbol{\chi}\|_1 \quad \text{subject to} \quad \boldsymbol{b} = \boldsymbol{F}^T \boldsymbol{\chi} \tag{5.13}$$

70

Depending on the nature of the signal, one could find the most optimum domain where most of its coefficients are zero. The choice of the dictionary is essential for the sparse signal recovery problem. Notice that $\chi$ is the wavelength-dependent and spatially varying susceptibility of the imaged sample that we want to find. In this thesis, we use Coiflets and union of a discrete cosine transform (DCT) dictionary and Symlet wavelets as optimum dictionaries to find the sparse representation of spectra and texture variations of the susceptibility $\chi$ respectively. The physical nature of spectra of the susceptibility $\chi$ shows that it has a small number of peaks corresponding to resonant absorption peaks. Thus, Coiflets are used as the optimum dictionary for the sparse spectra representation of $\chi$. Coiflets have the most significant number of vanishing moments and produces a sparser representation of the spectrum. Image structures such as edges and textures require redundant dictionaries to be represented more sparsely. In this work, a union of a DCT dictionary and a Symlet wavelets packet with four vanishing moments dictionary $G$ is used to provide a sparse texture representation of the spectroscopic image.

The non-sparse unknown signal $\chi$ can be sparsified in the known two dictionaries as $GXC^T$. Where $C = [c_1, c_2, \ldots, c_n]$ is an $N \times N$ coiflets dictionary whose columns are the atoms, and in general normalized to a unit $l_2$ norm, i.e., $\forall i \in \{1, \ldots, n\}, \|c_i\|^2 = \sum_{k=1}^{N} |c_i[k]|^2 = 1$. $G$ is $N \times 2N$ union dictionary, $X$ is $L \times N$ matrix and represents the coefficients of $\chi$ in the dictionaries. In the above (5.13), the Fourier transform $F^T$ of the complex unknown signal $\chi$ produces a complex component. Its real and imaginary parts are related through the Kramers-Kronig relations. The Kramers-Kronig equations state that the real and imaginary components are Hilbert transform pairs. Hence, the right-hand side of (5.13) can be written as

$$F^T\chi = \text{Re}\{F^T\chi\} + j\text{Re}\{F^T\chi\}H \tag{5.14}$$

where $H$ is $N \times N$ Hilbert matrix. Rewriting (5.14) in terms of the sparse matrix $X$ and dictionaries,

71

(5.14) could be written as

$$F^T \chi = S[\text{Re}\{F^T GXC^T\} + j\text{Re}\{F^T GXC^T\}H] \tag{5.15}$$

Following the Fourier transform in (5.15), the measurement vector $b$ is equivalent to the diagonal vector of $F^T GXC^T$ and $S$ is the selection matrix that selects the diagonal values. Substituting (5.15) into (5.13), we can obtain the sparsest solution for $X$ by solving the following basis pursuit problem

$$\min_{X} \|X\|_1 \quad \text{subject to} \quad b = S[\text{Re}\{F^T GXC^T\} + j\text{Re}\{F^T GXC^T\}H] \tag{5.16}$$

To solve the minimization problem, one could write the matrix linear system of equations as a vector linear system of equations, i.e.,

$$\min_{X} \frac{1}{2}\|S[\text{vec}(\text{Re}\{BXC^T\} + j\text{Re}\{BXC^T\}H)] - b\|_2^2 + \lambda\|X\|_1 \tag{5.17}$$

where $B = F^T G$ is $N \times 2N$ matrix, and $\lambda$ is regularization parameter that quantifies the tradeoff between the squared residual term, $\|S[\text{vec}(\text{Re}\{BXC^T\} + j\text{Re}\{BXC^T\}H)] - b\|_2^2$, and the sparsity level term, $\|X\|_1$. $S$ is $N \times N^2$ selection matrix that selects the diagonal values of a matrix in a vectorized form and is given by

$$S = \sum_{i=1}^{N} I_{i,:} \otimes S^{(i)} \tag{5.18}$$

where $I$ is $N \times N$ identity matrix and $I_{i,:}$ is the $1 \times N$ $i^{th}$ row vector and $S^{(i)}$ is $N \times N$ matrix and its defined by

$$S^{(i)}_{j,k} = \delta_{ij}\delta_{jk} \ (i,j,k \epsilon\{1, \dots, N\}) \tag{5.19}$$

The above (5.17) is commonly known as the basis pursuit problem in signal processing literature, and it can be simplified more by expanding the inner terms in the equation using Kronecker product and vectorization properties as follows

$$vec(\text{Re}\{\mathbf{B}\mathbf{X}\mathbf{C}^T\}) = Re\{(\mathbf{C} \otimes \mathbf{B})vec(\mathbf{X})\} \tag{5.20}$$

and

$$vec(\text{Re}\{\mathbf{B}\mathbf{X}\mathbf{C}^T\}\mathbf{H}) = vec(\text{Re}\{\mathbf{B}\mathbf{X}\mathbf{C}^T\mathbf{H}\}) = Re\{(\mathbf{H}^T\mathbf{C} \otimes \mathbf{B})vec(\mathbf{X})\} \tag{5.21}$$

where $vec(\mathbf{X})$ is a column vector whose length is $2N^2 \times 1$. Let $\mathbf{D} = \mathbf{H}^T\mathbf{C}$ is $N \times N$ matrix. Substituting (5.20) and (5.21) into (5.13), the basis pursuit problem could be written in vectorized form, and thus, the optimization problem would then become

$$\min_{\mathbf{X}} \frac{1}{2}\|\mathbf{S}[Re\{(\mathbf{C} \otimes \mathbf{B})vec(\mathbf{X})\} + \mathbf{j}Re\{(\mathbf{D} \otimes \mathbf{B})vec(\mathbf{X})\}] - \mathbf{b}\|_2^2 \tag{5.22}$$

$$+ \lambda\|\mathbf{X}\|_1$$

Substituting $\mathbf{S}$ given in (5.18) into the above (5.22) and using the Kronecker product property, $(\mathbf{A} \otimes \mathbf{B})(\mathbf{C} \otimes \mathbf{B}) = \mathbf{A}\mathbf{C} \otimes \mathbf{B}\mathbf{D}$, the above (5.22) can be written as follows

$$\min_{\mathbf{X}} \frac{1}{2}\left\|\left[Re\left\{\sum_{i=1}^{N}(\mathbf{C}_{i,:} \otimes \mathbf{B}^{(i)})vec(\mathbf{X})\right\}\right.\right. \tag{5.23}$$

$$\left.\left.+ \mathbf{j}Re\left\{\sum_{i=1}^{N}(\mathbf{D}_{i,:} \otimes \mathbf{B}^{(i)})vec(\mathbf{X})\right\}\right] - \mathbf{b}\right\|_2^2 + \lambda\|\mathbf{X}\|_1$$

where $\mathbf{C}_{i,:} = \mathbf{I}_{i,:}\mathbf{C}$ and $\mathbf{D}_{i,:} = \mathbf{I}_{i,:}\mathbf{D}$ are $1 \times N$ row vectors, and $\mathbf{B}^{(i)} = \mathbf{S}^{(i)}\mathbf{B}$ is $N \times 2N$ matrix with only the $i^{th}$ row being nonzero. In the above (5.23), the summation can be written as Khatri-Rao product that is based on rows-by-rows Kronecker product of two matrices, and it is given by

$$\min_{X} \frac{1}{2} \|[Re\{(C \bullet B)vec(X)\} + jRe\{(D \bullet B)vec(X)\}] - b \|_2^2 \qquad (5.24)$$

$$+ \lambda \|X\|_1$$

where $C \bullet B = (C^T \odot B^T)^T$ is the transposed Khatri-Rao product and $\odot$ is the Khatri-Rao product. The matrix $B$ and $X$ are generally complex-valued. Substituting $B = B_r + jB_i$ and $X = X_r + jX_i$ in (5.24), the inner terms can be expanded as follows

$$Re\{(C \bullet B)vec(X)\} = (C \bullet B_r)vec(X_r) - (C \bullet B_i)vec(X_i) \qquad (5.25)$$

$$jRe\{(D \bullet B)vec(X)\} = j\big((D \bullet B_r)vec(X_r) - (D \bullet B_i)vec(X_i)\big) \qquad (5.26)$$

where $B_r = \text{Real}\{B\}$, $B_i = \text{Imag}\{B\}$ and $X_r = \text{Real}\{X\}$, $X_i = \text{Imag}\{X\}$. Substituting the two equations, (5.25) and (5.26) in (5.24), the basis pursuit problem can be written as

$$\min_{X} \frac{1}{2} \|[(C \bullet B_r)vec(X_r) - (C \bullet B_i)vec(X_i) \qquad (5.27)$$

$$+ j\big((D \bullet B_r)vec(X_r) - (D \bullet B_i)vec(X_i)\big)] - b\|_2^2$$

$$+ \lambda \|X\|_1$$

The measurement vector $b$ is $N \times 1$ complex-valued, and it can be treated simply as real-valued data by stacking the real and imaginary parts together, which doubles the effective number of measurements. For instance, defining the $N \times 1$ vector $b_{re} = \text{Real}(b)$ and the $N \times 1$ vector $b_{im} = \text{Imag}(b)$, we can introduce the $2N \times 1$ column vector $\bar{b}$ formed by $\bar{b} = [b_{re}; b_{im}]$. A similar quantity, $\bar{x}$, can be introduced by stacking $2N^2 \times 1$ vector $vec(X_r)$ and $2N^2 \times 1$ vector $vec(X_i)$ to form a $4N^2 \times 1$ vector $\bar{x} = [vec(X_r); vec(X_i)]$. In addition, the measurement matrix can also be

decoupled into real and imaginary sub-matrices to generate a matrix that is twice times the size of its original size. Thus, the above (5.27) can be rewritten as

$$\min_{\bar{x}} \frac{1}{2} \left\| \begin{bmatrix} (C \bullet B_r) & -(C \bullet B_i) \\ (D \bullet B_r) & -(D \bullet B_i) \end{bmatrix} \bar{x} - \bar{b} \right\|_2^2 + \lambda \|\bar{x}\|_1 \tag{5.28}$$

again, (5.28) can be rewritten as,

$$\min_{\bar{x}} \frac{1}{2} \left\| [\Phi^{(1)} \bullet \Phi^{(2)} \quad -\Phi^{(1)} \bullet \Phi^{(3)}]\bar{x} - \bar{b} \right\|_2^2 + \lambda \|\bar{x}\|_1 \tag{5.29}$$

where $\Phi^{(1)} = \begin{bmatrix} C \\ D \end{bmatrix}$, $\Phi^{(2)} = \begin{bmatrix} B_r \\ B_r \end{bmatrix}$ and $\Phi^{(3)} = \begin{bmatrix} B_i \\ B_i \end{bmatrix}$. To have a Kronecker structure among the matrices $\Phi^{(1)}$, $\Phi^{(2)}$, and $\Phi^{(3)}$ in (5.29), we can introduce a weighting matrix with entries of 0 and 1. Let $W = S^H S$, be a diagonal weight matrix. Weights consist of zeros for the pixels that belong to the zero rows in the dictionary and ones everywhere else. Alternatively, (5.29) could be rewritten as a weighted linear transformation of $\bar{x}$ in terms of the Kronecker product as follows

$$\min_{\bar{x}} \frac{1}{2} \|S\Phi\bar{x} - S\bar{y}\|_2^2 + \lambda \|\bar{x}\|_1 \tag{5.30}$$

where $\Phi = [\Phi^{(1)} \bullet \Phi^{(2)} \quad -\Phi^{(1)} \bullet \Phi^{(3)}]$. $S\bar{y}$ is a new column vector where its non-zero entries correspond to the measurement sample points in $\bar{b}$, and for the pixels that are not available, their values are set to zero in $S\bar{y}$. Each row in the $\Phi$ that has zero weight corresponds to the sample point equal to zero in the vector $S\bar{y}$. The objective here is to estimate the $4N^2 \times 1$ column vector $\bar{x}$ given the $2N \times 1$ measurement vector $\bar{b}$. Due to zero weights, the weighted least-squares problem loses the Kronecker structure for incomplete samples, which could not be efficiently solved using Kronecker-OMP or T-LARS. The above basis pursuit problem can be solved using the weighted tensor least angle regression (WT-LARS) method, which is considered an efficient technique for finding a sparse solution of an underdetermined linear system involving a non-separable weight matrix.

75

## 5.3.2  Data Requirement for Our Spectroscopy OCT Algorithm

In this section, we verify the uniqueness of the solution $\bar{x}$ in (5.30). Our numerical example considers a 1D A-scan signal of size $1024 \times 1$ acquired from the quadrature OCT system. The measurement vector can be doubled by concatenating the real and imaginary components of the full complex interferometric signal. Having observed $\bar{b}$ of length $M=2048$, we can obtain the unknown signal $\bar{x}$ of length, $L = 4N^2 = 4,194,304$, samples by solving (5.30). Here, for fixed sparsifying dictionaries, $C \in \mathbb{R}^{1024 \times 1024}$ and $D \in \mathbb{R}^{1024 \times 2048}$, the matrices $\Phi^{(1)} \in \mathbb{R}^{2048 \times 1024}$, $\Phi^{(2)} \in \mathbb{R}^{2048 \times 2048}$ and $\Phi^{(3)} \in \mathbb{R}^{2048 \times 2048}$ can be obtained. Using (5.3), the minimum coherence parameter for the Kronecker dictionary $\Phi$ is $\mu(\Phi) \geq 1/\sqrt{L} = 0.00045$.    According to (5.4), using the measurements $M=2048$, a minimum of $K = 310$ non-zero coefficients will be obtained, below 1% of the signal length $L$. For example, suppose we want to reconstruct the signal of length $L$ with $K = 209,715$ non-zero coefficients (5%) using the same sensing matrices. In that case, a minimum of $M = 1,388,175$ number of measurements is required. In the thesis, to reduce the number of measurements (or increase the number of non-zero coefficients) needed to reconstruct the unknown signal, we exploit the fact that many signals are known to have sparse gradients. Thus, we developed gradient-based $N$-dimensional signal recovery from incomplete measurements.

## 5.4    Chapter Summary

This chapter applied compressed sensing theory for acquiring spectroscopy information from OCT signals measured by a swept-source quadrature OCT system. The quadrature OCT is used to extract the full complex interferogram signal from an object. Compressed sensing has attracted colossal research interest in various fields. The theory of compressed sensing uses the sparsity constraint of a signal as prior information to obtain an estimate of the signal accurately and efficiently from

compressed versions or incomplete measurements.

The complex scattering potential (or complex susceptibility) of an object is obtained by solving a basis pursuit problem, a well-known technique for compressed sensing. The basis pursuit problem can be solved using the thresholding method or the WT- LARS approach. WT-LARS is a powerful method to efficiently solve the weighted tensor least squares problem for a non-separable weight matrix. Unlike the thresholding methods, WT-LARS does not require a predefined value for the regularization parameter. This chapter also reviews the fundamental theoretical analysis in compressed sensing regarding the number of measurements needed to reconstruct the signal accurately. The coherence determines the number of samples (measurements) required for the accurate recovery of a signal. We developed a gradient-based $N$-dimensional signal recovery algorithm to reduce the number of measurements required for the exact signal recovery. The basic idea of gradient-based signal recovery is that by exploiting the sparsity of the gradient of the signal, one can accurately represent the signal using incomplete samples.

# Chapter 6

# Gradient-Based Multidimensional Signal Recovery from Incomplete Samples in Arbitrary Separable Dictionaries

In this chapter, an algorithm that recovers $N$-dimensional gradient sparse signal from incomplete measurements using Kronecker products of arbitrary transformation domains is presented. Background on the gradient-based sparse signal recovery and multidimensional signal representation using Kronecker product matrices will be discussed. To guarantee exact recovery, we assess the performance of the multidimensional gradient-based signal recovery algorithm by computing the coherence matrix of the Kronecker products of the arbitrary transformation domains. Lastly, the multidimensional gradient-based signal recovery method will be applied to 3D MRI images of the brain and liver.

## 6.1   Sparse Signal Representation

Sparse representation of a signal in a domain in which most of its entries are equal to zero. Sparse signal representation has attracted massive attention in various signal processing fields such as image-inpainting [101], image classification [102], and inverse problems [103, 104]. It is known that most signals of interest have naturally sparse representation with respect to the appropriate domain [98, 101]. Therefore, a signal can be represented with a small number of dictionary elements such that its reconstruction error is minimal. Sparse signal representations can result in simpler signal processing algorithms, for example, signal denoising via simple thresholding operations in a domain where the signal is assumed to be sparse. In addition, sparse signal representation is robust to noise [103]. Furthermore, since sparse signal representation stores only essential information about the signal, the computational costs of processing a sparsely represented signal are typically less than the costs of processing its dense counterpart. Sparse representation can be used for a variety of tasks, including signal denoising [103] and compressed sensing [96].

The goal of sparse signal recovery algorithms is to calculate the sparse representation of a signal given a dictionary. The main challenge arises from the fact that the location of the non-zero values in the sparse representation is unknown. It is important to note that, without the sparsity constraint, the signal recovery problem is equivalent to solving the underdetermined linear system problem, characterized by fewer equations than the unknowns. i.e., the number of measurements required for exact reconstruction is much small than the number of signal samples. Consequently, there are infinitely many solutions that could result in the given measurements. The uniqueness of sparse representation is related to the properties of the dictionary. The dictionary limits the sparsity of signal that is to be sparsely represented by its atoms. Several ways of evaluating the performance of the sparse signal recovery algorithms, such as the mutual coherence, give us a guarantee about the exact reconstruction of the unknown signals from a limited linear measurement. Suppose the signal of interest has a sparse representation in some appropriate dictionary (called sparsifying

bases), where all the dictionary atoms are linearly independent. In that case, an accurate reconstruction can be guaranteed from the incomplete measurements. Linear independence of dictionary atoms can be measured using mutual coherence, which is defined as the maximum absolute inner product between each pair of normalized dictionary atoms [105].

Several algorithms have been studied to approximate the sparse representation problem, which is often formulated as an optimization problem. The two most common methods are basis pursuit ($\ell_1$-minimization problem) and matching pursuit. The basis pursuit is a convex optimization problem and can be solved by using linear programming. In contrast, the second method uses greedy algorithms such as the Orthogonal Matching Pursuit (OMP) [99, 100]. Both methods are computationally expensive, especially for multidimensional signals, even though the second methods are usually much faster than the first ones.

In the past few years, the use of total-variation (TV) regularization instead of the $\ell_1$ term in sparse signal recovery is widely applied [106, 107, 108, 109]. TV of a signal is the sum of the norms of the gradients. To get more sparsity, we can exploit the fact that many signals such as angiograms and MR images of organs are known to have sparse gradients, i.e., signals expected to demonstrate piecewise continuous behavior. Such signals have a slight total variation, and hence, TV-based signal recovery would succeed when the underlying signal has a sparse gradient. TV was first introduced by Rudin *et al*. and used in image denoising problems [110], and since then has been widely applied in different fields such as signal restoration [106] and compressed sensing [111, 112, 113, 114, 115]. Further, for image restoration, recent research has confirmed that its advantages to using the TV regularization instead of the $\ell_1$ term in signal recovery problems as the TV-based signal recovery effectively removes the noise while preserving the edges.

Further, in many applications of practical interest (especially medical imaging such as CT scanners and MRIs), we often wish to reduce the number of measurements and reconstruct the entire original object from a partial set or incomplete Fourier samples [108, 112, 116, 117]. It was demonstrated that since the discrete derivative of an image in a single direction is sparser than the

corresponding TV, the signal recovery algorithms will be more successful in recovering these differences individually [116]. This would reduce the number of measurements required to generate the signal significantly. Further, minimizing the directional derivatives of a signal essentially reduces artifacts, high spatial frequency components and hence suppresses noise in the reconstructed signal.

Most of the sparse signal recovery algorithms have been developed to reconstruct 1-D and 2-D signals, which are sparse on some basis. However, in the past decade, there has been significant interest in critical applications such as hyperspectral imaging and multi-sensor networks that broadly focus on solving signal recovery problems involving high-dimensional data [105]. Also, as the dimensions of the signal increase, the size of the data sets increases exponentially. In this case, the signal recovery algorithm becomes nonlinear, and the construction of the sparsifying bases becomes complicated, especially in multidimensional signals. One of the main drawbacks of the conventional sparse signal recovery framework is that it relies on data representation in vectors. For example, a relatively small three-dimensional (3-D) signal with $256 \times 256 \times 256$ pixels represents a vector with 16,777,216 entries which would impose colossal memory and computation burden to process with the conventional sparse signal recovery vector algorithms. This also leads to considerably huge time and storage memory requirements.

Further, many data types do not lend themselves to vector data representation. Consequently, in multidimensional signals, the conventional sparse signal recovery algorithms are not applicable in practice due to the vectorization of the multidimensional signals. To solve this problem, one may need to characterize the signal structure present on each of its different dimensions in terms of a sparse representation and approximate a sparsifying basis for an entire multidimensional signal that simultaneously accounts for all the types of structure present in the signal. Kronecker product matrices provide a natural means to approximate sparsifying bases and measurement matrices for compressed sensing of multidimensional signals, resulting in a formulation known as Kronecker Compressive Sensing (KCS) [105]. This KCS model for multidimensional signals would allow

81

conventional sparse signal recovery methods to a higher degree. Kronecker product sparsifying bases combine the structures encoded by the sparsifying bases for each signal dimension into a single matrix. Kronecker product measurement matrices can be implemented by performing a sequence of independent multiplexing operations on each signal dimension.

This thesis shows that, by using KCS representation models, we can obtain a convenient representation of the multidimensional signal that allows us to use an efficient compressed sensing algorithm (weighted tensor least angle regression method). Contributions of this work reside on the solid foundation of sparse representations. They have three main contributions: 1) We generalized the theory of gradient-based sparse signal recovery to multidimensional signals using Kronecker products. 2) We confront the challenge of the existing gradient-based sparse signal recovery algorithms, which restrict the measurement matrix to the Fourier domain to arbitrary transformation domains. 3) To guarantee the uniqueness of the solution and exact recovery, we assess the performance of the multidimensional gradient-based signal recovery algorithm by computing the coherence of the Kronecker products of the arbitrary transformation domains. In this work, we used an efficient multilinear sparse signal recovery algorithm, weighted tensor least angle regression (WT-LARS), to recover a multidimensional gradient from incomplete measurements. This chapter is organized as follows. Section 6.2 includes a brief background motivating the formulation of gradient-based sparse signal recovery and reviews Kronecker product matrices that serve as a basis for our proposed method. Specifically, we study how to represent a sparse multidimensional signal using the Kronecker products, and Section 6.3 presents our gradient-based sparse recovery with the Kronecker products method in detail. Section 6.4 provides experimental results.

## 6.2   Problem Formulation

### 6.2.1  Gradient-based Sparse Signal Recovery

In this section, we first formulate the sparse representation of a one-dimensional signal, followed by a general formulation of the multidimensional sparse representation problem. The sparse model assumes that a signal can be accurately represented by a few elements from a basis set called a dictionary. The key objective in sparse signal representation is to reconstruct a signal accurately based on elementary vectors to represent the signals compactly by only a few of these vectors. Mathematically, the problem of sparse representation can be formulated as finding the sparsest solution to an underdetermined problem and can be addressed as follows: let us assume that a vector $\mathbf{y} \in \mathbb{R}^M$ can be represented as a sparse linear combination of the columns of the overcomplete dictionary or sparsifying frame $\mathbf{\Phi} \in \mathbb{R}^{M \times N}$, $N > M$, i.e., $\mathbf{y} = \mathbf{\Phi x}$. The dictionary $\mathbf{\Phi}$ is a matrix containing an atom, i.e., a unit vector of length $M$, in each of its columns ($\mathbf{\Phi} = [\boldsymbol{\phi}_1 \, \boldsymbol{\phi}_2 \, ... \, \boldsymbol{\phi}_N]$) and it is chosen such that the signal of interest is sparse in the dictionary domain. The vector $\mathbf{x} \in \mathbb{R}^N$ are sparse vectors with a minimal number of non-zero approximation coefficients $K = \|\mathbf{x}\|_0 \ll N$ and contains the representation coefficients of the signal $\mathbf{y}$. Here, $\|\mathbf{x}\|_0$ denotes the number of nonzero entries in the vector x.  The sparsest solution can be determined by solving the following sparse representation problem.

$$\hat{\boldsymbol{x}} = \arg \min \| \boldsymbol{x} \|_0 \quad \text{s.t.} \quad \| \mathbf{y} - \mathbf{\Phi x} \|_2 \leq \epsilon \tag{6.1}$$

where $\epsilon$ is the permitted error tolerance in the representation, and $\|\cdot\|_0$ denotes the $\ell_0$ norm, which is equal to the nonzero elements of a vector. The reconstruction problem of obtaining $\boldsymbol{x}$ from $\boldsymbol{y}$ is an underdetermined problem because the number of measurements, $M$, is much smaller than the signal dimension. The uniqueness of sparse representation is related to the properties of the dictionary. The dictionary limits the sparsity of signals that are to be sparsely represented by their

atoms. This sparsity also guarantees stability in recovering the solution of (6.1). If the dictionary atoms of $\boldsymbol{\Phi}$ are linearly independent, then we can recover $\mathbf{x}$ from $\boldsymbol{y}$ accurately. In the field of sparse signal representation, there exists a metric known as the mutual coherence $\mu(\boldsymbol{\Phi})$ that determines the performance of the signal recovery algorithm and gives us a guarantee of the exact reconstruction of sparse signals from a reduced set of measurements. The coherence $\mu(\boldsymbol{\Phi})$ is the maximum absolute value of the inner products between any two columns of the matrix $\boldsymbol{\Phi}$ and is given by

$$\mu(\boldsymbol{\Phi}) = \max_{1 \leq i,j \leq N} \left| \langle \phi_i, \phi_j \rangle \right| \tag{6.2}$$

where $\boldsymbol{\phi}_i$, and $\boldsymbol{\phi}_j$ denoting the $i^{th}$ and $j^{th}$ column of $\boldsymbol{\Phi}$ respectively. The number of samples (measurements) required to recover the signal accurately can be obtained using (6.4). The sparse representation problem given by (6.1) is an optimization problem to find the minimal number of atoms to reconstruct the signal based on $K$ atoms in the dictionary. The sparse representation problem is often solved using either basis pursuit ( $\ell_1$-minimization problem) or matching pursuit, which are the two main approaches in the field of sparse signal recovery. The basis pursuit is a convex optimization problem, whereas the matching pursuit, such as the Orthogonal Matching Pursuit (OMP), uses greedy algorithms [99, 100]. The greedy algorithms are the most efficient and straightforward techniques and gradually increase the selected support of coefficient vector to reduce the reconstruction error.

In the past few years, the use of total-variation (TV) regularization instead of the $\ell_1$ term in signal recovery algorithms is widely applied [106, 107, 108, 109]. Many signals that are not inherently sparse have sparse representation with respect to the total variation. To get more sparsity, we can exploit the fact that many signals such as angiograms and MR images of organs are known to have sparse gradients, i.e., signals expected to demonstrate piecewise continuous behavior. In such cases, instead of minimizing the $\ell_1$ norm, minimizing the TV seminorm $\|X\|_{TV}$, which enforces the necessary TV sparsity of the solution would succeed. In analogy with (6.1),

this yields a method to recover a signal $X \in \mathbb{R}^{N \times N}$ that is $K$-sparse in gradient domain. i.e. $\|TV(X)\|_0 = K$ with $K \ll N$, by using incomplete measurements $Y \in \mathbb{R}^{M \times N}$ $(Y = \Phi X)$ with $M \ll N$. This corresponds to solving the following optimization problem:

$$\hat{X} = \arg\min_{X} \|X\|_{TV} \quad \text{s.t.} \quad \|\Phi X - Y\|_2 \leq \varepsilon \tag{6.3}$$

where $\|X\|_{TV} = \|TV(X)\|_1$ is the total-variation of a discrete-space signal $X(i,j)$ and is defined as the sum of the discrete directional derivative amplitudes of the signal and is given by,

$$(TV(X))_{i,j} = \sqrt{\left|(X_x)_{i,j}\right|^2 + \left|(X_y)_{i,j}\right|^2} \tag{6.4}$$

where $X_x \in \mathbb{R}^{N \times N}$ and $X_y \in \mathbb{R}^{N \times N}$ denote the discrete derivatives of $X$ in the $x$ and $y$ directions respectively, and they are defined pixel-wise as

$$(X_x)_{i,j} = X_{i,j} - X_{i-1,j} \tag{6.5}$$
$$(X_y)_{i,j} = X_{i,j} - X_{i,j-1}$$

The most popular method of solving this problem is to find the signal of the least TV that satisfies the given constraints. $X$ can be obtained by solving the following optimization technique

$$\hat{X} = \arg\min_{X} \|X\|_{TV} + \lambda \|\Phi X - Y\|_2^2 \tag{6.6}$$

It is also possible to combine both the $\ell_1$ and TV norms in the objective function by assuming that the signal $X$ has a sparse representation in both the sparsifying transform $\Psi$ and the gradient domain [118]. The following optimization problem is then solved [118]

$$\widehat{X} = \arg\min_{X} \|\Psi X\|_1 + \alpha \text{TV}(X) \quad \text{s.t.} \quad \|\Phi X - Y\|_2 \leq \varepsilon \tag{6.7}$$

where $\alpha$ trades the transform domain sparsity with the finite-difference sparsity. Similarly, Yin *et al*. has also proposed an algorithm called RecPF to solve recovering sparse MRI images [108]. Several methods were also proposed to solve the TV minimization problem given by (6.3), such as the fast TV convolution method [119]. While the TV-based signal recovery method yields a significant reduction in the number of measurements required to recover a signal, in [116, 117, 120], a different approach was proposed to exploit additional sparsity by reconstructing the image by separately reconstructing the discrete directional derivatives and solve for the image. In [116, 120], it was demonstrated that discrete directional derivatives of medical images are each sparser than the corresponding TV image. Thus, compressed sensing-based image recovery algorithms will be more successful in recovering these differences individually. This would allow the recovery of a signal with a far fewer number of measurements than required by the TV minimization method. References [116, 120] have provided a way to recover an image $X \in \mathbb{R}^{N \times N}$ that is K-sparse in the gradient domain, i.e. $\|\text{TV}(X)\|_0 = K$ with $K \ll N$, by using incomplete Fourier measurements $\mathcal{F}_\Omega X \in \mathbb{R}^{M \times N}$ with $M \ll N$. We note that $\mathcal{F}_\Omega \in \mathbb{R}^{M \times N}$ and $\Omega$ denote 2-D Fourier transform operator and a set of frequencies, respectively. The measurement procedure can be written as $Y = \mathcal{F}_\Omega X + \mathbf{n}$. Where the vector $\mathbf{n}$ is the measurement noise with $\|n\|_2 = \varepsilon$ introduced in the measurement process. The recovery is achieved by solving the following TV minimization problem:

$$\widehat{X} = \arg\min_{X} \|X\|_{TV} \quad \text{s.t.} \quad \|\mathcal{F}_\Omega X - Y\|_2 \leq \varepsilon \tag{6.8}$$

The discrete directional derivatives-based signal recovery algorithm from incomplete Fourier measurements consists of three main steps. 1) It obtains the Fourier observations of the corresponding vertical $\mathcal{F}_\Omega X_y$ and horizontal $\mathcal{F}_\Omega X_x$ edge images from the original Fourier measurements $\mathcal{F}_\Omega X$. 2) It uses one of the compressed sensing algorithms to recover the edge

images $\boldsymbol{X}_x$ and $\boldsymbol{X}_y$. 3) It recovers the actual image from the estimate of its edge using two methods: a least-squares method and a 2-D generalized Poisson solver. All the gradient-based CS signal recovery algorithms proposed in [108, 112, 116, 120] restrict the measurement matrix to the Fourier domain. In this thesis, we generalize the theory of gradient-based sparse 1-D and 2-D signal recovery to multidimensional signals using Kronecker products of arbitrary transformation domains.

## 6.2.2 Multidimensional Signal Representation using Kronecker Product Matrices

Most of the sparse signal recovery algorithms have been developed to measure and reconstruct 1-D and 2-D signals, which are sparse on some basis. However, there is tremendous interest in critical applications such as hyperspectral imaging and multi-sensor networks that broadly focus on solving signal recovery problems involving high-dimensional data [105]. Here, we generalize the sparse signal recovery of a vector to multidimensional signals through the Kronecker structure. For multidimensional signals, the Kronecker structure of the sparsifying basis allows one to implement the signal recovery algorithms efficiently as it involves operations with smaller matrices. The generalization of sparse signal recovery framework to multidimensional is straightforward using the tensor model and Kronecker product structure for the sparsifying bases [121, 105]. i.e., the Kronecker product sparsity bases make it possible to simultaneously exploit the sparsity properties of a multidimensional signal along each of its dimensions. Tensor models have been widely used in mathematics and applied sciences, and the word tensor means a multidimensional array [122]. For example, a vector and matrix are first-order and second-order tensors, respectively, while an $N$-dimensional array is an $N^{th}$ order tensor. Let the tensor $\mathcal{X} \in \mathbb{R}^{I_1 \times I_2 \cdots \times I_N}$ be the unknown $N$-dimensional signal and assume that each $N$-section is sparse in a bases $\boldsymbol{\Phi}^{(n)} \in \mathbb{R}^{I_N \times I_N}; n \in \{1, 2, \dots, N\}$ with sparse coefficients $\theta \in \mathbb{R}^{I_1 \times I_2 \cdots \times I_N}$. Then their *mode-n*

product, $\mathcal{Y}_n \in \mathbb{R}^{I_1 \times I_2 \dots \times I_N}$ is denoted as

$$\mathcal{Y}_n = \mathcal{X} \times_n \mathbf{\Phi}^{(n)} \tag{6.9}$$

where all *mode-n* fibers of the tensor $\mathcal{X}$ are multiplied by the sparsifying matrix $\mathbf{\Phi}^{(n)}$. (6.9 ) could also be written as, $\mathbf{Y}_{(n)} = \mathbf{\Phi}^{(n)} \mathbf{X}_{(n)}$ where $\mathbf{Y}_{(n)}$ and $\mathbf{X}_{(n)}$ are *mode-n* matricizations of tensors $\mathcal{Y} \ and \ \mathcal{X}$, respectively. A *mode-n* product could be thought of as a linear transformation of the *mode-n* fibers of a tensor. Therefore, a multilinear transformation of a tensor $\mathcal{Y}$ could be defined as [123]

$$vec(\mathcal{Y}) = (\mathbf{\Phi}^{(N)} \otimes \mathbf{\Phi}^{(N-1)} \otimes \dots \otimes \mathbf{\Phi}^{(1)})vec(\mathcal{X}) \tag{6.10}$$

where $vec(\mathcal{Y}), vec(\mathcal{X}) \in \mathbb{R}^{I_N I_{N-1} \dots \times I_1}$, and $\overline{\mathbf{\Phi}} = \mathbf{\Phi}^{(N)} \otimes \mathbf{\Phi}^{(N-1)} \otimes \dots \otimes \mathbf{\Phi}^{(1)}$ is the sparsifying separable basis. The sparse signal recovery algorithm guarantees, provided in (5.4), induce corresponding constraints on the Kronecker sparsifying bases $\overline{\mathbf{\Phi}}$. These results provide a link between the signal recovery performance of the Kronecker product matrix and that of the individual matrices comprising the product.

## 6.3 Our Gradient-based Sparse Recovery with Kronecker Products

This section generalized the theory of gradient-based sparse signal recovery of vectors to multidimensional signals using Kronecker products of arbitrary transformation domains. The problem is reduced to solve a large-scale underdetermined linear system of equations possessing a Kronecker structure. We have used a weighted tensor least angle regression (WT-LARS), a generalization of the classical LARS algorithm, to solve the multilinear optimization problem.

## 6.3.1 Problem Formulation

It is relatively straightforward to generalize the computation of the gradients for multidimensional signals. i.e., the gradients can be obtained by computing the discrete derivatives along each direction of the signal space. Given $\mathcal{Y} = \mathcal{X} \times_1 \mathbf{\Phi}^{(1)} \times_2 \mathbf{\Phi}^{(2)} \times_3 ... \times_N \mathbf{\Phi}^{(N)}$ observation, one can obtain the directional derivatives of $\mathcal{X} \in \mathbb{R}^{I_1 \times I_2 ... \times I_N}$ in the arbitrary transformation domains by expressing the derivatives as linear functions of the measurements. The multilinear transformation could also be written as a product of $vec(\mathcal{X})$ and the Kronecker product of matrices $\mathbf{\Phi}^{(n)}; n \in \{1,2, ..., N\}$ as

$$(\mathbf{\Phi}^{(N)} \otimes \mathbf{\Phi}^{(N-1)} \otimes ... \otimes \mathbf{\Phi}^{(1)})vec(\mathcal{X}) = vec(\mathcal{Y}) \tag{6.11}$$

Any particular pixel of $\mathcal{X}$ will be written as $\mathcal{X}_{i_1, i_2, ..., i_N}$ and $\mathcal{X}_n^g \in \mathbb{R}^{I_1 \times I_2 ... \times I_N}; n \in \{1,2, ..., N\}$ denote the discrete directional derivatives of the tensor $\mathcal{X}$ along each direction of the signal space. Thus, the discrete directional derivatives of the tensor $\mathcal{X}$ are defined pixel-wise as

$$\left(\mathcal{X}_1^g\right)_{i_1, i_2, ..., i_N} = \mathcal{X}_{i_1, i_2, ..., i_N} - \mathcal{X}_{i_1-1, i_2, ..., i_N} \tag{6.12}$$

$$\left(\mathcal{X}_2^g\right)_{i_1, i_2, ..., i_N} = \mathcal{X}_{i_1, i_2, ..., i_N} - \mathcal{X}_{i_1, i_2-1, ..., i_N}$$

$$\vdots$$

$$(\mathcal{X}_N^g)_{i_1, i_2, ..., i_N} = \mathcal{X}_{i_1, i_2, ..., i_N} - \mathcal{X}_{i_1, i_2, ..., i_N-1}$$

Referring to the above (6.12), $\mathcal{X}_{i_1-1, i_2, ..., i_N}$ is the shifted version of $\mathcal{X}_{i_1, i_2, ..., i_N}$ along the direction of $i_1$ and can be written in terms of the shift operator $\mathbf{S}$ as $\mathcal{X} \times_1 \mathbf{S}$. Thus, the gradient $\mathcal{X}_1^g$ given in (6.12) can be written as

$$\mathcal{X} - \mathcal{X} \times_1 \boldsymbol{S} = \mathcal{X}_1^g \tag{6.13}$$

Again, multiplying both sides of (6.13) by the transformation domain $\boldsymbol{\Phi}^{(1)}$, we can obtain

$$\mathcal{X} \times_1 \boldsymbol{\Phi}^{(1)} - \mathcal{X} \times_1 \boldsymbol{\Phi}^{(1)}\boldsymbol{S} = \mathcal{X}_1^g \times_1 \boldsymbol{\Phi}^{(1)} \tag{6.14}$$

and the above (6.14) can be written as

$$\mathcal{X} \times_1 \boldsymbol{\Phi}^{(1)}\mathbf{U} = \mathcal{X}_1^g \times_1 \boldsymbol{\Phi}^{(1)} \tag{6.15}$$

where $\mathbf{U} = I - \boldsymbol{S}$ is the difference matrix and its inverse $\mathbf{U}^{-1}$ is the sum matrix given by

$$\mathbf{U} = \begin{bmatrix} 1 & 0 & & \\ -1 & 1 & 0 & \\ & \ddots & \ddots & \ddots \\ & & -1 & 1 \end{bmatrix}_{I_n \times I_n} \quad \mathbf{U}^{-1} = \begin{bmatrix} 1 & 0 & & \\ 1 & 1 & 0 & \\ & \ddots & \ddots & \ddots \\ 1 & 1 & 1 & 1 \end{bmatrix}_{I_n \times I_n} \tag{6.16}$$

Therefore, the gradient signal $\mathcal{X}_1^g$ in the transformation domain $\boldsymbol{\Phi}^{(1)}$ can be obtained from the given observation $\mathcal{X} \times_1 \boldsymbol{\Phi}^{(1)}$ as

$$\mathcal{X} \times_1 \boldsymbol{\Phi}^{(1)} = \mathcal{X}_1^g \times_1 \boldsymbol{\Phi}^{(1)}\mathbf{U}^{-1} \tag{6.17}$$

Thus, the gradient signal in the Kronecker products of transformation domains $\boldsymbol{\Phi}^{(n)}; n \in \{1, 2, \dots, N\}$ can be obtained from the tensor $\mathcal{Y}$ as the following

$$\left(\boldsymbol{\Phi}^{(N)} \otimes \dots \otimes \boldsymbol{\Phi}^{(2)} \otimes \boldsymbol{\Phi}^{(1)}\mathbf{U}^{-1}\right)vec(\mathcal{X}_1^g) = vec(\mathcal{Y}) \tag{6.18}$$

Similarly, the same procedure can be applied to all directions of the signal space to obtain the respective directional derivatives from the given observation tensor $\mathcal{Y}$. Thus, the measurement procedure can be written in terms of the discrete directional derivatives of the tensor $\mathcal{X}$ as the following

$$\left(\boldsymbol{\Phi}^{(N)} \otimes \dots \otimes \boldsymbol{\Phi}^{(2)} \otimes \boldsymbol{\Phi}^{(1)}\mathbf{U}^{-1}\right)vec\left(\mathcal{X}_1^g\right) = vec(\mathcal{Y}) \tag{6.19}$$

$$\left(\boldsymbol{\Phi}^{(N)} \otimes \dots \otimes \boldsymbol{\Phi}^{(2)}\mathbf{U}^{-1} \otimes \boldsymbol{\Phi}^{(1)}\right)vec\left(\mathcal{X}_2^g\right) = vec(\mathcal{Y})$$

$$\vdots$$

$$\left(\boldsymbol{\Phi}^{(N)}\mathbf{U}^{-1} \otimes \dots \otimes \boldsymbol{\Phi}^{(2)} \otimes \boldsymbol{\Phi}^{(1)}\right)vec(\mathcal{X}_N^g) = vec(\mathcal{Y})$$

## 6.3.2 Sparse Weighted Tensor Least Squares Problem

In this section, we used the Weighted Tensor Least Angle Regression (WT-LARS) to solve the multilinear problem given in (6.19). WT-LARS extends Tensor Least Angle Regression (T-LARS) to solve the sparse tensor least-squares problem in (6.19). A multilinear transformation of a tensor $\mathcal{X}_1^g$ could be defined as $\mathcal{Y} = \mathcal{X}_1^g \times_1 \boldsymbol{\Phi}^{(1)}\mathbf{U}^{-1} \times_2 \dots \times_N \boldsymbol{\Phi}^{(N)}$ where $\mathcal{Y} \in \mathbb{R}^{J_1 \times \dots \times J_n \times \dots \times J_N}$ and $\mathcal{X}_1^g \in \mathbb{R}^{I_1 \times \dots \times I_n \times \dots \times I_N}$ are $N^{th}$ order tensors, with the equivalent vector form $\boldsymbol{\Phi}vec\left(\mathcal{X}_1^g\right) = vec(\mathcal{Y})$ as given by (6.19), where $\boldsymbol{\Phi} = \left(\boldsymbol{\Phi}^{(N)} \otimes \dots \otimes \boldsymbol{\Phi}^{(1)}\mathbf{U}^{-1}\right)$. Let $\boldsymbol{W} = \boldsymbol{S}^H\boldsymbol{S}$, be a diagonal weight matrix. We could obtain a weighted linear transformation of $vec\left(\mathcal{X}_1^g\right)$ as

$$\mathbf{S}\boldsymbol{\Phi}vec\left(\mathcal{X}_1^g\right) = \mathbf{S}vec(\mathcal{Y}) \tag{6.20}$$

A sparse representation of the weighted linear system in (6.20) could be obtained by rewriting it as an $L_p$ minimization problem,

$$\widehat{\mathcal{X}_1^g} = \arg\min_{\mathcal{X}_1^g} \left\|\mathbf{S}\boldsymbol{\Phi}vec\left(\mathcal{X}_1^g\right) - \mathbf{S}vec(\mathcal{Y})\right\|_2^2 + \lambda\left\|\mathcal{X}_1^g\right\|_p \tag{6.21}$$

where $\lambda$ is a regularization parameter. Minimization of such objective functions can be performed using various classic iterative optimization algorithms such as steepest-descent and Conjugate-Gradient. However, all these general methods are often found inefficient, requiring too many iterations and too many computations to reach their destination. This is especially the case for high-dimensional problems. In such cases, the OMP and LARS methods are also inefficient for solving large multidimensional sparse least-squares problems as they require multiplication and inversion of huge matrices. Hence, an alternative approach is needed. Recently, a new family of LARS algorithms, known as weighted tensor-least angle regression algorithm (WT-LARS), has been developed, addressing the above optimization problems very effectively. WT-LARS is a generalization of LARS to solve the sparse multilinear least-squares problem in (4.21) for diagonal weighting matrix $S \in \mathbb{R}^{J \times J}$ using tensors and multilinear algebra.

## 6.3.3 Gradient-based Iterative Solution for N-D Poisson Equation

A final step in the gradient-based signal recovery method is to reconstruct the final signal from the estimated gradient data set. $\widehat{\mathcal{X}_n^g}; n \in \{1,2, \dots, N\}$ , each $\mathbb{R}^{I_1 \times I_2 \dots \times I_N}$ tensor denote the estimated non-integrable gradient signals of $\mathcal{X}_n^g$. After obtaining estimates of the gradients $\widehat{\mathcal{X}_n^g}$ of $\mathcal{X}_n^g; n \in \{1,2, \dots, N\}$, an integration technique can be performed to recover an estimate, $\widehat{\mathcal{X}}$, of $\mathcal{X}$. However, the gradient field of the object should be integrable or should have zero curl. Moreover, the inherent noise in the estimation process, the ambiguities in the solution, and ill-posed problems often lead to a non-integrable gradient field [124]. One way of enforcing integrability is to use Simchony, Chellappa, and Shao's (referred to as the SCS) method proposed in [101]. Given a nonintegrable gradient field $\widehat{\mathcal{X}_n^g}; n \in \{1,2, \dots, N\}$, the signal $\mathcal{X}$ such that its gradient field $\mathcal{X}_n^g; n \in \{1,2, \dots, N\}$ satisfies the integrability constraint $\text{curl}(\mathcal{X}_1^g, \mathcal{X}_2^g, \dots, \mathcal{X}_N^g) = 0$ can be obtained by minimizing the following least square function given by [125].

$$J(\mathcal{X}) = \int_{\Omega} \left( (\mathcal{X}_1^g - \widehat{\mathcal{X}_1^g})^2 + \cdots + (\mathcal{X}_N^g - \widehat{\mathcal{X}_N^g})^2 \right) dI \qquad (6.22)$$

where $\Omega$ is a surface. This minimization problem can be solved by using the Euler–Lagrange equation given by

$$\frac{\partial E}{\partial \mathcal{X}} - \sum_{j=1}^{N} \frac{d}{di_j} \left( \frac{\partial E}{\partial \mathcal{X}_j^g} \right) = 0 \qquad (6.23)$$

where $E(\mathcal{X}) = (\mathcal{X}_{1_1}^g - \widehat{\mathcal{X}_{1_1}^g})^2 + (\mathcal{X}_{2_2}^g - \widehat{\mathcal{X}_{2_2}^g})^2 + \cdots + (\mathcal{X}_N^g - \widehat{\mathcal{X}_N^g})^2$. Then (6.23) can be reduced to the following $N$-dimensional Poisson equation

$$\nabla^2 \mathcal{X} = \mathrm{div}\left( \widehat{\mathcal{X}_1^g}, \widehat{\mathcal{X}_2^g}, \ldots, \widehat{\mathcal{X}_N^g} \right) \qquad (6.24)$$

Where $\nabla^2 = \left( \frac{\partial^2}{\partial i_1^2} + \frac{\partial^2}{\partial i_2^2} + \cdots + \frac{\partial^2}{\partial i_N^2} \right)$ is the Laplacian operator and $\nabla^2 \mathcal{X} = (\mathcal{X}_1^g)_{i_1} + (\mathcal{X}_2^g)_{i_2} + \cdots + (\mathcal{X}_N^g)_{i_N}$, i.e., the integrable field $\mathcal{X}_n^g$ ; $n \in \{1,2, \ldots, N\}$ is found by differentiating the estimated signal $\mathcal{X}$ . In other words, this method enforces integrability by finding a zero-curl gradient field that has the same divergence as the estimated nonintegrable gradient field. The divergence of the gradients is given by

$$\mathrm{div}(\mathcal{X}_1^g, \mathcal{X}_2^g, \ldots, \mathcal{X}_N^g) = \frac{\partial}{\partial i_1}(\mathcal{X}_1^g) + \frac{\partial}{\partial i_2}(\mathcal{X}_2^g) + \cdots + \frac{\partial}{\partial i_N}(\mathcal{X}_N^g) \qquad (6.25)$$

$$= (\mathcal{X}_1^g)_{i_1} + (\mathcal{X}_2^g)_{i_2} + \cdots + (\mathcal{X}_N^g)_{i_N}$$

Let $\mathcal{U} \in \mathbb{R}^{I_1 \times I_2 \cdots \times I_N}$ be tensor corresponding to $\mathrm{div}\left( \widehat{\mathcal{X}_1^g}, \widehat{\mathcal{X}_2^g}, \ldots, \widehat{\mathcal{X}_N^g} \right)$ then the N-dimensional Poisson equation can be written as a vectorized tensor form as

$$\mathbf{Lx} = \mathbf{u} \tag{6.26}$$

where $= vec(\mathcal{U}) \in \mathbb{R}^{I_1 I_2 \dots I_N \times 1}$ , $\mathbf{x} = vec(\mathcal{X}) \in \mathbb{R}^{I_1 I_2 \dots I_N \times 1}$ is the sparse Laplacian matrix corresponding to the Laplacian operator $\nabla^2$ and can be written as a sum of Kronecker product of matrices $\boldsymbol{D}_{i_n}, \boldsymbol{I}_{i_n} \in \mathcal{R}^{I_n \times I_n}; n \in \{1,2,\dots,N\}$ and it's given by

$$\mathbf{L} = \boldsymbol{I}_{i_N} \otimes \cdots \otimes \boldsymbol{I}_{i_2} \otimes \boldsymbol{D}_{i_1} + \cdots + \boldsymbol{D}_{i_N} \otimes \cdots \otimes \boldsymbol{I}_{i_2} \otimes \boldsymbol{I}_{i_1} \tag{6.27}$$

where $I$ is the identity matrix and the matrix $\boldsymbol{D}_{i_n}; n \in \{1,2,\dots,N\}$ is a one-dimensional Laplacian operator and is given by

$$\boldsymbol{D}_{i_n} = \begin{bmatrix} 2 & -1 & & \\ -1 & -2 & -1 & \\ & . & . & . \\ & & -1 & 2 \end{bmatrix}_{I_n \times I_n} \tag{6.28}$$

substituting the expression for the sparse Laplacian matrix into the Poisson equation given by (6.26) can be written as

$$( \boldsymbol{I}_{i_N} \otimes \cdots \otimes \boldsymbol{I}_{i_2} \otimes \boldsymbol{D}_{i_1} + \cdots + \boldsymbol{D}_{i_N} \otimes \cdots \otimes \boldsymbol{I}_{i_2} \otimes \boldsymbol{I}_{i_1})\mathbf{x} = \mathbf{u} \tag{6.29}$$

Further, (4.29) can also be written as a multilinear transformation of tensor $\mathcal{X}$ as following

$$\sum_{n=1}^{N} \mathcal{X} \times_n \boldsymbol{D}_{i_n} = \mathcal{U} \tag{6.30}$$

where all *mode-n* fibers of the tensor X are multiplied by the matrix $\boldsymbol{D}_{i_n}$ . The above equation is known as the Sylvester tensor equation and is widely used in different applications such as system identification [126, 127]. Iterative methods are often used to solve the problem [128]. The Sylvester tensor equation given by 6.30 has a unique solution if and only if $\sum_{n=1}^{N} \lambda_{i_n}(\boldsymbol{D}_{i_n}) \neq 0$ for any $i_n; n \in \{1,2,\dots,N\}$ [126]. Where $\lambda_{i_n}$ denotes the eigenvalue of $\boldsymbol{D}_{i_n}$. To derive the gradient-

based iterative algorithm for the Sylvester tensor problem, we need to define the following residual tensors: $\mathcal{E}_j; j \in \{1,2, \ldots, N\}$.

$$\mathcal{E}_j := \mathcal{U} - \sum_{n=1,n\neq j}^{N} \mathcal{X} \times_n \boldsymbol{D}_{i_n} \tag{6.31}$$

(6.30) can be decomposed into $N$ subsystems:

$$\mathcal{X} \times_n \boldsymbol{D}_{i_n} = \mathcal{E}_n \tag{6.32}$$

The solution for the tensor X can be obtained by minimizing the following least-squares problem:

$$J_n(\mathcal{X}) = \frac{1}{2} \left\| \mathcal{X} \times_n \boldsymbol{D}_{i_n} - \mathcal{E}_n \right\|^2 \tag{6.33}$$

derivatives of $J_n(\mathcal{X}); n \in \{1,2, \ldots, N\}$ with respect to $\mathcal{X}$ are derived in [38] and is given by

$$\frac{\partial J_n(\mathcal{X})}{\partial x} = \left( \mathcal{X} \times_n \boldsymbol{D}_{i_n} - \mathcal{E}_n \right) \times_n \boldsymbol{D}_{i_n}^{\ T} \tag{6.34}$$

Minimizing $J_n(\mathcal{X})$ and equating its partial derivatives to zero leads to the following recursive equations:

$$\mathcal{X}_n^k = \mathcal{X}^{k-1} + \mu \mathcal{R}_n^{k-1} \times_n \boldsymbol{D}_{i_n}^{\ T} \tag{6.35}$$

where $0 < \mu < 2/\left( \sum_{n=1}^{N} \|\boldsymbol{D}_{i_n}\|_2^2 \right)$ is iterative step length, and the residual $\mathcal{R}_i^k$ is given by

$$\mathcal{R}_i^k = \mathcal{U} - \sum_{n=1}^{N} \mathcal{X}_i^k \times_n \boldsymbol{D}_{i_n} \tag{6.36}$$

Finally, the tensor $\mathcal{X}$ is obtained by taking the average of $\mathcal{X}_n^k; n \in \{1,2, \ldots, N\}$, i.e., $\mathcal{X} = \frac{1}{N} \sum_{n=1}^{N} \mathcal{X}_n^k$.

**Algorithm 1: Kronecker based Iterative Solution for N-D Poisson Equation**

**Input:** one-dimensional Laplacian operator $\boldsymbol{D}_{i_n}$; $n \in \{1,2,\dots,N\}$, $\mathcal{U} \in \mathbb{R}^{I_1 \times I_2 \dots \times I_N}$ ; iterative step length μ; Stopping criterion: residual tolerance: ε or number of non-zero coefficients: K

**Output:** $\mathcal{X}$

**Initialization:** $\mathcal{X}^0$, iteration $t = 1$

1. *Compute residual*

$$\mathcal{R}_i^t = \mathcal{U} - \sum_{n=1}^{N} \mathcal{X}_i^t \times_n \boldsymbol{D}_{i_n}$$

2. *Update components of the solution $\mathcal{X}_n^t$; $n \in \{1,2,\dots,N\}$*

$$\mathcal{X}_n^t = \mathcal{X}^{t-1} + \mu \mathcal{R}_n^{t-1} \times_n \boldsymbol{D}_{i_n}{}^T$$

3. *Update the final solution*

$$\mathcal{X}^t = \frac{1}{N} \sum_{n=1}^{N} \mathcal{X}_n^t$$

4. *Stopping Rule: if $\|\mathcal{X}^t - \mathcal{X}^{t-1}\|_2^2$ is smaller than some predetermined threshold ε, stop.*
5. *Otherwise, apply another iteration.*

## 6.4   Experimental Results

In this section, two experimental results are conducted to verify the performance of our gradient-based multidimensional signal recovery method to obtain a sparse representation of 3D images. The gradient images are obtained by solving the $L_1$ constrained sparse tensor least-squares problem using WT-LARS after applying zero weights to the missing data. For our computational experiments shown in Figure 6.1 and Figure 6.2, we obtained 3D brain images, and 3D liver images, from publicly available datasets. Our used 3D MRI images were obtained from the OASIS-3:

Longitudinal Neuroimaging, Clinical, and Cognitive Dataset for Normal Aging and Alzheimer's Disease [129]. We compare the performance of our gradient-based sparse recovery algorithm to obtain K-sparse representations of the images. Our fixed *mode-n* overcomplete dictionaries were a union of a Discrete Cosine Transform (DCT) dictionary and a Symlet wavelet packet with four vanishing moments dictionaries. In this case of using fixed *mode-n* dictionaries, we obtained the required 3D sparse representations by solving the 3-D $L_1$ minimization problem.

All our experimental results were obtained using MATLAB on an MS-Windows machine: 2 Intel Xeon CPUs E5-2637 v4, 3.5GHz, 32GB RAM, and NVIDIA Tesla P100 GPU with 12GB memory. In the first example, we obtain the sparest representation of a 3D MRI brain image, $\mathcal{Y}$, $175 \times 150 \times 10$ tensor and size of the representation coefficient of the tensor $\mathcal{Y}$ is $351 \times 302 \times 26$ and has N = 2, 756, 052 voxels in total. The coherence parameter for the Kronecker dictionary $\boldsymbol{\Phi} = \left(\boldsymbol{\Phi}^{(3)} \otimes \boldsymbol{\Phi}^{(2)} \otimes \boldsymbol{\Phi}^{(1)}\right)$ is $\mu(\boldsymbol{\Phi}) = 0.780$. In this experiment, the algorithm was stopped when the number of non-zero coefficients $K$ reached 25,000, which is 9.5% of the number of elements in $\mathcal{Y}$. A minimum of $M = 153,353$ samples is required for exact recovery of the 3D MRI image using WT-LARS, with $K = 25,000$ nonzero coefficients. Using our gradient-based signal recovery method, the coherence parameter is reduced to $\mu_x(\boldsymbol{\Phi}) = 0.674$ for the column vectors of $\boldsymbol{\Phi} = \left(\boldsymbol{\Phi}^{(3)} \otimes \boldsymbol{\Phi}^{(2)} \otimes \boldsymbol{\Phi}^{(1)}\mathbf{U}^{-1}\right)$, $\mu_y(\boldsymbol{\Phi}) = 0.605$ for the column vectors of $\boldsymbol{\Phi} = \left(\boldsymbol{\Phi}^{(3)} \otimes \boldsymbol{\Phi}^{(2)}\mathbf{U}^{-1} \otimes \boldsymbol{\Phi}^{(1)}\right)$ and $\mu_z(\boldsymbol{\Phi}) = 0.615$ for the column vectors of $\boldsymbol{\Phi} = \left(\boldsymbol{\Phi}^{(3)}\mathbf{U}^{-1} \otimes \boldsymbol{\Phi}^{(2)} \otimes \boldsymbol{\Phi}^{(1)}\right)$. The maximum coherence $\mu_x(\boldsymbol{\Phi}) = 0.674$ corresponds to M = 112, 478 number of samples, which is 42.8% of the number of elements in $\mathcal{Y}$.

Experiment 1: Figure 6.1 shows obtained experimental results for representing our 3D MRI brain image, $\mathcal{Y}$, $175 \times 150 \times 10$ tensor using three fixed mode-n overcomplete dictionaries, $\boldsymbol{\Phi}^{(1)} \in \mathbb{R}^{175 \times 351}$, $\boldsymbol{\Phi}^{(2)} \in \mathbb{R}^{150 \times 302}$ and $\boldsymbol{\Phi}^{(3)} \in \mathbb{R}^{10 \times 26}$ by solving the $L_1$ minimization problem, using WT-LARS. In this example, we assume that only a small set of coefficients is available. We can observe that the MRI image can be successfully reconstructed by using 50%, 75%, and 100%

of the total number of samples. Therefore, using our gradient-based multidimensional signal recovery algorithm, we obtained the exact sparse signal representation of the 3D image with incomplete samples.
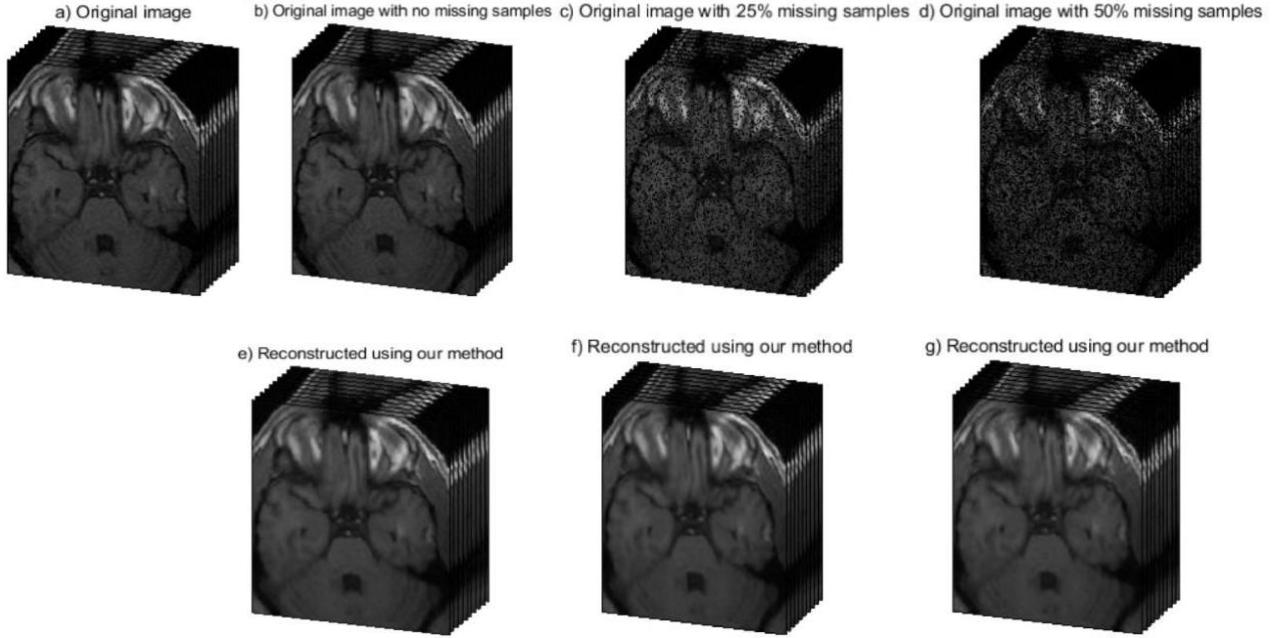


Figure 6.1. 3D-MRI brain image and its reconstruction using 9.5% non-zero coefficients (K=25,000) obtained by WT-LARS using fixed *mode-n* overcomplete dictionaries. (a) Original 3D-MRI brain image, original image with (b) no missing samples, (c) 25% missing samples, (d) 50% missing samples. (e) image reconstructed using 100% number of samples, (f) image reconstructed using 75% number of samples, (g) image reconstructed using 50% number of samples

Experiment 2: Figure 6.2 shows obtained experimental results for representing our 3D MRI liver image $\mathcal{Y}$, $195 \times 166 \times 14$ voxels using three fixed *mode-n* overcomplete dictionaries, $\mathbf{\Phi}^{(1)} \in \mathbb{R}^{195 \times 395}$, $\mathbf{\Phi}^{(2)} \in \mathbb{R}^{166 \times 334}$ and $\mathbf{\Phi}^{(3)} \in \mathbb{R}^{14 \times 30}$, by solving the $L_1$ minimization problem, using WT-LARS. In this experiment, the algorithm was stopped when the number of non-zero coefficients K reached 35,000, which is 7.7% of the number of elements in $\mathcal{Y}$.
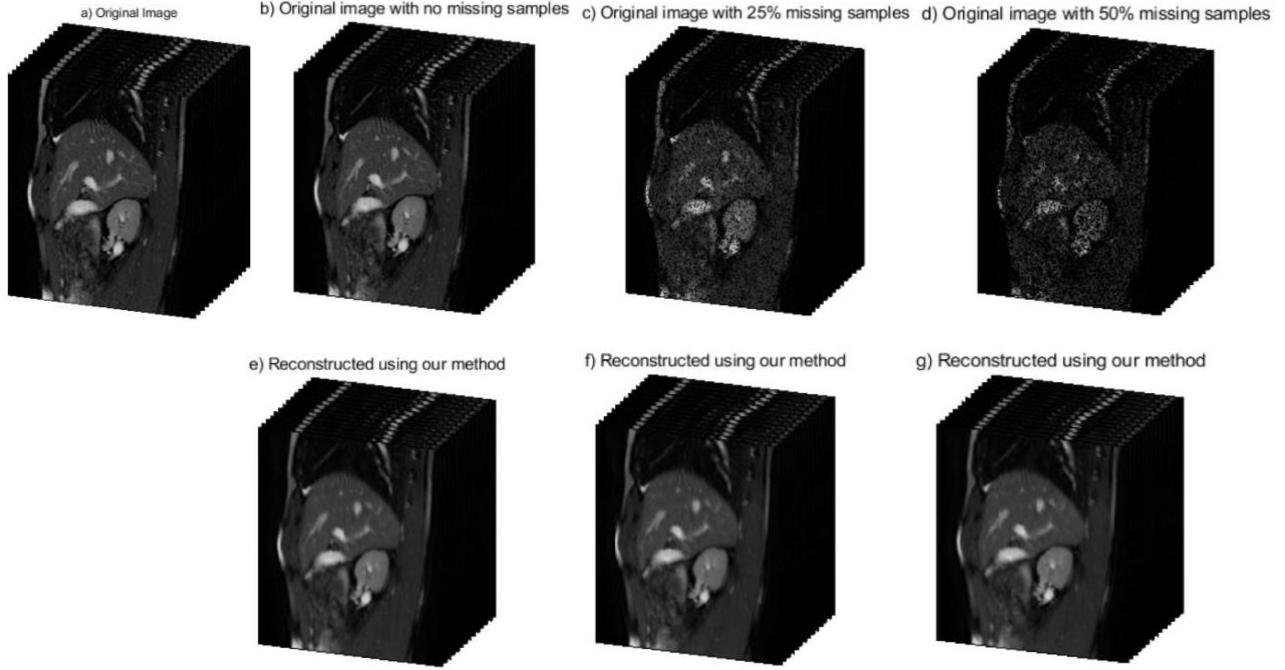
Figure 6.2. 3D-MRI liver image and its reconstruction using 7.7% non-zero coefficients (K=35,000) obtained by WT-LARS using fixed mode-n overcomplete dictionaries. (a) Original 3D-MRI liver image, original image with (b) no missing samples, (c) 25% missing samples, (d) 50% missing samples. (e) image reconstructed using 100% number of samples, (f) image reconstructed using 75% number of samples, (g) image reconstructed using 50% number of samples

**Table 6.1**: Summary of experimental results for our 3D MRI images

| Experiment | Image Size | K | Coherence, $\mu(\boldsymbol{\Phi})$ | Minimum number of Measurements, M | Norm of Residual, $\|\mathcal{R}\|_2$ |
|---|---|---|---|---|---|
| 1 | $175 \times 150 \times 10$ | 25,000 (9.5%) | 0.78 | 153,352 (58.4%) | 0.0724 (7.24%) |
| 1 (Gradient-based method) | $175 \times 150 \times 10$ | 25,000 | 0.674 | 112,478 (42.8%) (26.65% less than 1) | 0.0859 (8.59%) |
| 2 | $195 \times 166 \times 14$ | 35,000 (7.7%) | 0.8481 | 250,841 (55%) | 0.1289 (12.89%) |
| 2 (Gradient-based method) | $195 \times 166 \times 14$ | 35,000 | 0.7331 | 186,120 (41%) (25.81% less than 2) | 0.1302 (13.02%) |

In the second example, we obtain the sparest representation of a 3D MRI liver image, $\mathcal{Y}$, $195 \times 166 \times 14$ tensor and size of the representation coefficient of the tensor $\mathcal{Y}$ is $395 \times 334 \times 30$ and has N = 3, 957, 900 voxels in total. The coherence parameter for the Kronecker dictionary $\boldsymbol{\Phi} = \left(\boldsymbol{\Phi}^{(3)} \otimes \boldsymbol{\Phi}^{(2)} \otimes \boldsymbol{\Phi}^{(1)}\right)$ is $\mu(\boldsymbol{\Phi}) = 0.8481$. In this experiment, the algorithm was stopped when the number of non-zero coefficients K reached 35,000, which is 7.7% of the number of elements in $\mathcal{Y}$. A minimum of M = 250, 841 samples are required for exact recovery of the 3D MRI liver image using WT-LARS, with $K = 35,000$ nonzero coefficients. Using our gradient-based signal recovery method, the coherence is reduced to $\mu_x(\boldsymbol{\Phi}) = 0.7262$ for the column vectors of $= \left(\boldsymbol{\Phi}^{(3)} \otimes \boldsymbol{\Phi}^{(2)} \otimes \boldsymbol{\Phi}^{(1)}\mathbf{U}^{-1}\right)$, $\mu_y(\boldsymbol{\Phi}) = 0.7331$ for the column vectors of $\boldsymbol{\Phi} = \left(\boldsymbol{\Phi}^{(3)} \otimes \boldsymbol{\Phi}^{(2)}\mathbf{U}^{-1} \otimes \boldsymbol{\Phi}^{(1)}\right)$ and $\mu_z(\boldsymbol{\Phi}) = 0.7308$ for the column vectors of $\boldsymbol{\Phi} = \left(\boldsymbol{\Phi}^{(3)}\mathbf{U}^{-1} \otimes \boldsymbol{\Phi}^{(2)} \otimes \boldsymbol{\Phi}^{(1)}\right)$. The maximum coherence $\mu_y(\boldsymbol{\Phi}) = 0.7331$ corresponds to M = 186, 120 number of samples, which is 41% of the number of elements in $\mathcal{Y}$.

## 6.5   Chapter Summary

In this chapter, the problem of sparse representation of a multidimensional signal is investigated. A gradient-based approach is proposed in which the aim is to reconstruct a multidimensional signal when an incomplete sampled measurement is collected in an arbitrary transformation domain. This entails using the assumption that the signal is assumed to be sparsely represented by gradients. To improve the performance of sparse representation, we exploit the fact that many signals are known to have sparse gradients. In this case, gradient-based signal recovery would succeed by recovering these gradients individually before reconstructing the original signal from these recovered gradients. Since the signal is retrieved from incomplete data samples, where some of its elements are zero, the weighted tensor least squares problem loses the Kronecker structure, which could not be efficiently solved using Kronecker-OMP or T-LARS. In this work, we used an efficient method called weighted tensor least angles regression (WT-LARS) to estimate the gradients from

incomplete samples, where we used a non-separable diagonal weight matrix. The weight matrix is a diagonal matrix with weights as diagonal elements. We also demonstrated that the assumption that the signal is assumed to have sparse gradients had improved the sparsity. The result of our method on 3D MRI images is promising. It also confirms that mutual coherence is necessary for efficient sparse representation, which is introduced in terms of the number of measurements taken.

# Chapter 7

# Power Transformer Paper Insulation Ageing Estimation Using Swept-Source Optical Coherence Tomography

The current chapter presents an evaluation of changes in the subsurface structural texture due to thermal stress. Using a statistical-based image texture analysis method, a quantitative analysis was developed by converting each OCT image of thermally aged Kraft paper samples to the spatial grey level dependence matrix (SGLDM). The results and analysis of the computed statistical texture features are presented along with the operational age estimation model. The statistical features show how the paper texture with different deterioration levels may change in relation to the ageing time.

## 7.1 Preparation of Thermally Aged Kraft Paper Samples

Samples of oil-impregnated Kraft paper have been aged at different levels by accelerated thermal ageing. The accelerated thermal ageing test is a common method used to monitor the performance and condition of the insulation materials [36], and various experiment arrangements have been reported [130]. In [35, 131], a similar accelerated thermal ageing experiment was conducted for assessing the retained tensile strength of thermally aged oil-impregnated Kraft paper samples. In this work, 400 brand-new samples of transformer cellulose paper were selected, and the ageing time of the insulating paper was used to differentiate the samples with different ageing conditions. The Kraft paper was cut into 2.5 cm $\times$ 3 cm rectangular samples, and each sample was then inserted in a cylindrical glass vial, as shown in Figure 7.1.

Before the accelerated ageing process, the sample vials were placed in a vacuum oven at 105°C for 24 hours to remove moisture influences on the ageing. After drying, the sample vials were taken out from the oven and immediately sealed. Approximately 10 ml of insulating oil was added to each vial to impregnate the paper samples, as shown in Figure 7.2. Following impregnation, the sample vials were then returned to the oven at a temperature of 140°C for accelerated thermal ageing. One Kraft paper sample was then removed from the oven every 1 hour. Thus, the minimum and maximum ageing times of the thermally deteriorated samples are 0 and 399 hours, respectively. Each vial is immediately sealed upon removal from the oven. A temperature of 140°C was selected for the accelerated thermal ageing test because it is sufficiently well above operating temperatures that the insulation would be exposed to during service [30], and the same temperature was selected for the ageing experiment performed in [1].

Figure 7.1. Preparation of sample vials containing Kraft papers for removal of pre-existing moisture.

Figure 7.3 shows sample vials containing Kraft paper with different ageing levels. As seen in this figure, the color of the oil has also changed due to the heat.

## 7.1.1   Swept Source OCT Images of Thermally Aged Paper Samples

After thermal ageing, subsurface structural images of the insulating Kraft paper samples were obtained using an SS-OCT system with a wavelength-swept laser source (Santec HSL-20- 100-B) with a scanning rate of 100 kHz. Its center wavelength is 1, 310 nm, wavelength range from 1, 270 - 1, 360 nm, and average output power of 22.2 mW.

Figure 7.2. Sample vials containing Kraft paper and 10 ml of insulating oil.

A comparison of SS-OCT sample images after a different ageing time of thermal stressing at 140°C is shown in Figure 7.4. A typical change to the oil-impregnated paper samples morphology due to the thermal deterioration is clear in the SS-OCT sample images.

Five OCT images were taken for each insulating paper sample, and in total, up to 500 OCT images were acquired from the paper samples. To reduce the effect of illumination, the positions of the reference and sample arms of the SS-OCT system were held constant during all measurements. Better contrast and uniform distribution of intensities can be achieved by applying an image processing technique called image normalization on each OCT image. After the normalization step, the pixel intensity values range from 0 to 255. This is performed by a Min-Max normalization method that linearly transforms the original image from its range to another range without changing the relationships of the original data values.
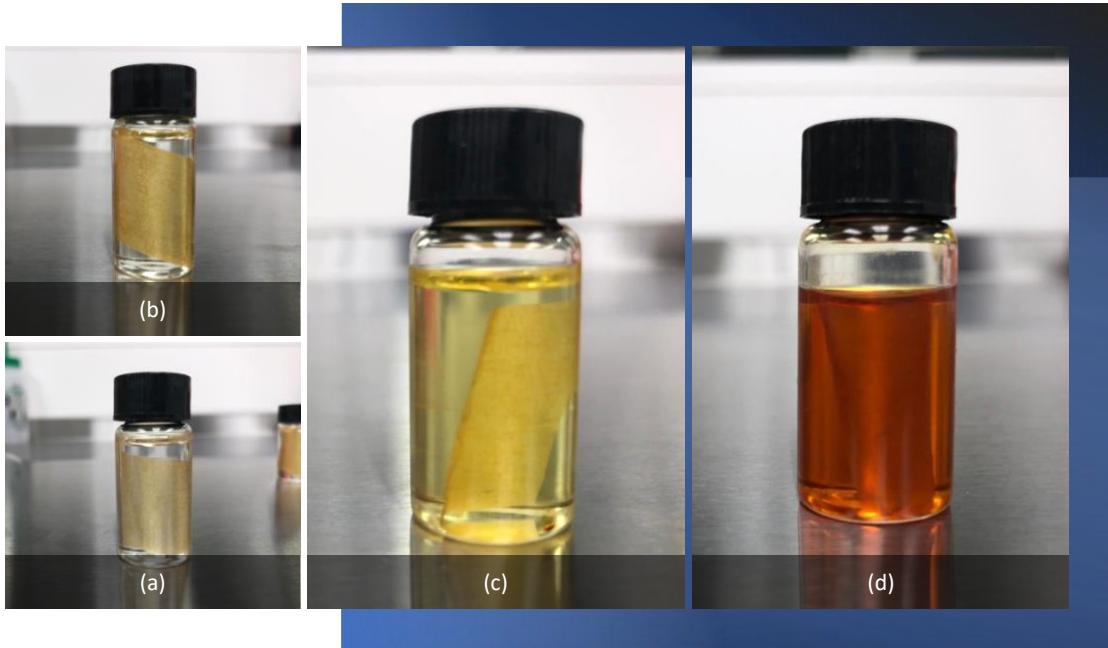
Figure 7.3. Sample vials containing Kraft paper and insulating oil after accelerated ageing tests. Samples aged (a) 0-hour, (b) 152-hours, (c) 252-hours, (d) 396-hours.

the Min-Max normalization formula is given by

$$X^{\text{norm}} = X_{\min}^{\text{norm}} + \frac{(X - X_{\min})}{(X_{\max} - X_{\min})} (X_{\max}^{\text{norm}} - X_{\min}^{\text{norm}}) \tag{7.1}$$

where $X$ represents the original unnormalized pixel, $X^{\text{norm}}$ represents the normalized pixel, and $X_{\max}$ and $X_{\min}$ are the maximum and minimum pixel values within the original image, respectively. The values $X_{\max}^{\text{norm}}$ and $X_{\min}^{\text{norm}}$ represents the maximum and minimum pixel intensities of the normalized image, which are 0 and 255, respectively. As can be seen from Figure 7.4, the subsurface structural

OCT image of the new cellulose Kraft paper has many texture variations. These correspond to a network of fibers that are orderly arranged.
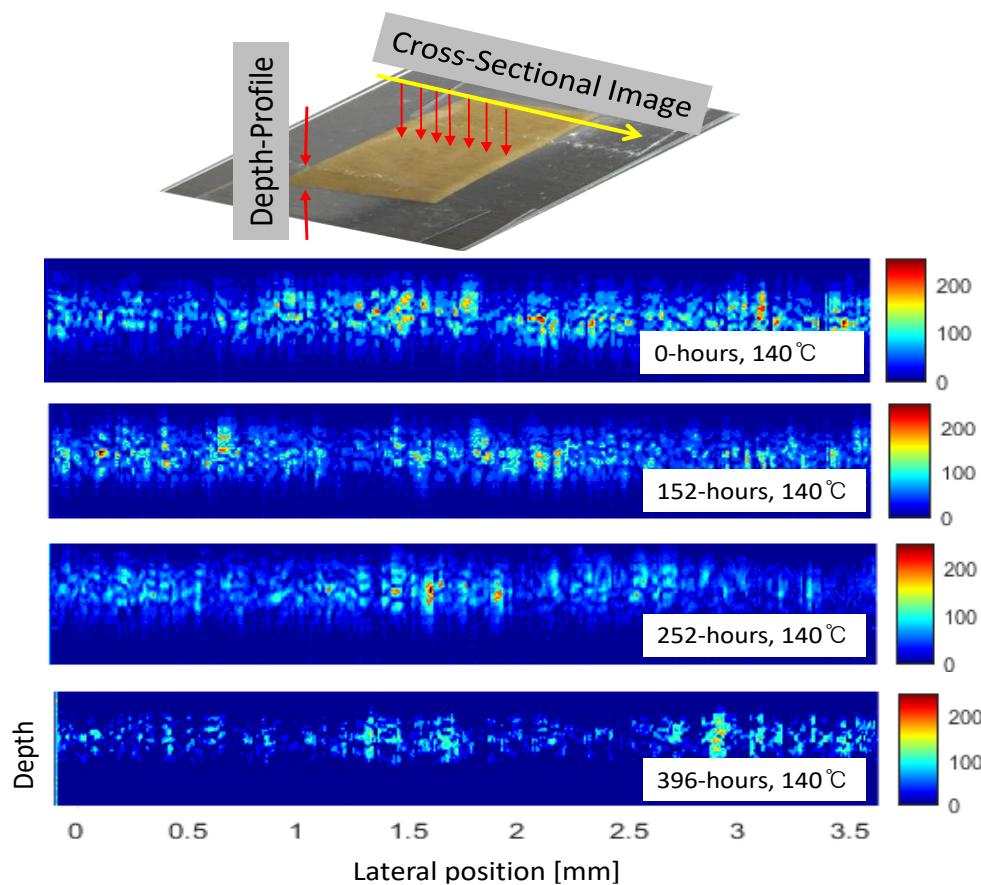


Figure 7.4. Experimental results for SS-OCT imaging oil-impregnated Kraft paper samples. The top image shows a Kraft paper sample placed in a microscope slide, and multiple A-scans (depth profiles), indicated by red arrows, allow for cross-sectional imaging of the sample. The second image shows a new Kraft paper, while the remaining OCT images show Kraft paper samples after 152-hours, 252-hours, and 396-hours of thermal stressing at 140°C.

As the paper becomes more thermally deteriorated, some gaps and cracks between the fibers

are created [2, 132, 37]. Consequently, the fiber structure of the paper samples changes, and this makes it difficult to perceive individual fibers of the oil-impregnated paper sample visually. After 396 hours of thermal ageing, the breakdown of the fibers is significant, and the density of the sample in the cross-sectional OCT image becomes sparse. Once the OCT measurements are completed, each OCT image is converted into a spatial grayscale level dependence matrix (SGLDM) [133], from which the Haralick texture features [134] are calculated.

## 7.2  Statistical Image Texture Analysis

Texture analysis extracts metrics/features from an image that quantifies its smoothness or coarseness and is used in different applications such as remote sensing and biomedical imaging [47]. These metrics typically relate the frequency of occurrence for pixel grey level intensities to their spatial arrangement within an image. SGLDM is one of the best-known texture analysis methods and contains the second-order statistical information of the spatial relationship of pixels of an image. SGLDM is a square matrix with elements corresponding to the number of instances in which a pixel with a certain grey level intensity appears next to another pixel with a specific gray level intensity. The number of rows and columns of the SGLDM matrix is equivalent to the number of gray levels in the sample image. An example for the computation of an SGLDM having three grey levels is provided in Figure 7.5. In this example, the original image is represented by a $4 \times 4$ matrix shown in Figure 7.5 (a), which has colored cells with varying numerical values from 1 to 3. Figure 7.5 (b) shows the cell entries of the SGLDM matrix, which is constructed by considering the relation of each pixel with its neighbor to the right. The SGLDM counts all combinations of gray-level pairs in the image. For example, there are two instances when a grey-level 3 is neighbored by the grey-level 2, and there is one instance of a reference grey-level 3 is neighbored with a grey-level 1. Moreover, if the pixel pairs in the image are highly correlated, the resulting SGLDM matrices would be diagonal, and this implies that the image has no texture.
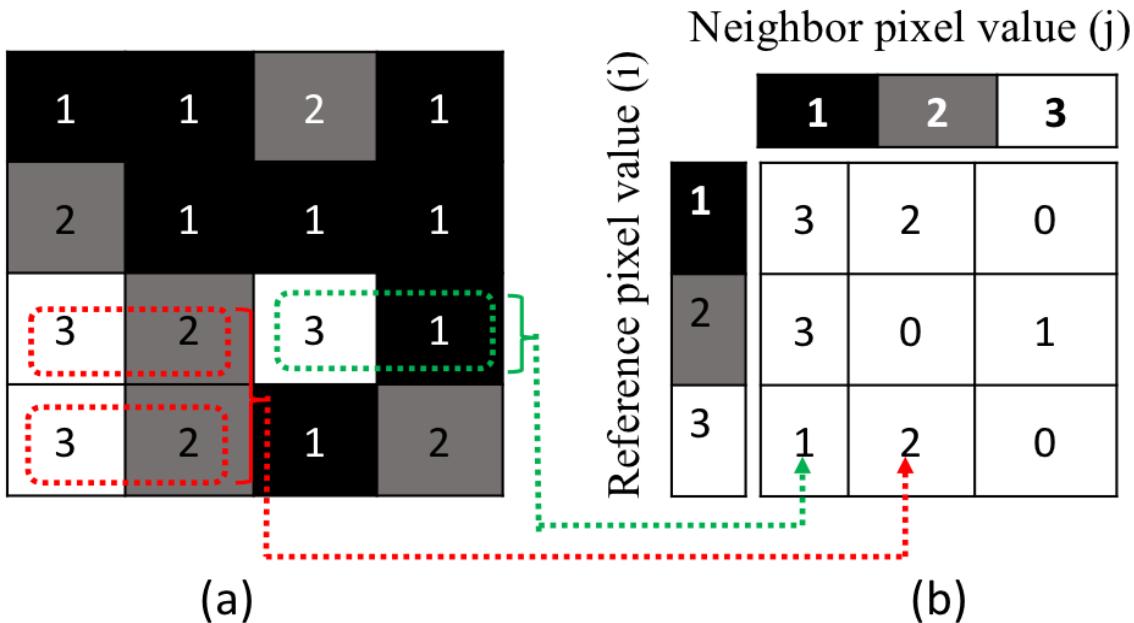
Figure 7.5. Example computation for SGLDM matrix on the imaginary 4x4 sample image. (a) Image with numeric gray levels (b) Right neighbor SGLDM.

The off-diagonal values in the SGLDM matrices will increase as the image texture increases (i.e., as the local pixel intensity variations increase). Finally, the SGLDM matrix is normalized by the sum of all grey-level intensities present in the original image. The normalized SGLDM matrix represents the estimated probability of each combination occurring in the image. For the OCT images of the aged paper samples, the statistical variation in gray levels is directly related to subsurface structural texture. Different properties of the pixel distribution can be obtained by applying mathematical operations on the SGLDM matrices. Features describe texture properties and contain essential information about the stochastic properties of the spatial distribution of gray-level in an image that represents specific image properties such as coarseness, contrast, and homogeneity. Feature extraction is a technique for obtaining higher-level information of an image and consists of two steps. SGLDM matrix is calculated in the first step, while the Haralick texture

features based on the SGLDM are computed in the second step. In this work, the OCT images of the thermally aged paper samples, captured with 256 greyscale levels, are converted to $256 \times 256$ SGLDM matrices. Eleven statistical textural features of SGLDM in two directions within an image plane are calculated according to Haralick equations. One direction for horizontal neighboring pixels ($0°$ and $180°$) and the other for neighboring vertical pixels ($90°$ and $270°$). As a result, 22 textural features were generated for each OCT image of the thermally aged paper sample and saved in the feature vector.

## 7.2.1 Haralick Statistical Texture Features

The formulas for the Haralick texture features are shown in (7.2) – (7.15) and have been adopted from [133, 134]. Generally, the cell entries of the SGLDM matrix are represented by $p_{(d,\theta)}(i,j)$. The co-occurrence matrix $p_{(d,\theta)}(i,j)$ is the probability of a pixel with the $i^{th}$ gray level from a fixed location distance d and reached to the $j^{th}$ gray-level. Where θ represents the angle relative to a reference pixel used in constructing the SGLDM. The $i^{th}$ row and $j^{th}$ column of the SGLDM matrix are represented by $(i,j)$. In this thesis, the SGLDM matrix has been defined using a distance $d = 1$ pixels from the reference pixel and at angle $0°$ and $180°$ for one complete feature set. Another set has been defined using the neighboring vertical pixels at $90°$ and $270°$ from the reference pixel. In total twenty-two, features are computed for each OCT image.

Angular Second Moment (ASM) or energy: ASM is used to measure the uniformity in the pixel grey-scale intensities in the image of texture. It is proportional to the global uniformity of gray-tone transitions spread within an image. An image having a uniform grey-level distribution results in large ASM feature quantity and is given by

$$Angular\ Second\ Moment:\ F_1 = \sum_{i=1}^{N} \sum_{j=1}^{N} p^2_{(d,\theta)}(i,j) \tag{7.2}$$

Contrast: Contrast is a measure of intensity or gray-level variations between the reference pixel and its neighbor. For an image containing a large amount of variation, the co-occurrence matrix $p_{(d,\theta)}(i,j)$ will be concentrated away from the main diagonal, and hence, the contrast feature quantity will be high. The feature described by 7.3 is a measure of contrast in an image.

$$Contrast: \quad F_2 = \sum_{\substack{n=1, \\ n=|i-j|}}^{N} n^2 \left\{ \sum_{i=1}^{N} \sum_{j=1}^{N} p_{(d,\theta)}(i,j) \right\}, \tag{7.3}$$

Variance (Sum of Squares): Variance measures the dispersion of the values around the mean of combinations of reference and neighbor pixels. The parameter $\mu$ represents the global mean of the SGLDM histogram matrix. The variance feature value is always high when an image contains a large variety of pixel intensities.

$$Variance: \quad F_3 = \sum_{i=1}^{N} \sum_{j=1}^{N} (i-\mu)^2 p_{(d,\theta)}(i,j) \tag{7.4}$$

Inverse Difference Moment (IDM): Inverse difference moment (7.5) measures the local homogeneity in an image. A significant value of IDM means that an image contains pixels neighbored by other pixels with the same or similar intensity. Therefore, images with concentrated regions of dark or bright pixels immediately neighboring each other will yield higher IDM.

$$Inverse\ Diffrence\ Moment: \quad F_4 = \sum_{i=1}^{N} \sum_{j=1}^{N} \frac{1}{1+(i-j)^2} p_{(d,\theta)}(i,j) \tag{7.5}$$

Sum Vector: A sum vector given by (7.6) is computed from the SGLDM histogram matrix. The sum vector is calculated from the addition of the histogram matrix cell entries where the cell indices satisfy the condition that $k = i + j$ in the range from 2 to 2N. The sum vector is used to

calculate features F5, F6, and F7 given by (7.6) to (7.8).

$$p_{(x+y)}(k) = \sum_{i=1}^{N}\sum_{j=1}^{N} p_{(d,\theta)}(i,j), \quad where \ \ k = i + j \tag{7.6}$$

Sum Average: The sum average feature in (7.7) calculates the average value of the sum vector in (7.6)

$$Sum\ Average: \qquad F_5 = \sum_{i=2}^{2N} i \cdot p_{x+y}(i) \tag{7.7}$$

Sum Variance: Sum variance measures the dispersion of the gray level sum distribution of the image. It has a high value when the values of the SGLDM matrix are equally concentrated in the lowest and highest cells.

$$Sum\ Variance: \qquad F_6 = \sum_{i=2}^{2N} (i - F_6)^2 \cdot p_{x+y}(i) \tag{7.8}$$

Sum Entropy: expressed in (7.9), sum entropy measures the disorder related to the gray level sum distribution of an image.

$$Sum\ Entropy: \qquad F_7 = -\sum_{i=2}^{2N} p_{x+y}(i) \log(p_{x+y}(i)) \tag{7.9}$$

Entropy: (7.10) calculates the entropy of an image, which is a measure of the randomness or the degree of disorder of intensity distribution present in the SGLDM. When an image is texturally uniform, many SGLDM matrix elements will have huge values, implying that entropy is minimal. It is computed as

$$Entropy: \quad F_8 = -\sum_{i=1}^{N}\sum_{j=1}^{N} p_{(d,\theta)}(i,j)\log(p_{(d,\theta)}(i,j)) \tag{7.10}$$

Difference Vector: (7.11) computes a difference vector from the entries of the SGLDM matrix. The difference vector relates to the number of occurrences SGLDM entries differ by a value $k = |i - j|$ ranging from 0 to $N$. The difference vector is used to compute features F9 and F10 given by (7.12) and (7.14).

$$p_{x-y}(k) = \sum_{i=1}^{N}\sum_{j=1}^{N} p_{x-y}(i)\log\left[p_{x-y}(i,j)\right] \quad where \quad k = |i - j| \tag{7.11}$$

Difference Variance: (7.12) computes the variance of entries in the difference vector in (7.11)

$$Difference\ Variance: \quad F_9 = \sum_{i=1}^{N}(i - F_9')^2 . p_{x-y}(i) \tag{7.12}$$

where

$$F_9' = \sum_{i=1}^{N} i . p_{x-y}(i) \tag{7.13}$$

Difference Entropy: Given by (7.14), which computes the disorder related to the gray level difference distribution of the image.

$$Difference\ Entropy: \quad F_{10} = -\sum_{i=1}^{N} p_{x-y}(i)\log(p_{x-y}(i)) \tag{7.14}$$

Information Measures of Correlation: (7.15) calculates the information measures of correlation feature, which is a statistical metric developed from the sums of row $i$ and column $j$ entires of the SGLDM.

$$F_{11} = (1 - \exp\left[-2(HXY2 - HXY)\right]^{\frac{1}{2}}) \tag{7.15}$$

where
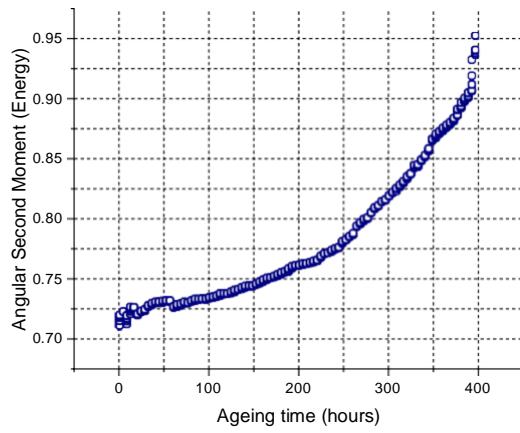
$$HXY2 = -\sum_{i=1}^{N}\sum_{j=1}^{N} p_x(i)p_y(j)\log(p_x(i)p_y(j)) \qquad (7.16)$$

$$HXY = -\sum_{i=1}^{N}\sum_{j=1}^{N} p_{(d,\theta)}(i,j)\log(p_{(d,\theta)}(i,j))$$

$$p_x(i) = \sum_{j=1}^{N} p_{(d,\theta)}(i,j)$$

## 7.2.2 Texture Analysis of Thermally Deteriorated Paper Samples
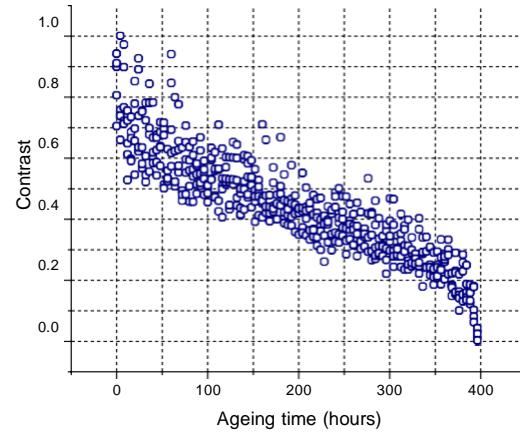
Each OCT sample image of thermally aged paper is converted into a feature vector containing 22 Haralick texture features based on the SGLDM. Figure 7.6 shows the variation of Haralick features with ageing time. As the ageing time increases, the features ASM and IDM exhibit an increasing logarithmic trend. In contrast, the features sum variance, entropy, sum entropy, and difference entropy show a decreasing logarithmic trend. Other features such as contrast and sum of square variance do not show a significant quantitative relationship between their values and the ageing time of the insulation paper.

As the ageing time increases, since the cellulose fibers of the insulating paper deteriorate in the ageing process, the cracks and holes in the fiber walls increase dramatically. This results in more uniform and homogeneous OCT images of the deteriorated paper samples with a concentrated transition between the pixel grayscale tones. ASM, also known as energy, is used to measure the uniformity in the pixel grayscale intensities in the image of texture. It is proportional to the global uniformity of grayscale tone transitions spread within an image. Therefore, an image having a uniform grayscale level distribution would result in a significant value of the ASM feature. From these observations, it is logical that the increasing logarithmic (upward) trends in ASM are due to the perceived texture becoming more granular with increased thermal deterioration. Similarly, the IDM shows an increasing logarithmic trend as a function of ageing

114
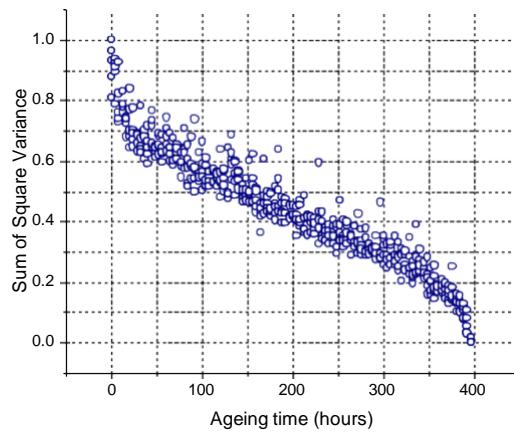
time, as shown in Figure 7.6 (d). IDM is used to measure the local homogeneity in an image. OCT images that contain concentrated regions of dark or bright pixels immediately neighboring each other will result in higher IDM. As the formation of cracks and holes increase in the fiber walls, the concentration of dark grayscale tones regions increases, and therefore the IDM also increases. This effect is apparent when comparing the brand-new paper and paper deteriorated for 396 hours, as shown in Figure 7.4. Unlike ASM and IDM, the entropy exhibited an increasing logarithmic trend as a function of increasing ageing time, as is evident in Figure 7.6 (h). Entropy measures the disorder in an image and is inversely related to IDM. The trend of the entropy implies that OCT images of the thermally aged Kraft paper have less concentrated details that yield a small entropy quantity. Moreover, the features, sum variance, sum entropy, and difference entropy, behave similar to entropy where all results show a good differentiability between the new Kraft paper and the deteriorated sample. Thus, in this work, the six features (ASM, IDM, sum variance, sum entropy, entropy, and difference entropy) that reflect the ageing condition of the insulating paper are selected as the characteristics to construct the age estimation model and features such as contrast don't reflect the actual ageing condition of the insulation paper . Further, some of the original image texture features can be used to implement the age estimation model. However, a regression model using a small number of the original image texture features would be less accurate than a model using all of the original image texture features, due to loss of information in the excluded features. Principal Component Analysis (PCA), a dimensionality reduction technique, incorporates almost all the information in all of the original image texture features by generating a smaller set of new features as linear combinations of all original features. Therefore, the usage of a small subset of the new PCA-generated features to build our regression model amounts to incorporating almost all the information in all of the original image texture features. The PCA is discussed in the next section.

(a)

(b)

(c)

(d)

(e)

(f)

116

(g)

(h)

(i)

(j)
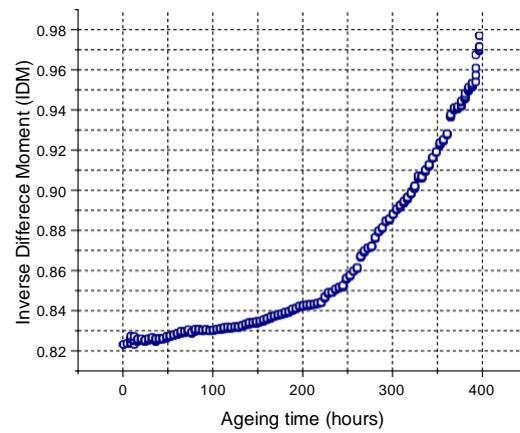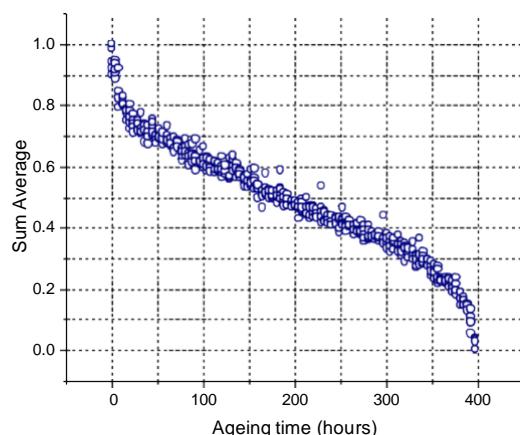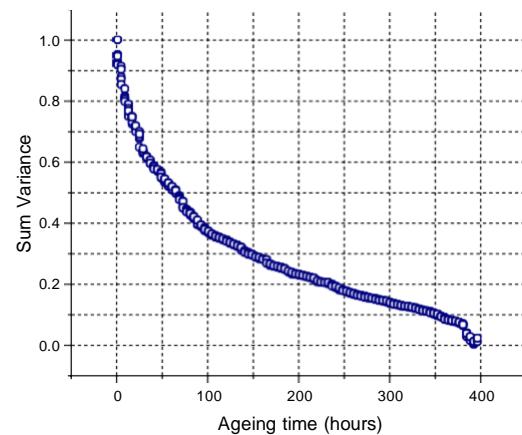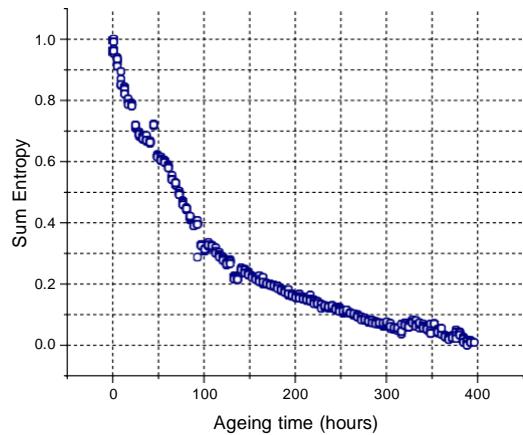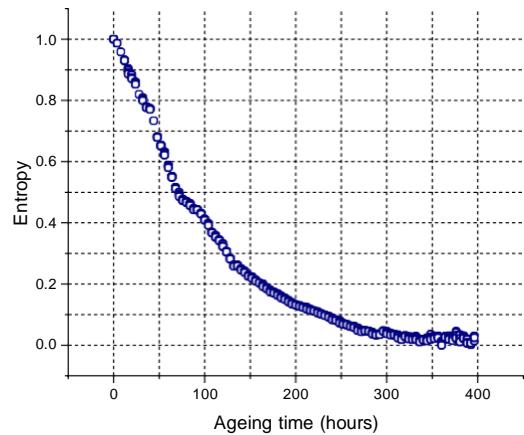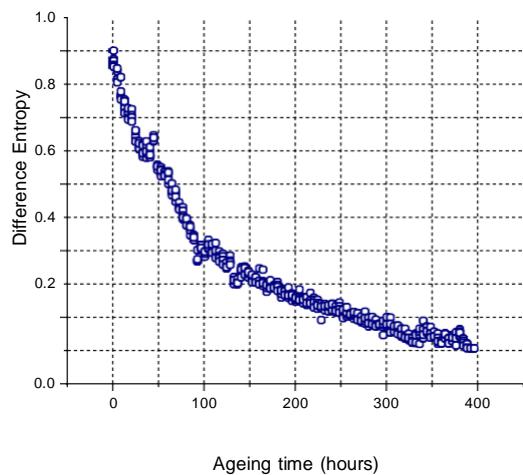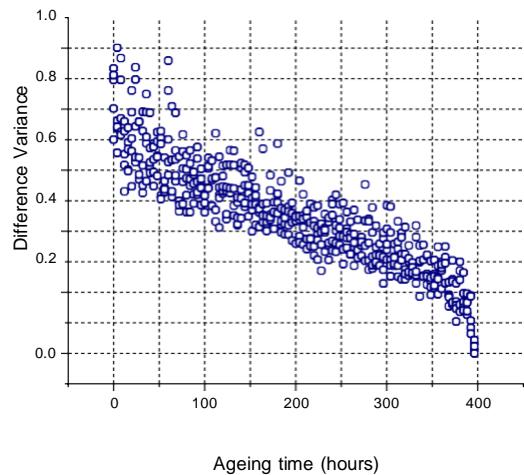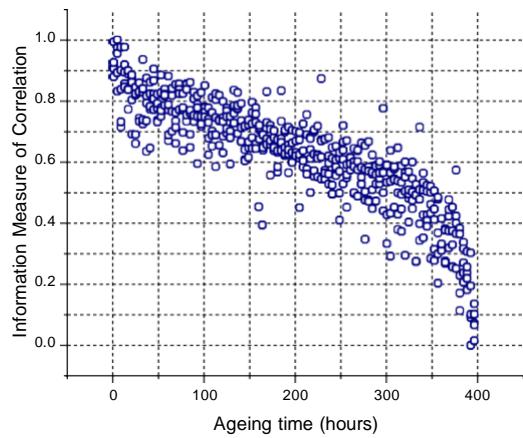
(k)

Figure 7.6. Relationship between Haralick texture features and ageing time (a) angular second moment, (b) contrast, (c) sum of square variance, (d) inverse difference moment, (e) sum average, (f) sum variance, (g) sum entropy, (h) entropy, (i) difference entropy, (j) difference variance, (k) information measure of correlation.

## 7.3  Texture Feature Reduction Using Principal Component Analysis

Following the Haralick feature extraction, one of the feature reduction techniques called principal component analysis (PCA) is applied to reduce the dimension of the feature matrix without loss of any important information. PCA is a statistical procedure and an unsupervised algorithm that orthogonally transforms data from a higher dimensional space into a new data set of a significantly lower dimension called principal components (PCs). The PCs are ranked in order of their explained variance and are uncorrelated with each other. The first principal component (PC1) explains the most variance that was present in the original components. PCA can be achieved via a series of steps. Let $Y = y_1, y_2, \dots, y_N$ be the original feature matrix, where $y_i$ represents the $i^{th}$ feature column vector and $N$ is the total number of samples. The PCA is performed by first estimating the covariance matrix C given by

$$\hat{C} = \frac{1}{N-1} \sum_{i=1}^{N} (y_i - \mu)(y_i - \mu)^T \tag{7.17}$$

where $\mu$ is the mean of $Y$. The final projection matrix can be obtained by computing the eigenvectors of the covariance matrix (V = eig{C}). In this work, we found out that the first component of the PCA retains about 98.2% of the total feature set information, so we used it to model the ageing time of transformer insulation. Figure 7.7 shows the logarithmic relationship between the first principal component (PC1) and the ageing time.
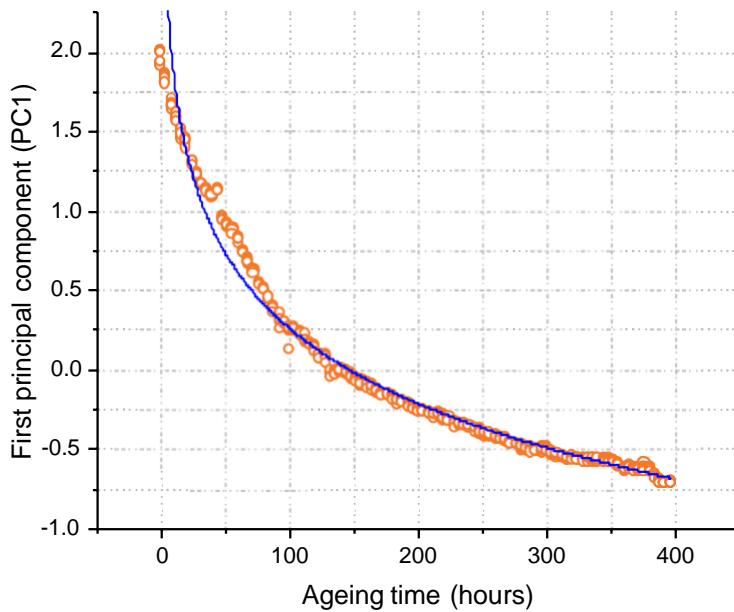
Figure 7.7. Relationship between the first principal component of the PCA and the ageing time

(in hours). Using a logarithmic function to fit these data, the age of Kraft paper can be readily calculated. The parameters of the model are obtained by solving a non-linear data fitting problem and is given by

$$PC1 = -1.568 \ln(\text{ageing time}) + 3.394. \tag{7.18}$$

The PC value of the insulating paper decreases as the ageing time increases. Note that in the early ageing stage, from zero to 150 hours, the PC value of the Kraft paper samples reduces dramatically with the ageing time, as shown in Figure 7.7. This corresponds to the breakdown of the long-chain cellulose molecules in the amorphous region of the Kraft paper, where the cellulose fibers are arranged disorderly and loosely. Therefore, in the early ageing stage, the amorphous region is easily damaged and leads to the rapid decline of the PC value. However, in the middle-later ageing stage, i.e., from 150 to 396 hours, the ageing rate of PC value is reducing.

119

Finally, we used the leave-one-out-cross-validation (LOOCV) to assess the estimation performance of our fitted model. LOOCV is a resampling procedure used to assess the accuracy of the model on limited data samples, where each sample is estimated within the complete data set of all other samples. Of our 500 training samples, 499 samples were used to obtain the regression model, and a test was carried out using the excluded sample. We repeated this procedure 500 times, and then we calculated the average error from these 500 models, where we achieved an average estimation error of 1.12%.

## 7.4   Chapter Summary

In this chapter, an experimental method for the generation of oil-impregnated insulation paper samples with different deterioration levels is described. The subsurface structural OCT images of the deteriorated insulation paper samples show clear textural changes due to thermal ageing. It is shown that the OCT image of the new cellulose Kraft paper has many texture variations that correspond to a network of fibers that are orderly arranged. As the paper becomes more thermally deteriorated, the OCT image of the Kraft paper becomes homogeneous in appearance. These correspond to the gaps and cracks created between the fibers as a consequence of thermal deterioration. A Min-Max normalization method was applied on each cross-sectional OCT image to obtain a better contrast and uniform distribution of intensities. After the normalization step, the pixel intensity values range from 0 to 255.

After image preprocessing, a machine learning algorithm called statistical texture analysis is applied to each OCT image to generate a spatial grayscale level dependence matrix (SGLDM), from which statistical texture features were calculated using Haralick equations. In this thesis, a total of 22 statistical texture features are computed from each insulation paper sample image. We demonstrated that twelve features (6 in each of vertical and horizontal directions) reflected the

ageing condition of the insulating paper and are selected as the characteristics to construct the age estimation model.

Following the Haralick feature extraction, one of the feature reduction techniques called principal component analysis (PCA) was also applied to the features to extract a new feature. We found out that the first principal component (PC1) of our PCA retains about 98.2% of the total feature set information, so we used it to model the ageing time of transformer insulation.

# Chapter 8

# Concluding Remarks

## 8.1   Conclusions

OCT is a novel non-invasive imaging modality based on interferometry used to acquire high-resolution 3-dimensional images of objects. These images provide information on the microstructures of the sample by looking at the amount of light backscattered by the different points in the sample. In addition to being used for capturing the cross-section views of samples, OCT can also be extended to extract spectroscopic information from a sample such as spatially localized absorption spectra without changing the system's hardware configurations. This is known as spectroscopy OCT where the complex refractive index of a sample can be obtained from the interferometric OCT signal using posterior signal processing. In a low absorption media, the real and imaginary components of the complex-valued refractive index refer to the scattering and

absorption profiles of the sample, respectively.

In this thesis, we implemented a quadrature swept-source OCT using a $3 \times 3$ fiber coupler to acquire the complex interferometric signal. We demonstrated that Fourier inversion on the full complex interferometric signal results in a complex conjugate resolved A-scans. We used Frame Theory to develop a generalized OCT image reconstruction method using redundant and non-uniformly spaced frequency domain samples that includes using non-redundant and uniformly spaced samples as special cases. We also corrected a critical theoretical error in the previously reported results related to OCT image reconstruction using the Nonuniform Discrete Fourier Transform (NDFT). Moreover, we described an efficient method to compute our corrected reconstruction transform, i.e., a *scaled* NDFT, using the Fast Fourier Transform (FFT). Further, Fourier inversion of the obtained SS-OCT interferogram typically produces a potentially overlapping conjugate mirror image, whose overlap could be avoided by restricting the object to have its strongest reflective surface at its own surface. However, this restriction may not be fulfilled when imaging a very thin object that is placed on a highly reflective surface or imaging an object containing a contrast agent with high reflectivity. We showed that oversampling of the SS-OCT signal in k-space would overcome such restriction on the object.

In this thesis, we also introduced a new concept of applying the compressed sensing technique to acquire a sample's spectroscopic properties. Further, we investigated the minimum number of measurements required for accurate recovery of the spectroscopy information by first computing the coherence value of the sensing matrix. A gradient-based method is proposed to reconstruct a multidimensional signal when an incomplete sampled measurement is collected in an arbitrary transformation domain to reduce the number of measurements. The method exploited the fact that many signals are known to have sparse gradients. The signal recovery would first recover these gradients individually and then reconstruct the original signal from the estimated gradients.

The main objective of this research was to develop a non-invasive optical technique to assess

the condition of power transformer cellulose insulating paper. In this thesis, a novel diagnostic OCT technique is used to acquire the subsurface structural image of the thermally deteriorated oil-impregnated Kraft paper. Machine learning techniques were applied to the OCT images to show that thermal deterioration of the insulation paper was detected by the statistical texture features extracted from the SGLDM. A total of 12 textural features results in good differentiability between the oil-impregnated paper samples with different levels of thermal degradation. We demonstrated that a logarithmic relationship exists between the texture features and the ageing time. The LOOCV was implemented to assess the estimation performance of our fitted model, where we achieved an estimation error of 1.12%. Our OCT-based method to estimate the ageing time of transformer insulation may be performed off-line during transformer maintenance outages while the oil is removed for inspection and potentially online using fiber optics and optical sensors.

## 8.2   Future Work

A long-term objective in this research is to develop an algorithm that uses both subsurface structural images and localized near-infrared absorption profiles obtained by spectroscopic optical coherence tomography, to estimate the remaining lifetime of high voltage transformer insulation paper. When light is incident on a material, the light can cause stretching or vibrations of molecular bonds. If the wavelength of the light source is varied over a range, a spectral plot of the light absorption as a function of wavelength can be generated. These spectra can be used to identify the chemical composition of materials as the spectra correspond to specific molecular bond vibrations. Spectral changes in transformer cellulose insulation due to thermal ageing has been demonstrated in [135, 136]. Deterioration is observed through a combination of changes in resonant peaks ('bond vibrations') related to stretches and bends to cellulose C-H, C-C, C-O, and O-H bonds. However, the existing bulk spectroscopy techniques typically result in only spatially averaged infrared absorption values of samples. Therefore, obtaining both subsurface structural images and spatially

localized near-infrared (NIR) (1300nm) absorption profiles of transformer paper would offer considerably more information about the samples than obtained from current optical methods. This extra information should allow a more accurate estimation of the remaining operational age.

Another possible area of future work is to incorporate a fiber-based spectroscopic OCT that would allow almost instantaneous in-field estimation during transformer maintenance outages. Further, in future work, the statistical texture analysis may be computed in parallel using a Graphics Processing Unit (GPU) module as the computation of textural features for large-size images is computationally expensive. Also, instead of performing a data-fitting problem, a supervised machine learning method, e.g., K nearest neighbor, can be applied to the SGLDM values to estimate the remaining operational lifetime of the insulation paper.

# References

[1]   D. Feng, Z. Wang, and P. Jarman, "Modeling thermal life expectancy of the UK transmission power transformers," in *2012 IEEE International Conference on High Voltage Engineering and Application*, Sep 2012.

[2]   D. Feng, Life expectancy investigation of transmission power transformers. The University of Manchester, Faculty of Electrical Engineering and Physical Sciences, 2013.

[3]   "IEEE guide for loading mineral-oil-immersed transformers and step-voltage regulators," *IEEE Std C57.91-2011 (Revision of IEEE Std C57.91-1995)*, pp. 1–123, 2012.

[4]   Nathan Jacob, "texture Analysis of Microscopy Images from Power Transformer Cellulose Insulation for Aging Condition Assessment", PhD thesis, University of Manitoba, Winnipeg, 2017.

[5]   S. Chakravorti, D. Dey, and B. Chatterjee, *Recent Trends in the Condition Monitoring of Transformers*. London: Springer, 2013.

[6]   *Ageing of cellulose in mineral-oil insulated transformers*, Cigre Bulletin TB 323, Task Force D1.01.10, 2007.

[7]   Susilo, Suwarno, U. Khayam, M. Tsuchie, M. Thein, M. Hikita, and T. Saito, "Study on dissolved gas due to thermally degraded insulating paper in transformer oil," *Procedia Technology*, vol. 11, pp. 257 – 262, 2013.

[8]   J. Jalbert, M. C. Lessard, and M. Ryadi, "Cellulose chemical markers in transformer oil insulation part 1: Temperature correction factors," *IEEE Transactions on Dielectrics and Electrical Insulation*, vol. 20, no. 6, pp. 2287–2291, December 2013.

[9]   P. M. Mitchinson, P. L. Lewin, B. D. Strawbridge, and P. Jarman, "Tracking and surface discharge at the oil and pressboard interface," *IEEE Electrical Insulation Mag-azine*, vol. 26, no. 2, pp. 35–41, mar 2010.

[10]  "IEEE guide for the interpretation of gases generated in mineral oil-immersed trans-formers," *IEEE Std C57.104-2019 (Revision of IEEE Std C57.104-2008)*, pp. 1–98, 2019.

[11]  L. Ruijin, T. Chao, Y. Lijun, and C. Huanchao, "Thermal aging studies on cellulose insulation paper of power transformer using afm," *8th International Conference on Properties and applications of Dielectric Materials*, pp. 722–725, June 2006.

[12] A. Emsley, M. Ali, X. Xiao, and R. Heywood, "Degradation of cellulosic insulation in power transformers. part 4: Effects of ageing on the tensile strength of paper," *IEE Proceedings - Science, Measurement and Technology*, vol. 147, no. 6, pp. 285–290, Nov 2000.

[13] L. Lundgaard, W. Hansen, D. Linhjell, and T. Painter, "Ageing of oil-impregnated paper in power transformers," *IEEE Transactions on Power Delivery*, vol. 19, no. 1, pp. 230–239, Jan 2004.

[14] W. T. Shugg, *Handbook of Electrical and Electronic Insulating Materials*. London: Van Nostrand Reinshold, 1986.

[15] "High-voltage test techniques. partial discharge measurements."

[16] *High Voltage Engineering Fundamentals*. Elsevier, 2000.

[17] V. Sokolov, Z. Berler, and V. Rashkes, "Effective methods of assessment of insulation system conditions in power transformers: a view based on practical experience," in *Proceedings: Electrical Insulation Conference and Electrical Manufacturing and Coil Winding Conference (Cat. No.99CH37035)*. IEEE.

[18] I. Hohlein and A. Kachler, "Ageing of cellulose at transformer service temperatures. Part 2. influence of moisture and temperature on degree of polymerization and formation of furanic compounds in free-breathing systems," *IEEE Electrical Insulation Magazine*, vol. 21, no. 5, pp. 20–24, Sep 2005.

[19] A. Abu-Siada, S. P. Lai, and S. M. Islam, "A novel fuzzy-logic approach for furan estimation in transformer oil," *IEEE Transactions on Power Delivery*, vol. 27, no. 2, pp. 469–474, apr 2012.

[20] Y. Lin, C. Wei, F. Tao, and J. Li, "Ageing assessment of oil-paper insulation of power equipment with furfural analysis based on furfural generation and partitioning," *IEEE Transactions on Power Delivery*, vol. 34, no. 4, pp. 1626–1633, aug 2019.

[21] M. Pradhan and T. Ramu, "On the estimation of elapsed life of oil-immersed power transformers," *IEEE Transactions on Power Delivery*, vol. 20, no. 3, pp. 1962–1969, July 2005.

[22] O. E. Gouda and A. Z. E. Dein, "Prediction of aged transformer oil and paper insulation," *Electric Power Components and Systems*, vol. 47, no. 4-5, pp. 406–419, mar 2019.

[23] A. Emsley, R. Heywood, X. Xiao, and M. Ali, "Degradation of cellulosic insulation in power transformers. part 2: Formation of furan products in insulating oil," *IEE Proceedings - Science, Measurement and Technology*, vol. 147, no. 3, pp. 110–114, May

2000.

[24] S. Li, H. Ma, T. K. Saha, Y. Yang, and G. Wu, "On particle filtering for power transformer remaining useful life estimation," *IEEE Transactions on Power Delivery*, vol. 33, no. 6, pp. 2643–2653, dec 2018.

[25] D. Zhou, Z. Wang, and C. Li, "Data requisites for transformer statistical lifetime modelling-part ii: Combination of random and ageing-related failures," *IEEE Transactions on Power Delivery*, vol. 28, no. 3, pp. 1750–1757, july 2013.

[26] S. M. Agah and H. A. Abyaneh, "Distribution transformer loss-of-life reduction by increasing penetration of distributed generation," *IEEE Transactions on Power Delivery*, vol. 26, no. 2, pp. 1128–1136, apr 2011.

[27] S. M. Agah and H. A. Abyaneh, "Effect of modeling non-normality and stochastic dependence of variables on distribution transformer loss of life inference," *IEEE Transactions on Power Delivery*,vol. 27, no. 4, pp. 1700–1709, oct 2012.

[28] *Standard Test method for measurement of average viscometric degree of polymerization of newand aged electrical papers and boards*, ASTM D4243-99, 2009.

[29] *Measurement of the average viscometric degree of polymerization of new and aged cellulosic electrically insulating materials*, IEC 60450, 2004.

[30] N. D. Jacob, S. Sherif, D. R. Oliver, and B. Kordi, "Correlation of microscopic textural features and degree of polymerization for thermally deteriorated cellulose insulation," in *2016 IEEE Electrical Insulation Conference (EIC)*. IEEE, Jun 2016.

[31] N. D. Jacob, H. Hassanzadeh, D. R. Oliver, S. S. Sherif, and B. Kordi, "Classification of degradation in oil-impregnated cellulose insulation using texture analysis of optical microscopy images," *Electric Power Systems Research*, vol. 133, pp. 104–112, Apr 2016.

[32] N. D. Jacob, S. S. Sherif, and B. Kordi, "Quantification of changes in surface texture of thermally-aged kraft paper using orthogonal wavelets," in *2017 IEEE Electrical Power and Energy Conference (EPEC)*. IEEE, Oct 2017.

[33] N. D. Jacob, D. R. Oliver, S. S. Sherif, and B. Kordi, "Statistical texture analysis of morphological changes in pressboard insulation due to thermal ageing and partial discharges," in *2015 IEEE Electrical Insulation Conference (EIC)*. IEEE, Aug 2015.

[34] J. Borch, M. B. Lyne, R. E. Mark, and C. Habeger, Eds., *Handbook of Physical Testing of Paper*. CRC Press, Sep 2001.

[35] P. Verma, M. Roy, A. Verma, and V. Bhanot, "Assessment of degradation of transformer insulation paper by SEM and x-RD techniques," in *Proceedings of the 2004*

*IEEE International Conference on Solid Dielectrics, ICSD 2004.* IEEE, 2004.

[36]  P. Verma, D. Chauhan, and P. Singh, "Effects on tensile strength of transformer insu- lation paper under accelerated thermal and electrical stress," in *2007 Annual Report - Conference on Electrical Insulation and Dielectric Phenomena.* IEEE, 2007.

[37]  R. J. Liao, C. Tang, L. jun Yang, and S. Grzybowski, "Thermal ageing micro-scale anal- ysis of power transformer pressboard," *IEEE Transactions on Dielectrics and Electrical Insulation*, vol. 15, no. 5, pp. 1281–1287, Oct 2008.

[38]  G. Piantanida, M. Bicchieri, and C. Coluzza, "Atomic force microscopy characteriza- tion of the ageing of pure cellulose paper," *Polymer*, vol. 46, no. 26, pp. 12 313–12 321, dec 2005.

[39]  P. Baird, H. Herman, and G. Stevens, "On-site analysis of transformer paper insula- tion using portable spectroscopy for chemometric prediction of aged condition," *IEEE Transactions on Dielectrics and Electrical Insulation*, vol. 15, no. 4, pp. 1089–1099, aug 2008.

[40]  S.-H. Kim, E. Cherney, R. Hackam, and K. Rutherford, "Chemical changes at the surface of RTV silicone rubber coatings on insulators during dry-band arcing," *IEEE Transactions on Dielectrics and Electrical Insulation*, vol. 1, no. 1, pp. 106–123, 1994.

[41]  D. P. Popescu, L.-P. Choo-Smith, C. Flueraru, Y. Mao, S. Chang, J. Disano, S. Sherif, and M. G. Sowa, "Optical coherence tomography: fundamental principles, instru- mental designs and biomedical applications," *Biophysical Reviews*, vol. 3, no. 3, pp. 155–169, aug 2011.

[42]  R. Leitgeb, C. Hitzenberger, and A. Fercher, "Performance of fourier domain vs time domain optical coherence tomography," *Optics Express*, vol. 11, no. 8, p. 889, apr 2003.

[43]  S. R. Chinn, E. A. Swanson, and J. G. Fujimoto, "Optical coherence tomography using a frequency-tunable optical source," *Optics Letters*, vol. 22, no. 5, p. 340, mar 1997.

[44]  J. G. Fujimoto, "Optical coherence tomography for ultrahigh resolution in vivo imag- ing," *Nature Biotechnology*, vol. 21, no. 11, pp. 1361–1367, oct 2003.

[45]  J. Fujimoto, "Optical coherence tomography:  technology and applications," in *IEEE/LEOS International Conference on Optical MEMs*.

[46]  M. Wojtkowski, "High-speed optical coherence tomography: basics and applications," *Applied Optics*, vol. 49, no. 16, p. D30, mar 2010.

[47]  E. Scalco and G. Rizzo, "SP-0568: Texture analysis of medical images in radiotherapy," *Radiotherapy and Oncology*, vol. 119, pp. S273–S274, Apr 2016.

[48]  M. H. Bharati, J. Liu, and J. F. MacGregor, "Image texture analysis: methods and

comparisons," *Chemometrics and Intelligent Laboratory Systems*, vol. 72, no. 1, pp. 57–71, June 2004.

[49] A. Dixit and N. P. Hegde, "Image texture analysis - survey," in *2013 Third International Conference on Advanced Computing and Communication Technologies (ACCT)*. IEEE, April 2013.

[50] *Feature Extraction & Image Processing for Computer Vision*. Elsevier, 2012.

[51] S. Arivazhagan, T. G. S. Kumar, and L. Ganesan, "Texture Classification Using Curvelet Transform," *International Journal of Wavelets, Multiresolution and Information Processing*, vol. 05, no. 03, pp. 451–464, may 2007.

[52] M. Idrissa and M. Acheroy, "Texture classification using gabor filters," *Pattern Recognition Letters*, vol. 23, no. 9, pp. 1095–1102, Jul 2002.

[53] M. V. Sarunic, M. A. Choma, C. Yang, and J. A. Izatt, "Instantaneous complex conjugate resolved spectral domain and swept-source OCT using 3x3 fiber couplers," *Optics Express*, vol. 13, no. 3, p. 957, 2005.

[54] J. Zhang, W. Jung, J. S. Nelson, and Z. Chen, "Full range polarization-sensitive fourier domain optical coherence tomography," *Optics Express*, vol. 12, no. 24, p. 6033, 2004.

[55] S. H. Yun, G. J. Tearney, J. F. de Boer, and B. E. Bouma, "Removing the depth-degeneracy in optical frequency domain imaging with frequency shifting," *Optics Express*, vol. 12, no. 20, p. 4822, 2004.

[56] B. J. Vakoc, S. H. Yun, G. J. Tearney, and B. E. Bouma, "Elimination of depth degeneracy in optical frequency-domain imaging through polarization-based optical demodulation," *Optics Letters*, vol. 31, no. 3, p. 362, 2006.

[57] M. V. Sarunic, B. E. Applegate, and J. A. Izatt, "Real-time quadrature projection complex conjugate resolved fourier domain optical coherence tomography," *Optics Letters*, vol. 31, no. 16, p. 2426, Jul 2006.

[58] Y. Mao, S. Sherif, C. Flueraru, and S. Chang, "3×3 mach-zehnder interferometer with unbalanced differential detection for full-range swept-source optical coherence tomography," *Applied Optics*, vol. 47, no. 12, p. 2004, apr 2008.

[59] M. Born and E. Wolf, *Principles of Optics*. Cambridge University Press, dec 2019.

[60] E. Wolf, "Three-dimensional structure determination of semi-transparent objects from holographic data," *Optics Communications*, vol. 1, no. 4, pp. 153–156, sep 1969.

[61] A. Fercher, C. Hitzenberger, G. Kamp, and S. El-Zaiat, "Measurement of intraocular distances by backscattering spectral interferometry," *Optics Communications*, vol. 117, no. 1-2, pp. 43–48, may 1995.

[62] B. Golubovic, B. E. Bouma, G. J. Tearney, and J. G. Fujimoto, "Optical frequency-

domain reflectometry using rapid wavelength tuning of a Cr4+:forsterite laser," *Optics Letters*, vol. 22, no. 22, p. 1704, nov 1997.

[63]  S. S. Sherif, C. Flueraru, Y. Mao, and S. Chang, "Swept source optical coherence tomography with nonuniform frequency domain sampling," in *Biomedical Optics*. OSA, 2008.

[64]  *A Wavelet Tour of Signal Processing*.  Elsevier, 1999.

[65]  B. Cense, N. A. Nassif, T. C. Chen, M. C. Pierce, S.-H. Yun, B. H. Park, B. E. Bouma, G. J. Tearney, and J. F. de Boer, "Ultrahigh-resolution high-speed retinal imaging using spectral-domain optical coherence tomography," *Optics Express*, vol. 12, no. 11, p. 2435, may 2004.

[66]  S. Vergnole, D. Lévesque, and G. Lamouche, "Experimental validation of an optimized signal processing method to handle non-linearity in swept-source optical coherence tomography," *Optics Express*, vol. 18, no. 10, p. 10446, may 2010. [Online]. Available: https://doi.org/10.1364%2Foe.18.010446

[67]  S. H. Yun, G. J. Tearney, J. F. de Boer, and B. E. Bouma, "Motion artifacts in optical coherence tomography with frequency-domain ranging," *Optics  Express*, vol. 12, no. 13, p. 2977, 2004.

[68]  R. Huber, M. Wojtkowski, K. Taira, J. G. Fujimoto, and K. Hsu, "Amplified, frequency swept lasers for frequency domain reflectometry and OCT imaging: design and scaling principles," *Optics Express*, vol. 13, no. 9, p. 3513, 2005.

[69]  E. Azimi,  B. Liu,  and M. E. Brezinski,  "Real-time and high-performance calibration method for high-speed swept-source optical coherence tomography," *Journal of Biomedical Optics*, vol. 15, no. 1, p. 016005, 2010.

[70]  C. Chong, A. Morosawa, and T. Sakai, "High speed wavelength-swept laser source with simple configuration for optical coherence tomography," in Optical Coherence Tomography and Coherence Techniques III. OSA, 2007.

[71]  T. Wu, Z. Ding, L. Wang, and M. Chen, "Spectral phase-based k-domain interpolation for uniform sampling in swept-source optical coherence tomography," *Optics Express*, vol. 19, no. 19, p. 18430, sep 2011.

[72]  S. H. Yun, G. J. Tearney, J. F. de Boer, and B. E. Bouma, "Removing the depth-degeneracy in optical frequency domain imaging with frequency shifting," *Optics Express*, vol. 12, no. 20, p. 4822, 2004.

[73]  Sina Farsiu, Stephanie J. Chiu, Rachelle V. O'Connell, Francisco A. Folgar, Eric Yuan, Joseph A. Izatt, Cynthia A. Toth,"Quantitative Classification of Eyes with and without Intermediate Age-related Macular Degeneration Using Optical Coherence Tomography Ophthalmology",Volume 121, Issue 1,2014.

[74]  I. Grulkowski, J. J. Liu, B. Potsaid, V. Jayaraman, C. D. Lu, J. Jiang, A. E. Cable,

J. S. Duker, and J. G. Fujimoto, "Retinal, anterior segment and full eye imaging using ultrahigh speed swept source OCT with vertical-cavity surface emitting lasers," *Biomedical Optics Express*, vol. 3, no. 11, p. 2733, oct 2012.

[75] Y. Jia and R. K. Wang, "Label-free in vivo optical imaging of functional microcirculations within meninges and cortex in mice," *Journal of Neuroscience Methods*, vol. 194, no. 1, pp. 108–115, dec 2010

[76] J. Xu, W. Wei, S. Song, X. Qi, and R. K. Wang, "Scalable wide-field optical coherence tomography-based angiography for in vivo imaging applications," *Biomedical Optics Express*, vol. 7, no. 5, p. 1905, apr 2016.

[77] U. Morgner, W. Drexler, X. Li, F. Kartner, C. Pitris, S. Boppart, E. Ippen, and J. Fujimoto, "Spectroscopic optical coherence tomography," in *Technical Digest. Summaries of Papers Presented at the Quantum Electronics and Laser Science Conference*. Opt. Soc. America.

[78] R. Leitgeb, M. Wojtkowski, A. Kowalczyk, C. K. Hitzenberger, M. Sticker, and A. F. Fercher, "Spectral measurement of absorption by spectroscopic frequency-domain optical coherence tomography," *Optics Letters*, vol. 25, no. 11, p. 820, jun 2000.

[79] D. J. Faber, E. G. Mik, M. C. G. Aalders, and T. G. van Leeuwen, "Light absorption of (oxy-)hemoglobin assessed by spectroscopic optical coherence tomography," *Optics Letters*, vol. 28, no. 16, p. 1436, aug 2003.

[80] S. A. Boppart, S. A. Boppart, M. E. Brezinski, C. Pitris, C. Pitris, and J. G. Fujimoto, "Optical coherence tomography for neurosurgical imaging of human intracortical melanoma," *Neurosurgery*, vol. 43, no. 4, pp. 834–841, oct 1998.

[81] Z. Yaqoob, E. McDowell, J. Wu, X. Heng, J. Fingler, and C. Yang, "Molecular contrast optical coherence tomography: a pump-probe scheme using indocyanine green as a contrast agent," *Journal of Biomedical Optics*, vol. 11, no. 5, p. 054017, 2006.

[82] K. D. Rao, M. A. Choma, S. Yazdanfar, A. M. Rollins, and J. A. Izatt, "Molecular contrast in optical coherence tomography by use of a pump–probe technique," *Optics Letters*, vol. 28, no. 5, p. 340, mar 2003.

[83] C. Yang, M. Choma, J. Simon, and J. A. Izatt, "Spectral triangulation molecular contrast OCT with indocyanine green as the contrast agent," in *Biomedical Topical Meeting*. OSA, 2004.

[84] C. Xu, J. Ye, D. L. Marks, and S. A. Boppart, "Near-infrared dyes as contrast-enhancing agents for spectroscopic optical coherence tomography," *Optics Letters*, vol. 29, no. 14, p. 1647, jul 2004.

[85] R. N. Graf and A. Wax, "Nuclear morphology measurements using fourier domain low coherence interferometry," *Optics Express*, vol. 13, no. 12, p. 4693, 2005.

[86] D. C. Adler, T. H. Ko, P. R. Herz, and J. G. Fujimoto, "Optical coherence tomography

contrast enhancement using spectroscopic analysis with spectral autocorrelation," *Optics Express*, vol. 12, no. 22, p. 5487, 2004.

[87] T. S. Kim, S.-J. Jang, N. Oh, Y. Kim, T. Park, J. Park, and W.-Y. Oh, "Dual- wavelength band spectroscopic optical frequency domain imaging using plasmon- resonant scattering in metallic nanoparticles," *Optics Letters*, vol. 39, no. 10, p. 3082, May 2014.

[88] L. Yu, J. Kang, C. Jinata, X. Wang, X. Wei, K. T. Chan, N. P. Lee, and K. K. Y. Wong, "Tri-band spectroscopic optical coherence tomography based on optical parametric amplification for lipid and vessel visualization," *Journal of Biomedical Optics*, vol. 20, no. 12, p. 126006, dec 2015.

[89] C. Xu, D. L. Marks, M. N. Do, and S. A. Boppart, "Separation of absorption and scattering profiles in spectroscopic optical coherence tomography using a least-squares algorithm," *Optics Express*, vol. 12, no. 20, p. 4790, 2004.

[90] C. Xu and S. A. Boppart, "Comparative performance analysis of time-frequency distributions for spectroscopic optical coherence tomography," in *Biomedical Topical Meeting*. OSA, 2004.

[91] J. Yi, J. Gong, and X. Li, "Analyzing absorption and scattering spectra of micro-scale structures with spectroscopic optical coherence tomography," *Optics Express*, vol. 17, no. 15, p. 13157, jul 2009.

[92] D. J. Faber, E. G. Mik, M. C. Aalders, and T. G. van Leeuwen, "Toward assessment of blood oxygen saturation by spectroscopic optical coherence tomography," *Optics Letters*, vol. 30, no. 9, p. 1015, May 2005.

[93] F. Robles, R. N. Graf, and A. Wax, "Dual window method for processing spectroscopic optical coherence tomography signals with simultaneously high spectral and temporal resolution," *Optics Express*, vol. 17, no. 8, p. 6799, apr 2009.

[94] V. Jaedicke, S. Agcaer, F. E. Robles, M. Steinert, D. Jones, S. Goebel, N. C. Gerhardt, H. Welp, and M. R. Hofmann, "Comparison of different metrics for analysis and visualization in spectroscopic optical coherence tomography," *Biomedical Optics Express*, vol. 4, no. 12, p. 2945, nov 2013.

[95] J.-L. Starck, F. Murtagh, and J. Fadili, *Sparse Image and Signal Processing*. Cambridge University Press, 2009.

[96] Y. C. Eldar and G. Kutyniok, Eds., *Compressed Sensing*. Cambridge University Press, 2009.

[97] D. L. Donoho and I. M. Johnstone, "Ideal denoising in an orthonormal basis chosen from a library of bases," 1994.

[98] D. L. Donoho and M. Elad, "Optimally sparse representation in general (nonorthogo-

nal) dictionaries via 1 minimization," *Proceedings of the National Academy of Sciences*, vol. 100, no. 5, pp. 2197–2202, feb 2003.

[99] S. Boyd and L. Vandenberghe, *Convex Optimization*. Cambridge University Press, mar 2004.

[100] S. Mallat and Z. Zhang, "Matching pursuits with time-frequency dictionaries," *IEEE Transactions on Signal Processing*, vol. 41, no. 12, pp. 3397–3415, 1993.

[101] S. Mallat, *A Wavelet Tour of Signal Processing*. Elsevier, 2009.

[102] E. Elhamifar and R. Vidal, "Robust classification using structured sparse representation," in *CVPR 2011*. IEEE, june 2011.

[103] M. Elad and M. Aharon, "Image denoising via sparse and redundant representations over learned dictionaries," *IEEE Transactions on Image Processing*, vol. 15, no. 12, pp. 3736–3745, dec 2006.

[104] J. Yang, J. Wright, T. S. Huang, and Y. Ma, "Image super-resolution via sparse representation," *IEEE Transactions on Image Processing*, vol. 19, no. 11, pp. 2861–2873, 2010.

[105] M. F. Duarte and R. G. Baraniuk, "Kronecker product matrices for compressive sensing," in *2010 IEEE International Conference on Acoustics, Speech and Signal Processing*. IEEE, 2010.

[106] J. Bioucas-Dias and M. Figueiredo, "A new TwIST: Two-step iterative shrinkage/thresholding algorithms for image restoration," *IEEE Transactions on Image Processing*, vol. 16, no. 12, pp. 2992–3004, dec 2007.

[107] S. Ma, W. Yin, Y. Zhang, and A. Chakraborty, "An efficient algorithm for compressed MR imaging using total variation and wavelets," in *2008 IEEE Conference on Computer Vision and Pattern Recognition*. IEEE, jun 2008.

[108] J. Yang, Y. Zhang, and W. Yin, "A fast alternating direction method for TVL1-l2 signal reconstruction from partial fourier data," *IEEE Journal of Selected Topics in Signal Processing*, vol. 4, no. 2, pp. 288–297, apr 2010.

[109] S. Becker, J. Bobin, and E. J. Candès, "NESTA: A fast and accurate first-order method for sparse recovery," *SIAM Journal on Imaging Sciences*, vol. 4, no. 1, pp. 1–39, jan 2011.

[110] L. I. Rudin, S. Osher, and E. Fatemi, "Nonlinear total variation based noise removal algorithms," *Physica D: Nonlinear Phenomena*, vol. 60, no. 1-4, pp. 259–268, nov 1992.

[111] E. Y. Sidky and X. Pan, "Image reconstruction in circular cone-beam computed tomography by constrained, total-variation minimization," *Physics in Medicine and Biology*,

vol. 53, no. 17, pp. 4777–4807, aug 2008.

[112] E. Candes, J. Romberg, and T. Tao, "Robust uncertainty principles: exact signal reconstruction from highly incomplete frequency information," *IEEE Transactions on Information Theory*, vol. 52, no. 2, pp. 489–509, feb 2006.

[113] S. Chretien, P. Harris, and R. Tawil, "Total variation minimization for compressed sensing with "smoothly" varying covariates," in *2016 IEEE Intl Conference on Computational Science and Engineering (CSE) and IEEE Intl Conference on Embedded and Ubiquitous Computing (EUC) and 15th Intl Symposium on Distributed Computing and Applications for Business Engineering (DCABES)*. IEEE, aug 2016.

[114] F. Krahmer, C. Kruschel, and M. Sandbichler, "Total variation minimization in compressed sensing," in *Compressed Sensing and its Applications*. Springer International Publishing, 2017, pp. 333–358.

[115] C. Poon, "On the role of total variation in compressed sensing," *SIAM Journal on Imaging Sciences*, vol. 8, no. 1, pp. 682–720, jan 2015.

[116] V. M. Patel, R. Maleh, A. C. Gilbert, and R. Chellappa, "Gradient-based image recovery methods from incomplete fourier measurements," *IEEE Transactions on Image Processing*, vol. 21, no. 1, pp. 94–105, jan 2012.

[117] R. Maleh, A. C. Gilbert, and M. J. Strauss, "Sparse gradient image reconstruction done faster," in *2007 IEEE International Conference on Image Processing*. IEEE, 2007.

[118] M. Lustig, D. Donoho, and J. M. Pauly, "Sparse MRI: The application of compressed sensing for rapid MR imaging," *Magnetic Resonance in Medicine*, vol. 58, no. 6, pp. 1182–1195, 2007.

[119] Y. Wang, J. Yang, W. Yin, and Y. Zhang, "A new alternating minimization algorithm for total variation image reconstruction," *SIAM Journal on Imaging Sciences*, vol. 1, no. 3, pp. 248–272, jan 2008.

[120] V. M. Patel, G. R. Easley, R. Chellappa, and D. M. Healy, "Enhancing sparsity using gradients for compressive sensing," in *2009 16th IEEE International Conference on Image Processing (ICIP)*. IEEE, nov 2009.

[121] Y. Rivenson and A. Stern, "Compressed imaging with a separable sensing operator," *IEEE Signal Processing Letters*, vol. 16, no. 6, pp. 449–452, june 2009.

[122] T. G. Kolda and B. W. Bader, "Tensor decompositions and applications," *SIAM Review*, vol. 51, no. 3, pp. 455–500, aug 2009.

[123] S. Hawe, M. Seibert, and M. Kleinsteuber, "Separable dictionary learning," in *2013 IEEE Conference on Computer Vision and Pattern Recognition*. IEEE, june 2013.

[124] A. Agrawal, R. Raskar, and R. Chellappa, "What is the range of surface reconstructions from

a gradient field?" in *Computer Vision – ECCV 2006*. Springer Berlin Heidelberg,2006, pp. 578–591.

[125] T. Simchony, R. Chellappa, and M. Shao, "Direct analytical methods for solving poisson equations in computer vision problems," *IEEE Transactions on Pattern Analysis and Machine Intelligence*, vol. 12, no. 5, pp. 435–446, may 1990.

[126] Z. Chen and L. Lu, "A gradient based iterative solutions for sylvester tensor equations," *Mathematical Problems in Engineering*, vol. 2013, pp. 1–7, 2013.

[127] J. Ding, "Data filtering based recursive and iterative least squares algorithms for parameter estimation of multi-input output systems," *Algorithms*, vol. 9, no. 3, p. 49, july 2016.

[128] T. G. Kolda, "Multilinear operators for higher-order decompositions." Tech. Rep., apr 2006.

[129] P. J. LaMontagne et al., "OASIS-3: LONGITUDINAL NEUROIMAGING, CLINICAL, AND COGNITIVE DATASET FOR NORMAL AGING AND ALZHEIMER'S DISEASE," Alzheimer's Dement., vol. 14, no. 7S_Part_2, pp. P138–P138, Jul. 2018, doi: 10.1016/j.jalz.2018.06.2231.

[130] J. D. Singh, Y. R. Sood, and P. Verma, "Review of different prorated models which detects the effect of accelerated stresses on power transformer insulation," *International Journal of Computer and Electrical Engineering*, pp. 569–574, 2010.

[131] E. L. Morrison, "Evaluation of the thermal stability of electrical insulating paper," in *1967 Seventh Electrical Insulation Conference*. IEEE, Oct 1967.

[132] P. Sun, W. Sima, M. Yang, and J. Wu, "Influence of thermal ageing on the breakdown characteristics of transformer oil impregnated paper," *IEEE Transactions on Dielectrics and Electrical Insulation*, vol. 23, no. 6, pp. 3373–3381, Dec 2016.

[133] R. C. Gonzalez, R. E. Woods, and B. R. Masters, "Digital image processing, third edition," *Journal of Biomedical Optics*, vol. 14, no. 2, p. 029901, 2009.

[134] R. M. Haralick, K. Shanmugam, and I. Dinstein, "Textural features for image classification," *IEEE Transactions on Systems, Man, and Cybernetics*, vol. SMC-3, no. 6, pp. 610–621, Nov 1973.

[135] M. Shenton, "The use of spectroscopy with chemometrics to assess the condition and predict the lifetime of paper and oil used as transformer insulation," in *Eighth International Conference on Dielectric Materials, Measurements and Applications*. IEE, 2000.

[136] E. O. dos Santos, A. M. S. Silva, W. D. Fragoso, C. Pasquini, and M. F. Pimentel, "Corrigendum to "determination of degree of polymerization of insulating paper using near infrared spectroscopy and multivariate calibration" *Vibrational Spectroscopy*, vol. 54, no. 1, p. 81, sep 2010.